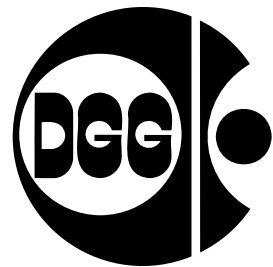
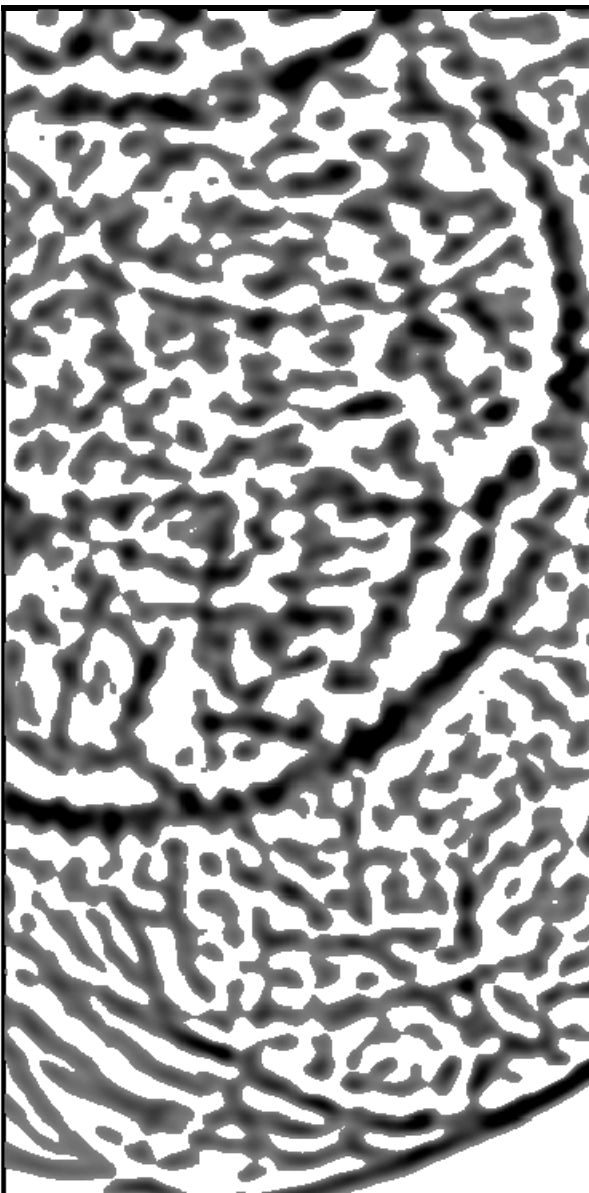


Deutsche Geophysikalische Gesellschaft e.V.



Noise and Diffuse Wavefields

**- Extended Abstracts of
the Neustadt Workshop -**

**Neustadt an der
Weinstraße, Germany,
5 - 8 July 2009**

**Sonderband II/2009
ISSN 0947-1944**

ISBN 978-3-00-027952-2

MITTEILUNGEN

Herausgeber:
Christoph Sens-Schönfelder, Joachim Ritter,
Ulrich Wegler, Christian Große
Im Auftrag der
Deutschen Geophysikalischen Gesellschaft e.V.

IMPRESSUM

Herausgeber im Auftrag der Deutschen Geophysikalischen Gesellschaft:

Dr. Christoph Sens-Schönenfelder
Universität Leipzig
Faculty of Physics and Earth Science
Department of Geophysics and Geology
Talstraße 35
04103 Leipzig
Germany
phone: +49 - (0)341 - 9732816
fax: +49 - (0)341 - 9732809
email: sens-schoenfelder@uni-leipzig.de

PD Dr. Joachim Ritter
Geophysical Institute
Universität Karlsruhe (TH)
Hertzstr. 16
76187 Karlsruhe
Germany
phone: +49 - (0)721 - 6084539
fax: +49 - (0)721 - 71173
email: joachim.ritter@gpi.uni-karlsruhe.de

Dr. Ulrich Wegler
Bundesanstalt für Geowissenschaften und Rohstoffe (BGR)
[Federal Institute for Geosciences and Natural Resources]
Geozentrum Hannover
Stilleweg 2
30655 Hannover
Germany
phone +49-(0)511-643-3867
fax +49-(0)511-643-3663
email: Ulrich.Wegler@bgr.de

Prof. Dr.-Ing. habil. Christian Grosse
Associate Director and Head of Department
Material Testing Institute MPA
University of Stuttgart
Dept. of Non-destructive Testing and Monitoring Techniques
P.O. 801140
70511 Stuttgart
Germany
phone +49-(0)711-685-66786
fax: +49-(0)711-685-66797
email: christian.grosse@mpa.uni-stuttgart.de

Noise and Diffuse Wavefields

- Extended Abstracts of the Neustadt Workshop -

**Neustadt an der Weinstraße, Germany
5 - 8 July 2009**

The Workshop was organized with the kind support of StatoilHydro.

StatoilHydro

The workshop was a joint initiative of the Deutsche Geophysikalische Gesellschaft (German Geophysical Society) and the Deutsche Gesellschaft für Zerstörungsfreie Prüfung (German Society for Non-destructive Testing).



Foreword

Christoph Sens-Schönenfelder¹, Joachim Ritter², Ulrich Wegler³, and Christian Grosse⁴

¹ Institute of Geophysics and Geology, University of Leipzig, Germany, e-mail: sens-schoenfelder@uni-leipzig.de

² Geophysical Institute, Universität Karlsruhe (TH), Germany, e-mail: joachim.ritter@gpi.uni-karlsruhe.de

³ Federal Institute for Geosciences and Natural Resources (BGR), Hannover, Germany, e-mail: ulrich.wegler@bgr.de

⁴ Material Testing Institute MPA, University of Stuttgart , Dept. of Non-destructive Testing and Monitoring Techniques, Germany, e-mail: christian.grosse@mpa.uni-stuttgart.de

Recent developments in wave theory, acoustics, seismology, data acquisition and data processing techniques throw a new light on continuous background noise and diffuse wave fields. The discovery of long-range correlations in diffuse wave fields led to a variety of applications that make use of the possibility to retrieve Green's functions of a medium without an active source.

Applications range from surface wave tomography of continents over imaging in acoustics and medicine to monitoring of volcanoes and engineering structures. The technical developments in continuous recording and data storage as well as handling large data sets were important premises for analyzing long-lasting time series. Another premise is the continuous availability of noise free of charge. The basis of the new techniques is the randomness of the noise wave field. This randomness might originate from disordered sources that generate a combined signal which is usually referred to as noise. The randomness might also stem from alteration of the coherent wave field by scattering. Fundamental research on the properties of noise and diffuse wave fields appears therefore as important as the new applications that make use of them.

This workshop intends to gather and discuss experience from all involved disciplines about noise and diffuse wave fields, their causes, properties, and use.

Content

1. The Good, the Bad, and the Ugly - Seismic Noise at Periods above 20 s <i>Walter Zürn</i>13
2. Continuous excitation of normal modes and its possible sources <i>Dieter Kurrle and Rudolf Widmer-Schnidrig</i>19
3. Seismic Noise in the City of Speyer <i>Barbara Schechiger and Alexander Goertz</i>21
4. Time Domain Classification and Quantification of Seismic Noise <i>Jörn Groos and Joachim R. R. Ritter</i>25
5. Unsupervised Recognition and Interpretation of Patterns in Continuous Seismic Wavefield Records: Application to Small-Scale Array Measurements <i>Andreas Köhler, Matthias Ohrnberger, and Frank Scherbaum</i>33
6. Ambient vibration analysis for site effect assessment – from measurement to interpretation <i>Matthias Ohrnberger</i>35
7. Array observations of a significant Love wave contribution to the ambient vibration H/V ratio <i>Brigitte Endrun and Matthias Ohrnberger</i>43
8. Building Responses Extracted from Seismic Background Signals <i>Lisa Rehor and Thomas Forbriger</i>45
9. Radiative transfer of seismic waves: theoretical approach and applications <i>Ludovic Margerin</i>49
10. Radiative Transfer of Elastic Waves in Random Media with Multiple Scales <i>Jens Przybilla, Michael Korn, and Ulrich Wegler</i>51
11. Retrieval of the Green function having coda for a scattering medium from noise correlation: the Born approximation <i>Haruo Sato</i>53
12. Detection of subtle changes in materials by Coda Wave interferometry <i>Simon Stähler, Ernst Niederleithinger, Stephan Pirskawetz, Thomas-Rudolf Nowak, and Frank Weise</i>59
13. Monitoring Temporal Changes in Seismically Active Areas Using Ambient Seismic Noise <i>Ulrich Wegler, Hisashi Nakahara, Christoph Sens-Schönfelder, Michael Korn, and Katsuhiko Shiomi</i>63
14. Temporal changes in site response associated with strong ground motion of 2004 Mw 6.6 Mid-Niigata earthquake sequences in Japan <i>Chunquan Wu, Zhigang Peng, and Dominic Assimaki</i>67
15. Energy Densities of Diffuse Seismic Fields as a Tool for Imaging <i>Francisco J. Sánchez-Sesma, Frank Scherbaum, Francisco Luzón, Miguel A. Santoyo, Antonio García-Jerez, Alejandro Rodríguez-Castellanos, Mathieu Perton, Michel Campillo, and Richard L. Weaver</i>71
16. Comparing Interferometric Migration and Mirror Imaging of 3D-VSP Free-Surface Multiples <i>Hugues Djikpesse, Shuqian Dong, Jakob Haldorsen, and Douglas Miller</i>79
17. Processing seismic ambient noise data at onshore-offshore networks <i>Andreas Schmidt and the EGELADOS working group</i>87

18. The characteristic of the cross-correlation of ambient noise for some of the stations of the German Regional Seismic Network <i>Danuta Garus and Ulrich Wegler</i>89
19. Time Reverse Localization of Sources in Non-Destructive Testing and Exploration Geophysics: Similarities and Differences <i>Erik H. Saenger, Georg Karl Kocur, Roman Jud, and Brian Steiner</i>91
20. Phase statistics of seismic coda waves <i>Ludovic Margerin, Domitille Anache-Ménier, and Bart Van Tiggelen</i>93
21. Lg-blockage in the western Pyrenees explained with locally increased heterogeneity based on radiative transfer theory <i>Christoph Sens-Schönfelder and Ludovic Margerin</i>95
22. Stability of Monitoring Weak Changes in Multiply Scattering Media with Ambient Noise Correlation: Laboratory Experiments. <i>Céline Hadzioannou, Eric Larose, Olivier Coutant, Philippe Roux, and Michel Campillo</i>97
23. Noise based seismic monitoring of the CO ₂ -Sequestration site Ketzin, Germany <i>Robert Mündel, Christoph Sens-Schönfelder, and Michael Korn</i>99
24. METSEIS: An Experiment to Quantify Meteorological and Seismological Interactions <i>Joachim Ritter, Johannes Thun, Jörn Groos, Friedemann Wenzel, and Christian Hauck</i>101
25. The Role of Modal Cross-terms in Seismic Interferometry <i>Wouter Kimman and Jeannot Trampert</i>107
26. Seismic Interferometry by cross-correlation and by multi-dimensional deconvolution sing ambient seismic noise <i>Deyan Draganov, Elmer Ruigrok, Jan Thorbecke, Jürg Hunziker, Joost v.d. Neut, and Kees Wapenaar</i>109
27. What can we learn from Greens function retrieval from ambient noise in the frequency range 1 to 10 Hz? <i>Michael Korn</i>115
28. A study of ambient seismic noise as the source for body-wave interferometry <i>Xander Campman, Deyan Draganov, Arie Verdel, and Kees Wapenaar</i>119
29. Lithospheric-scale seismic interferometry: a comparison of approaches to deal with an irregular source distribution and source-side reverberations <i>Elmer Ruigrok, Xander Campman, and Kees Wapenaar</i>125
30. Electromagnetic Interferometry by multi-dimensional deconvolution applied to diffusive controlled-source exploration <i>Jürg Hunziker, Evert Slob, and Kees Wapenaar</i>131

The Good, the Bad, and the Ugly - Seismic Noise at Periods above 20 s

Walter Zürn

Black Forest Observatory (BFO, Schiltach), Universities Karlsruhe/Stuttgart,
Heubach 206, D-77709 Wolfach, Germany, e-mail: walter.zuern@gpi.uni-karlsruhe.de

1 INTRODUCTION

Seismograms and noise are created by forces acting on the mass suspended in the seismometer's frame. At the frequencies of seismic body waves the inertial forces due to accelerations of the frame fixed to the ground are dominantly responsible for the seismograms. This allows relatively easy calculation of ground displacement, for example. However, as frequency decreases, the inertial forces (proportional to frequency squared) decrease strongly. This raises the importance of other forces on the mass, either related to the seismic phenomenon to be observed or due to ambient noise. For vertical sensors the most important forces are changes in the local gravity field due to mass redistributions and free air gravity changes due to motion in the local gravity field (e. g. at 0.28 mHz the free air gravity change equals the inertial force). For horizontal components tilts of the surface and changes of the local vertical (mass redistributions) are the most important contributions, because they bring a component of the (huge) local gravity into the sensor's sensitive direction. For example, for the horizontal accelerations by ${}_0S_2$ (0.3 mHz) the mass redistribution effect is 8.5 times, the tilt effect (with opposite sign) nearly 18 times as large as the inertial effect (Zürn and Wielandt 2007, Zürn et al. 2007).

Peterson (1993) and Berger et al. (2004) provide summaries of ambient broadband seismic noise for many stations of the global networks. Of course, the noise levels cover a wide dynamic range because seismic stations are mostly not selected for low noise but for logistical reasons (global coverage, accessibility etc.). For the best stations (among them BFO) an interesting pattern emerges at periods above 20 s. This is demonstrated with power spectral densities (PSD) of accelerations measured by the STS-1 seismometers at BFO (Fig. 1).

Horizontal noise increases strongly with increasing period from a minimum near 30 seconds (33 mHz), while the vertical noise shows two minima near 50 s (20 mHz) and 250 - 300 s (4 - 3.33 mHz) before it also rises strongly with increasing period.

Vertical noise displays a small hump between 100 and 160 s (10 and 6 mHz). In the period range where both components show strongly increasing noise as period gets longer vertical noise is almost a factor of 100 lower in PSD. Each component by itself is strongly influenced by weather. Many features of these PSDs for the most quiet stations are qualitatively, if not quantitatively understood as demonstrated in this paper.

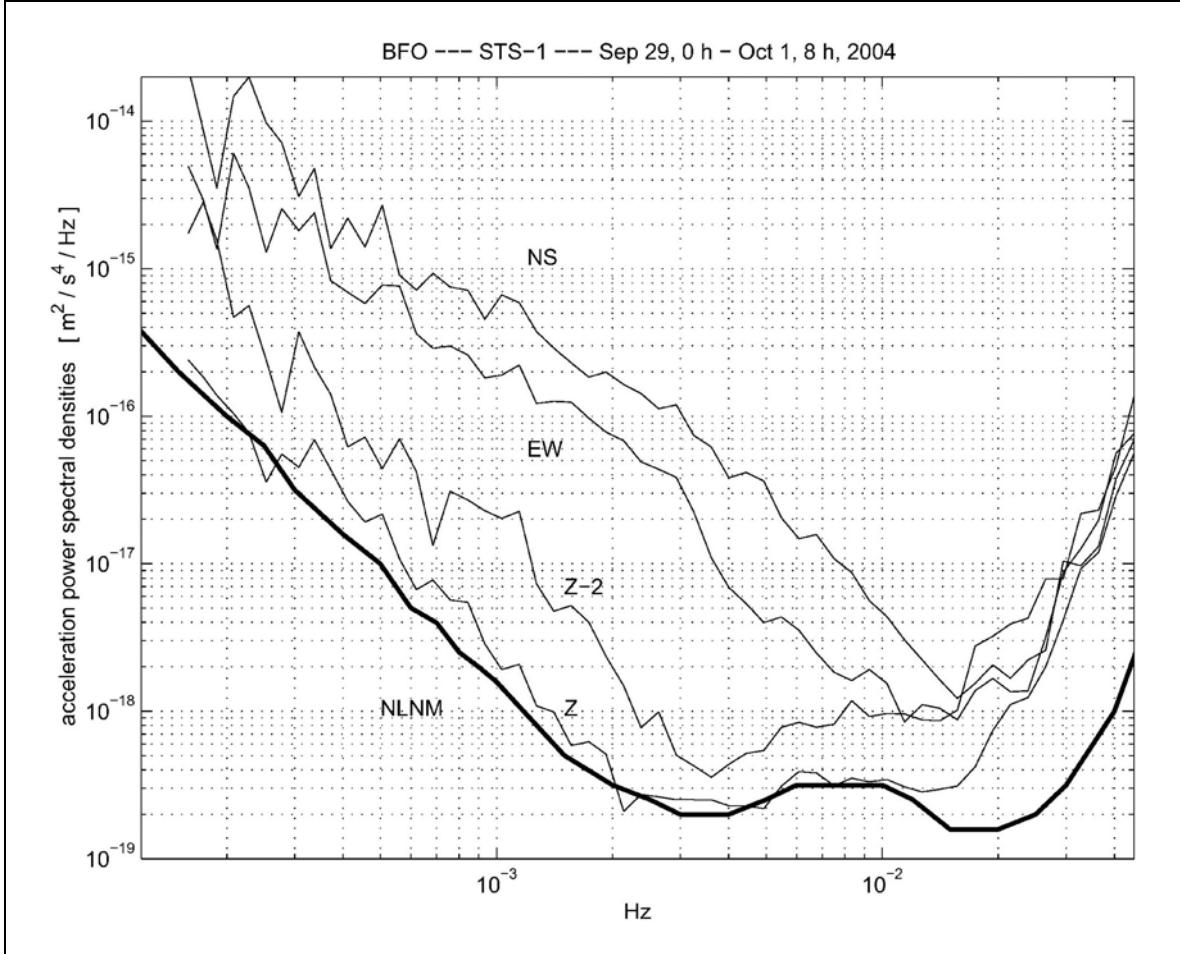


Fig. 1. Acceleration power spectral densities for 56 hour long records of the STS-1 seismometers at station BFO. Solid lines labeled Z, EW, and NS are from the corresponding components for the very quiet 56 h interval starting September 29, 0:00:00.0 GMT, 2004. Note the large difference between the vertical and horizontal components. The thick solid line represents the "New Low Noise Model" (NLNM) of Peterson (1993). Z follows the NLNM closely up to about 12 mHz. The difference between NS and EW is due to an amplification of pressure-induced noise on the former component due to a cavity effect. The curve labeled Z-2 is for the vertical component during the barometrically noisy 56 h interval starting 0:00:00.0 GMT on October 29, 2004 for comparison.

2 THE GOOD

Between about 140 and 500s (7 to 2 mHz) it can be shown that the Earth oscillates continuously with its fundamental spheroidal and toroidal modes with amplitudes of the order of at

most 10^{-12} g (background free oscillations, "hum" for short). Many vertical sensors show this phenomenon, while only a handful of seismometers provide noise levels low enough to observe the oscillations in the horizontal

component (e. g. Kurrale and Widmer-Schnidrig, 2006, 2008). Up to 50 s (20 mHz) Ekström (2001) and Nishida et al. (2002) have demonstrated that Rayleigh waves produce a background noise level in this range too. The demonstration of these phenomena needs statistical analysis, it cannot be done in a single time window of, say 12 or 24 h. This phenomenon is only mentioned briefly here because of a paper specially devoted to it.

3 THE UGLY

Seismic sensors (at very good stations) show continuous, episodic, and transient noise which is poorly or not at all understood. Clearly, all electronic components produce random and continuous noise. Digitizers are sources of digitization noise which due to the nonlinear mechanism of production might display strange properties (Zürn, 1976). According to E. Wielandt (pers. comm.) the transfer function of the STS-1 seismometers are shaped in such a way, that the dynamic range of the electronics and 24-bit digitizers accommodate the bazar of seismic signals optimally and that Earth noise is resolved over the full frequency range of seismic signals for the vertical components. The best (only) gravimeters (superconducting, LaCoste-Romberg) have proven to be superior to vertical STS-1s at periods above 1000 seconds (1 mHz), mainly because their shielding is superior (Widmer-Schnidrig, 2003). Coherence between the signals recorded by excellent vertical sensors collocated at a very good station leaves a lot to be desired, which shows that either the individual instrumental noise or different residual sensitivities to small variations of ambient conditions (e. g. temperature, air convection a. s. f.) prevent perfect

agreement between the signals. That such sensitivities exist is demonstrated by an attempt of "improving" the shielding of the STS-1/NS at BFO with disastrous effects on the quality of the data. The physical reasons for this "ugly" experience are not understood and probably still play a role when the minimum noise level is reached. Another experiment in consequence of an unusual observation was to turn a 150 W soldering iron on and off on the floor of the seismic vault at BFO with the result of a boxcar response (with decaying roof) in tiltlate with an amplitude of $5 \cdot 10^{-10}$ rad/s of the seismic pier shown by 6 horizontal broadband seismometers.

Forbriger (2007) has shown that many modern broadband seismometers are sensitive to ambient magnetic fields with widely differing sensitivities. The effect is believed to be caused by magnetization of the suspension springs made from ferromagnetic alloys. While this is an instrumental shortcoming, corrections to the recorded data can be made using records of the local magnetic field and the noise level can be lowered especially in cases of magnetic storms. However, basically this noise can be avoided by proper instrumental measures or by shielding. Vertical STS-1 components are provided with μ -metal shielding for this reason, but this is not always sufficient.

The noise discussed in the following "Bad" section cannot be avoided in principle. Even at the very best stations strong atmospheric pressure variations at the station cause strong disturbances of the seismic signals which clearly correlate with atmospheric pressure. This involves all components, with

horizontals (and strainmeters) affected more strongly than the verticals.

4 THE BAD

In Earth tide research it is well known that after removing the tides from gravimeter records the residual gravity clearly shows a strong correlation with the local barometric pressure (Warburton and Goodkind, 1977). The regression coefficients are of the order of 3.5 $\text{nms}^{-2}/\text{hPa}$. This is well understood as the gravitational attraction of the sensor mass by the air above the station, which changes its density with time and this density change also expresses itself as a change in the local barometric pressure. In addition, the pressure pushes on the surface with changing amplitude and causes smaller opposite acceleration changes due to the free air and inertial effect. I show several examples where the frequency-independent regression factor is used to correct the recorded data successfully (e.g. Zürn and Widmer, 1995). Zürn and Wielandt (2007) argue that since the inertial effect rises with frequency-squared, there should be a notch in the transfer-function from pressure to gravity at a frequency where the gravitational effect cancels the opposite free air and inertial effects. Using simple models of atmosphere and crust transfer-functions can be computed and it is shown that for reasonable parameters the notch is in the vicinity of about 300 s (3.3 mHz). Of course, one has to expect that this notch-frequency is not a stable property of the atmosphere in reality. Zürn and Wielandt (2007) claim that the minimum in Peterson's (1993) "New Low Noise Model" for vertical acceleration is probably caused by this cancellation effect of the atmospherically caused noise. Instrumental noise and the "hum"

prevent the notch to become really deep. Ultimately this partial cancellation of atmospheric noise is the reason why the "hum" can be detected by many vertical sensors. I also can demonstrate with a unique record from the superconducting gravimeter in Vienna, that frequency-dependent admittances perform better in reducing noise in the vicinity of 300 s than any frequency independent admittance does (Zürn and Meurers, 2009). This observation strongly corroborates the conjecture of cancelling effects in vertical components.

In contrast, for horizontal components the tilt, inertial and gravitational contributions from local atmospheric variations have all the same sign, so they enforce each other. This is discussed by Zürn and Wielandt (2007) in their "Gedankenexperiments". Again simple models can be used to calculate transfer-functions between local atmospheric pressure and horizontal accelerations (Zürn et al. 2007). Our first model conjectures, that on a complicated topography of the surface and in cavities inside hills all displacements are proportional to the atmospheric pressure above the station (local deformation model). This effect is in phase with the barometric pressure. Our second model consists of a sinusoidal pressure wave travelling (quasistatically) horizontally over an elastic halfspace (traveling wave model). For that one all the effects are in phase with each other but in quadrature to the pressure change. Especially the tilt effect turns out to be proportional to the Hilbert transform of the pressure. It also turns out that the tilt signal for realistic parameters dominates at the long periods. Thus we have two orthogonal signals ("pressure seismograms") we can fit to the recorded seismogram to obtain

regression coefficients for the two models simultaneously. I show several examples where we succeed in appreciably reducing the noise especially in situations where atmospherically caused noise is high.

5 SUMMARY

Looking again at Fig. 1 the situation above 20 s is summarized. As a caveat I mention in passing, that the distant atmosphere and oceans produce noise worldwide continuously and episodically by exciting seismic surface waves (besides the well-known primary and secondary marine microseisms). Evidence for this to be the case comes from the observations of the "hum" and occasional very large signals from volcanoes (El Chichón, Mt. Pinatubo; Widmer and Zürn, 1992; Kanamori et al. 1994).

Acknowledgements

I would like to thank the colleagues Udo Neumann, Thomas Forbriger, Erhard Wielandt, Rudolf Widmer-Schnidrig, and Bruno Meurers for discussions and for making very helpful comments on the manuscript. Financial support by the "Deutsche Forschungsgemeinschaft" under grants number KR 1906/3-1 and WE 2628/1-1 is gratefully acknowledged.

References

- Beauduin, R., P. Lognonné, J. P. Montagner, S. Cacho, J. F. Karczewski and M. Morand (1996). The Effects of Atmospheric Pressure Changes on Seismic Signals or How to Improve the Quality of a Station. *Bull. seism. Soc. Am.*, 86: 1760 - 1769. Berger, J., P. Davis and G. Ekström (2004). Ambient Earth Noise: A Survey of the Global Seismographic Network. *J. geophys. Res.*, 109, B11307, doi: 10.1029/2004JB003408.
- Ekström, G. (2001). Time domain analysis of Earth's long-period background seismic radiation. *J. geophys. Res.*, 106: 26483 - 26493.
- Forbriger, T. (2007). Reducing magnetic field induced noise in broad-band seismic recordings. *Geophys. J. Int.*, 169: 240 - 258. doi: 10.1111/j.1365-246X.2006.03295.x.
- Kanamori, H., Mori, J., Harkrider, D. G. (1994). Excitation of Atmospheric Oscillations by Volcanic Eruptions. *J. geophys. Res.*, 99: 21947 - 21961.
- Klinge, K., Kroner, C., Zürn, W. (2002). Broadband Seismic Noise at Stations of the GRSN. In: *Ten Years of German Regional Seismic Network* (M. Korn, Ed.), Wiley-VCH, Weinheim, Germany, 83 - 101.
- Kurrale, D., Widmer-Schnidrig, R. (2006). Spatiotemporal features of the Earth's background free oscillations observed in Central Europe. *Geophys. Res. Lett.*, 29: L24304, doi: 10.1029/2006GL028429.
- Kurrale, D., Widmer-Schnidrig, R. (2008). The horizontal hum of the Earth: A global background of spheroidal and toroidal modes. *Geophys. Res. Lett.*, 35: L06304, doi: 10.1029/2007/GL033125.
- Lognonné P., Clévédé, E., Kanamori, H. (1998). Computation of seismograms and atmospheric oscillations by normal-mode summation for a spherical earth model with realistic atmosphere. *Geophys. J. Int.*, 135: 388 - 406.

- Meurers, B. (2000). Gravitational effects of atmospheric processes in SG gravity data. Cah. Centre Europ. Geodyn. Seismol., 17: 57 - 65.
- Müller, T. and W. Zürn (1983). Observation of gravity changes during the passage of cold fronts. J. Geophys., 53: 155 - 162.
- Nishida, K., Kobayashi, N., Fukao, Y. (2002). Origin of Earth's ground noise from 2 to 20 mHz. Geophys. Res. Lett., 29, doi: 10.1029/2001GL013862.
- Peterson, J. (1993). Observations and Modeling of Seismic Background Noise. U. S. Geol. Surv., Open-FileRep., 93-322: 1 - 45.
- Richter, B., Wenzel, H.-G., Zürn, W., Klopping, F. (1995). From Chandler Wobble to Free Oscillations: Comparison of Cryogenic Gravimeters and Other Instruments in a Wide Period Range. Phys. Earth planet. Inter., 91: 131 - 148.
- Sorrells, G. G. (1971). A preliminary investigation into the relationship between long-period seismic noise and local fluctuations in the atmospheric pressure field. Geophys. J. R. astr. Soc., 26: 71 - 82.
- Steffen, H., Kuhlmann, S., Jahr, T., Kroner, C. (2005). Numerical modelling of the barometric pressure-induced noise in horizontal components for the observatories Moxa and Schiltach. J. Geodyn., 41, 242 - 252.
- Warburton, R. J., Goodkind, J. M. (1977). The influence of barometric pressure variations on gravity. Geophys.J. R. astr. Soc., 48: 281 - 292.
- Widmer-Schnidrig, R. (2003). What Can Superconducting Gravimeters Contribute to Normal-Mode Seismology. Bull. seism. Soc. Am., 93: 1370 - 1380.
- Widmer, R., Zürn, W. (1992). Bichromatic excitation of long-period Rayleigh and air waves by the Mount Pinatubo and El Chichon volcanic eruptions. Geophys. Res. Lett., 19: 765 - 768.
- Zürn, W. (1974). Detectability of Small Harmonic Signals in Digitized Records. J. geophys. Res., 79: 4433 - 4438.
- Zürn, W. (2009). Clear evidence for the sign-reversal of the pressure admittance to gravity near 3 mHz. accepted by J. Geodyn
- Zürn, W., Exß, J., Steffen, H., Kroner, C., Jahr, T., Westerhaus, M. (2007). On reduction of long-period horizontal seismic noise using local barometric pressure. Geophys. J. Int., 171, 780-796, doi: 10.1111/j.1365-246X.2007.03553.x
- Zürn, W. and Widmer, R. (1995). On noise reduction in vertical seismic records below 2 mHz using local barometric pressure. Geophys. Res. Lett., 22: 3537 - 3540.
- Zürn, W., Wielandt, E. (2007). On the minimum of vertical seismic noise near 3 mHz. Geophys. J. Int., 168, 647 - 658, doi: 10.1111/j.1365-246X.2006.03189.x

Continuous excitation of normal modes and its possible sources

Dieter Kurrle^{1,3}, Rudolf Widmer-Schnidrig^{2,3}

¹ Department of Earth and Environmental Sciences – Geophysics, Ludwig-Maximilians-Universität München, München D-80333, Germany, E-Mail: dieter.kurrle@geophysik.uni-muenchen.de

² Black Forest Observatory (BFO), Universities of Karlsruhe and Stuttgart, Wolfach D-77709, Germany, E-Mail: widmer@geophys.uni-stuttgart.de

³ Institute of Geophysics, University of Stuttgart, Stuttgart D-70174, Germany

Ten years ago, it was reported for the first time that the free oscillations of the Earth can be observed permanently and not only in connection with strong earthquakes (e.g., Suda et al. 1998). It was shown that between 2 and 7 mHz, all fundamental spheroidal modes, ${}_0S_1$, are evident in spectra of vertical seismic noise recorded at quiet stations. As was shown later, the frequency range of these background oscillations extends to 20 mHz (Nishida et al. 2002). Thus, the minimum of the New Low Noise Model (NLNM, Peterson 1993, see Figure 1) in this frequency range is defined by a globally uniform geophysical signal rather than instrumental or locally generated seismic noise.

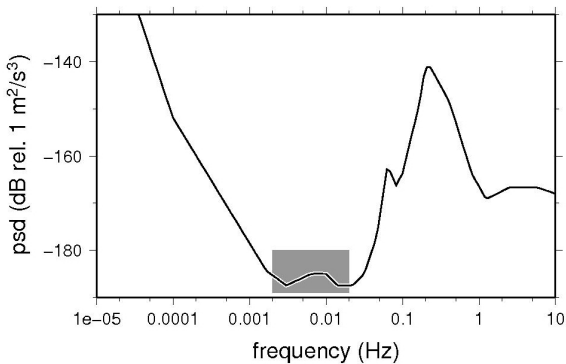


Figure 1. New Low Noise Model by Peterson (1993). The frequency band of background oscillations is marked by a gray box.

Since then, it was assumed that the background oscillations are caused by normal forces exerted on the solid Earth, either by atmospheric or ocean bottom pressure. The lack of overtones as well as observations of seasonal amplitude variations and shifting source areas corroborated the assumption that the background oscillations are related to processes outside the solid Earth. Recent

results argue for an excitation by ocean waves, similar to microseisms observed at higher frequencies.

Most recently, however, we showed that not only the fundamental spheroidal but also the fundamental toroidal oscillations are excited continuously (see Figure 2, Kurrle and Widmer-Schnidrig 2008).

Surprisingly, both kinds of modes show equal amplitudes. This seems to contradict an excitation by pressure forces which should lead to a predominance of spheroidal modes, even when effects of topography and bathymetry are taken into account. Similarly, based on coupling strengths in this frequency band determined from earthquake observations, it seems unlikely that the toroidal modes are excited only indirectly by spheroidal-toroidal mode coupling.

At present, it is not clear whether spheroidal and toroidal modes are excited together or independently. In case of an independent excitation, horizontal shear forces that selectively couple into toroidal modes are required. Such forces might be exerted by winds, ocean bottom currents or coastal waves.

If, on the other hand, the spheroidal and toroidal background oscillations have a common source, an excitation mechanism which causes similar amplitudes for spheroidal and toroidal modes is needed.

Again, horizontal forces seem to be the most promising way to explain the observations, whereas an additional excitation of spheroidal modes by vertical pressure forces seems to contradict the observations.

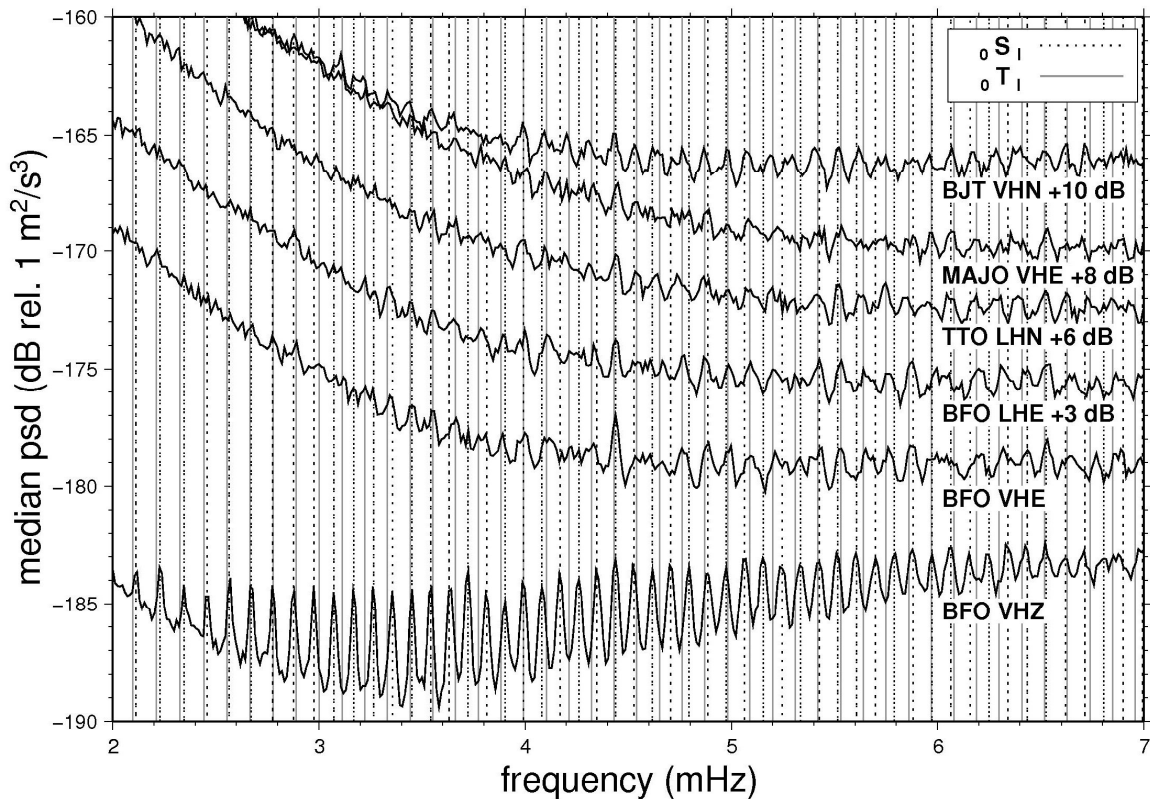


Figure 2. Median power spectral densities for some seismic channels with particular low noise levels. For each channel, the median of the 1000 quietest 24h-spectra out of a period between 8 and 13 years was computed. Some of the horizontal spectra have been vertically shifted for clarity. While the vertical spectrum consists only of spheroidal modes, the horizontal spectra indicate the presence of spheroidal as well as toroidal modes.

References

- Kurrale, D. and R. Widmer-Schnidrig, The horizontal hum of the Earth: A global background of spheroidal and toroidal modes, *Geophys. Res. Lett.*, v. 35(6), L06304, doi:10.1029/2007GL033125, 2008.
- Nishida K., N. Kobayashi, and Y. Fukao, Origin of Earth's ground noise from 2 to 20 mHz, *Geophys. Res. Lett.*, v. 29 (10), 1413, doi:10.1029/2001GL013862, 2002.
- Peterson, J., Observations and Modeling of Seismic Background Noise, USGS Open File Report, 93-322, 1993.
- Suda, N., K. Nawa and Y. Fukao, Earth's background free oscillations, *Science*, v. 279, 2089-2091, 1998.

Seismic Noise in the City of Speyer

Barbara Schechiger¹, Alexander Goertz¹

¹ Spectraseis AG, Zürich, Switzerland. E-mail: barbara.schechinger@spectraseis.com

A passive seismic survey was carried out in and around the city of Speyer which is located in the Rhinegraben in southwestern Germany. The survey was located above an oil field with the aim to analyze variations in the naturally occurring seismic noise that can indicate the presence of hydrocarbons in the subsurface (Lambert et al., 2009; Sänger et al., 2009; Van Mastrigt, 2008).

The survey consisted of 2 lines with 25 stations each (Fig. 1). The length of each line was ca. 7.5 km with a station spacing of approximately 300 m. Each station was equipped with a Nanometrics T40 three-component broad band seismometer buried in a hole, a digitizer, and a GPS unit. All stations were recording synchronously over a weekend for ~48 hours.

When planning such a survey in a city like Speyer with 50'000 inhabitants, it is unavoidable to have station locations in the vicinity of noise sources. They have to be identified and characterized in order to remove the noise from the data before analyzing the spectra. In the following, noise sources of various anthropogenic origins are discussed.

As in many locations around the world, a day/night variation of seismic noise background is observed. Additionally, there is a weekly variation with the quietest time occurring during the night from Saturday to Sunday. Fig. 2 compares average power spectral density (PSD) of three representative stations for Saturday night and Sunday noon. All spectra have a dominant and stable microseism peak at 0.2 – 0.3 Hz. However, for frequencies above 0.5 Hz we observe an almost constant offset between day and night data. During day time, the general spectral level reaches the New High Noise Model (Peterson, 1993). For frequencies above ca. 3 Hz variations between individual locations become significant due to their local noise characteristics.

Stationary noise originating from rotating machinery is observed widely in an urban environment. Spectra of all stations show a narrow-band peak at 2.083 Hz (arrows in Fig. 3) which is the rotation frequency of a 48 pole power generator in the 50 Hz power grid (Bokelmann & Baisch, 1999). Such narrow spectral spikes can be easily removed by despiking techniques. Stationary noise is observed at several other frequencies, particularly at stations located in the industrial quarter along line 1 (Fig. 3a). Some of the peaks have a distinct on/ off pattern whereas others show no interruptions.

Another major source of noise is the traffic. Due to its transient character, traffic events can be edited out of the data in the time domain. Since the station layout crosses federal highways where traffic events occur quite frequently, we use a statistical approach to edit them out. This approach is based on the average spectral level over a specified frequency band calculated for 40 seconds time intervals.

Strong noise is created by the barge traffic on Rhine River. The spectrogram of a station located at the west bank is shown in Fig. 3b. The ship's propeller causes a narrow band signal at 5-6 Hz lasting for about 30 minutes while the ship passes by. This frequency varies between ships, and it is possible to observe a Doppler shift. Additionally, strong broadband noise is generated by the ship's engine as it approaches closer to the station.

The observed noise is studied in more detail by doing a polarization analysis in the time-frequency domain (Kulesh et al., 2007). For the narrow banded propeller noise of the river barges it shows a well defined azimuth varying with time and pointing towards the moving source.

References

Bokelmann, G.H.R., and Baisch, S., Nature of Narrow-Band Signals at 2.083 Hz, Bull. Seis. Soc. Am., Vol. 89 (1), pp. 156 – 164, 1999.

Kulesh, M., Diallo, M.S., Holschneider, M., Kurennaya, K., Krüger, F., Ohrnberger, M., and Scherbaum, F., Polarization analysis in the wavelet domain based on the adaptive covariance method, Geophys. J. Int., Vol. 170 (2), pp. 667 – 678, 2007.

Lambert, M., Schmalholz, S.M., Sänger, E.H., and Steiner, B., Low-frequency microtremor anomalies at an oil and gas field in Voitsdorf, Austria, Geophysical Prospecting, in press, doi: 10.1111/j.1365-2478.2008.00734.x, 2009.

Peterson, J., Ambient earth noise: Observations and modeling of seismic background noise, U.S. Geol. Survey Open-File Report 93-322, 1993.

Sänger, E.H., Schmalholz, S., Metzger, S., Habiger, R., Müller, T., and Rentsch, S., A passive seismic survey over a gas field: Analysis of low-frequency anomalies, Geophysics, Vol. 74 (2), pp. 29 – 40, 2009.

Van Mastrigt, P., and Al-Dulaijan, A., Seismic spectroscopy using amplified 3D geophones, 70th Ann. Internat. Mtg., EAGE Expanded Abstracts, B047, 2008.

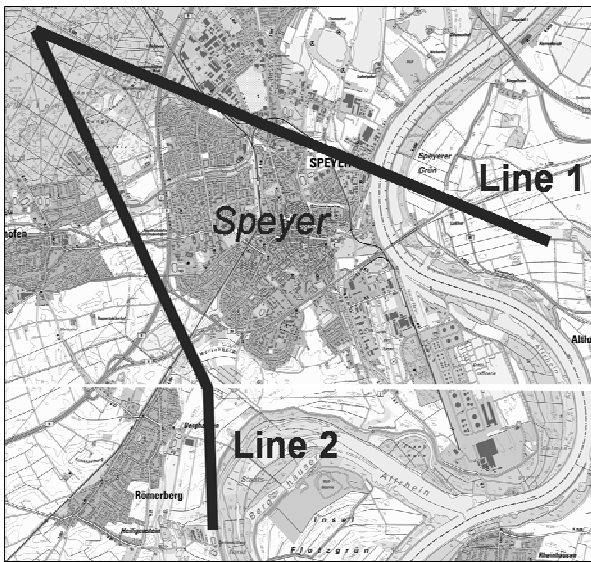


Fig. 1: Map showing the location of the passive seismic survey in Speyer. The two lines are crossing the industry quarter of Speyer, the federal highways, and the Rhine River.

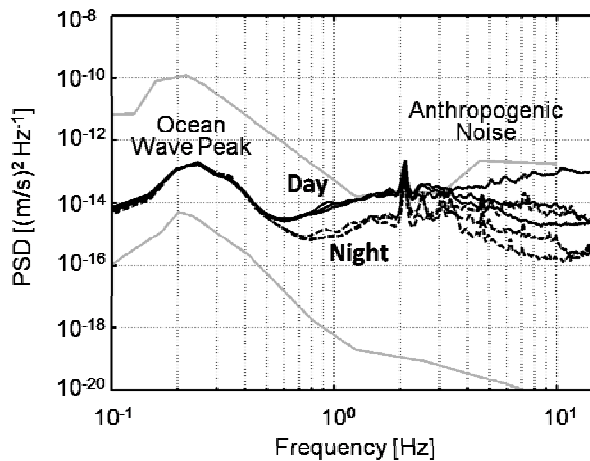


Fig. 2: Average spectra of three representative stations at day (solid lines) and at night (dashed lines) compared to the New Global Noise Model (grey lines).

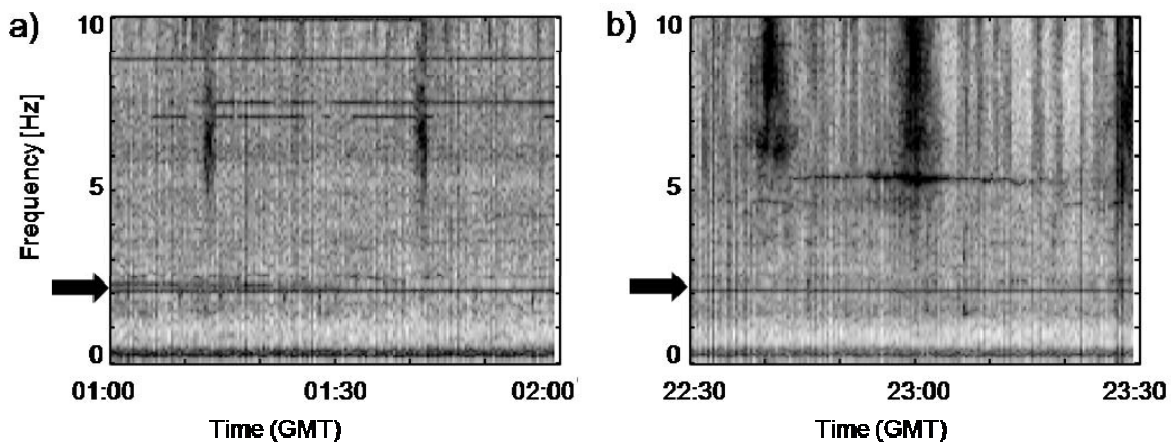


Fig. 3: Spectrograms of two selected stations. The stationary 2.083 Hz peak is indicated by the arrows.
 3a): Spectrogram of a station located in the industry quarter showing narrow band stationary noise at several frequencies as well as transient event caused by local traffic.
 3b): Spectrogram of a station located at the west dike of Rhine River showing noise caused by barge traffic: a narrow band noise around 6 Hz and a strong broadband noise when the ship is close. (Local time: GMT + 2 hours)

Time Domain Classification and Quantification of Seismic Noise

Jörn Groos¹, Joachim R. R. Ritter¹

¹ Geophysikalisches Institut, Universität Karlsruhe (TH), Germany, E-mail: joern.groos@gpi.uni-karlsruhe.de, joachim.ritter@gpi.uni-karlsruhe.de

Introduction

Currently several efforts are undertaken in seismology to retrieve information about the underground from ambient seismic noise (e.g. Curtis et al. 2006; Shapiro et al. 2005; Sens-Schönfelder & Wegler 2006).

Such studies are especially interesting in areas where traditional seismic methods are complicated such as remote areas with poor access and cities. E.g. a large number of passive seismic measurements in urban environments are undertaken with the aim to provide the required underground information for seismic hazard assessment. Seismological research must significantly improve the understanding of (urban) seismic noise to successfully and reliably apply these new methods in urban environments (Bonnefoy-Claudet et al. 2006; Campillo 2006). A good knowledge of the seismic noise conditions and contributing noise sources are crucial to select adequate time windows of available long-term data or to design short-term measurements.

We present a statistical classification scheme in the time domain to quantify and characterise seismic noise. The character of seismic noise (e.g. Gaussian distributed or dominated by single signals) is represented by only six noise classes. This approach allows us to easily visualise the seismic noise properties (amplitude and statistical properties). Furthermore, it provides a reduced dataset from broadband seismic waveforms to analyse temporal and spatial changes of seismic noise conditions.

Dataset

The proposed classification scheme was developed to analyse the urban seismic noise (USN) dataset collected during the URban Seismology (URS) project (Ritter et al. 2005). The URS project was conducted in Bucharest (Figure 1), the capital of Romania, whose 2.5 million inhabitants are endangered by devastating earthquakes from the Vrancea subduction zone (for a comprehensive review see Wenzel et al. 1999). The measurements within the URS project were conducted with the KArlsruhe BroadBand Array (KABBA) owned by the Universität Karlsruhe (TH), Germany. The URS dataset was recorded with 32 24-bit dataloggers (EarthData) and 22 Streckeisen STS-2 (fundamental period $T_0=120$ s), five Geotech KS-2000 ($T_0=100$ s), two Guralp CMG40T ($T_0=30$ s), one Guralp CMG3ESP ($T_0=30$ s) and two Lennartz LE3D/5s ($T_0=5$ s) seismometers.

These stations were deployed at 34 different sites within the metropolitan area of Bucharest from October 2003 until August 2004 (Figure 1). The instruments were mainly located in cellars of public and private buildings.

Noise classification

Broadband (urban) seismic noise must be considered as a temporally and spatially non-stationary random process. This random process is generated by an unknown number of signals emitted by numerous independent and spatially distributed sources with unknown properties. Such a summation of an infinite large number of independent signals can be expected as Gaussian distributed as expressed by the central limit theorem.

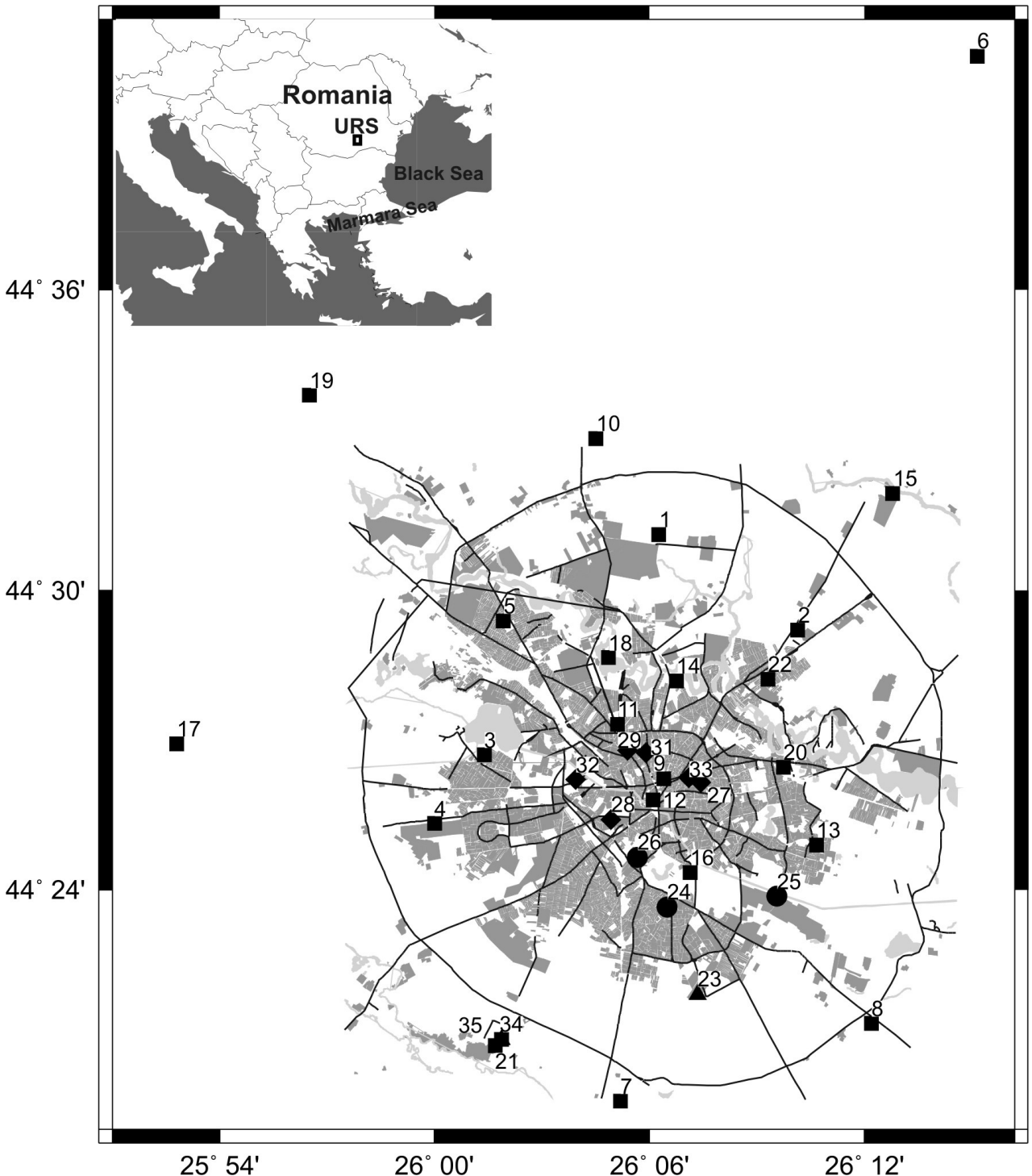


Figure 1: Station network of the URban Seismology (URS) project in Bucharest, Romania and its surroundings. Different symbols indicate different sensor types, squares: 22 Streckeisen STS-2, diamonds: 5 Geotech KS-2000, circles: 3 Guralp CMG40T and CMG3ESP, and triangles: 2 Lennartz LE3D/5s. The inset displays the regional context.

Nevertheless, finite time series of seismic noise may exhibit deviations from the Gaussian distribution due to the emergence of single or few dominating signals above the background signal. By analysing 4 hours long time windows of urban seismic noise in Bucharest, we observed several common deviations of their histograms (sample value

distributions of the time series) from the Gaussian distribution. Most common deviation from the Gaussian distribution is a positive kurtosis of the histogram due to the presence of transient signals with short duration (seconds to minutes) and large amplitudes in comparison to the background signal (Figure 2c+d). Less common are bell-

shaped or multi-modal histograms with a negative kurtosis (Figure 2e). These deviations are most commonly caused by the dominance of long-lasting periodic signals. In rare cases we observed time series with asymmetric histograms due to the presence of asymmetric signals (Figure 2f).

We utilise ratios of amplitude intervals (I) and percentiles (P) to identify and quantify the deviations of the time series histogram from the Gaussian distribution. In the case of a zero mean Gaussian distribution, 68% of the measurements lie within an interval of one standard deviation away from zero (I68). 95.45% are within two times the standard deviation (I95) and 99.73% are within three times the standard deviation (I99). This is also known as the 2σ and 3σ , or the ‘empirical’, rule. Furthermore, the ratios of the lower and upper boundaries of the intervals (e.g. the 16-percentile (P16) and the 84-percentile (P84) for I68) can reveal a possible skewness of the histogram and can be used as a symmetry measure.

The intervals I95 and I99 are indicated by solid (I95) and dash-dot (I99) lines at the corresponding percentiles in Figure 2. The ratios between the intervals (I68, I95 and I99) and the corresponding percentiles of the time series are used to classify the seismic noise time series. Basic idea is that the interval ratios increase in the case of a positive kurtosis and decrease in the case of a negative kurtosis of the histogram. We introduce the ratio between I99 and I95 as the quantity peakfactor (pf) to determine the kurtosis of the histogram. The peakfactor of a Gaussian distributed time series equals 1.5. The range of the 68%-interval is used for quantification and called ‘noise amplitude’.

We introduce six noise classes to classify the typically observed deviations from the Gaussian distribution (Figure 2). Time series are assumed to be Gaussian distributed if the interval ratios exhibit only very small

deviations from the empirical rule and the histograms are symmetric (see Table 1). Gaussian distributed time series are classified as noise class 1 (NC1, Figure 2a).

Noise class	I95/ I68	I99/ I68	P84/ P16	P97.5/ P2.5
1	2 ± 0.05	3 ± 0.15	1 ± 0.015	1 ± 0.015

Table 1: Criteria for the interval and percentile ratios to classify a time series as Gaussian distributed (NC1).

Non-Gaussian symmetric time series (see Table 2) are classified as NC2-NC5 depending on the observed deviation properties. Time series which exhibit determinable but rather small and unspecific deviations from the Gaussian distribution ($pf = 1.5 \pm 0.1$) are classified as noise class 2 (Table 2 and Figure 2b). Time series with a gentle positive kurtosis ($1.6 < pf \leq 2.0$) due to few transient signals are classified as noise class 3 (Figure 2c). A more pronounced positive kurtosis of the histogram ($pf > 2$) results in a classification of the time series as noise class 4 (Figure 2d). Symmetric time series with a negative kurtosis ($pf < 1.4$) are classified as noise class 5 (Figure 2e).

NC	peakfactor	P84/ P16	P97.5/ P2.5
2	1.5 ± 0.1	1 ± 0.03	1 ± 0.047
3	$1.6 < pf \leq 2.0$	1 ± 0.03	1 ± 0.047
4	$2.0 < pf$	1 ± 0.03	1 ± 0.047
5	$pf < 1.4$	1 ± 0.03	1 ± 0.047

Table 2: Criteria for the interval and percentile ratios to classify symmetric time series as noise classes NC2-NC5.

All time series which are not identified as symmetric time series (see Table 2) are classified as noise class 6.

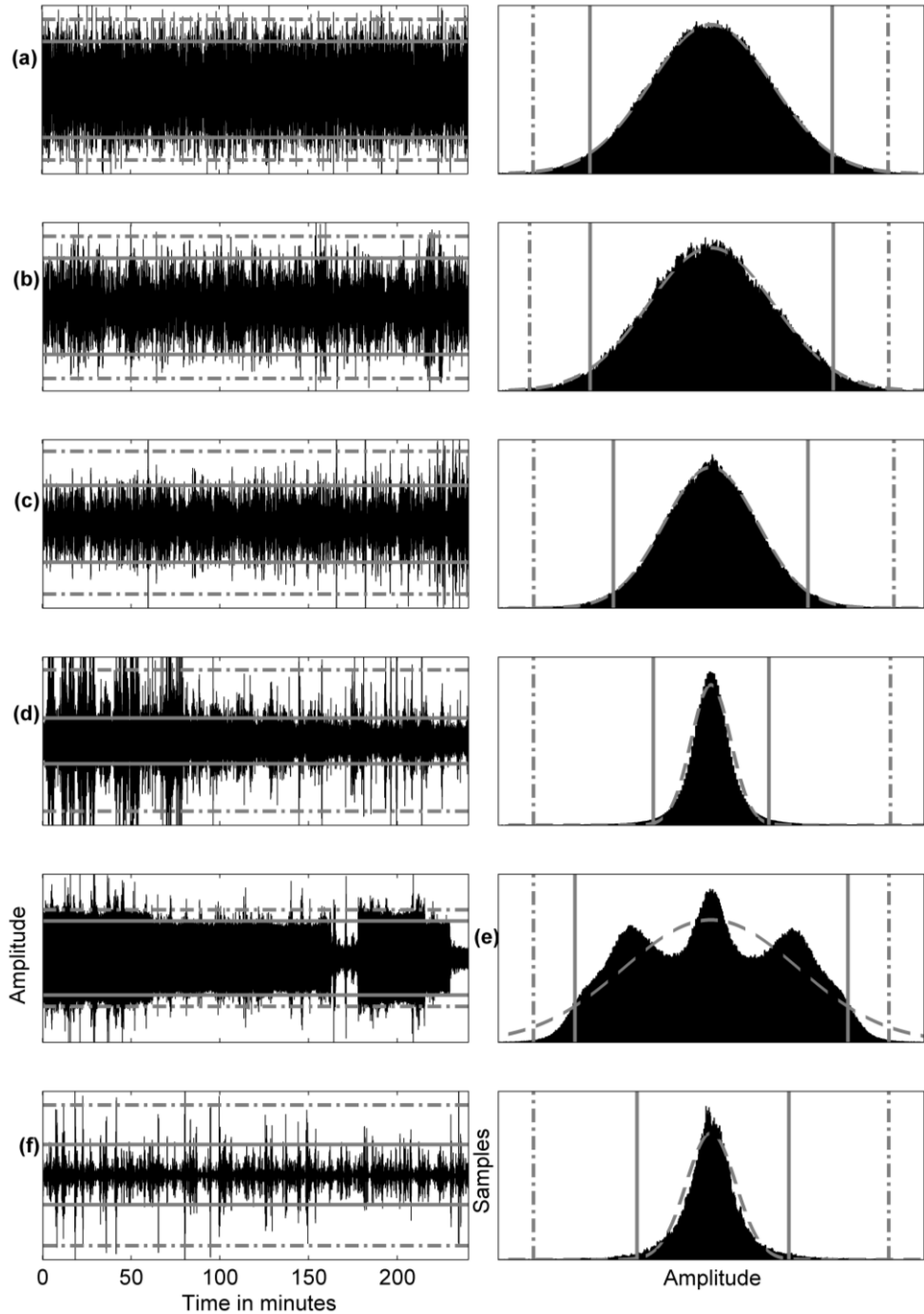


Figure 2: Time series (left) of vertical component urban seismic noise (USN) recorded in Bucharest and their histograms (distribution of sample values) (right) together with the Gaussian distributions (dashed lines) estimated from the mean and the upper boundary of the 68%-interval of the corresponding time series. The 95.45- (solid lines) and 99.73- (dash-dot lines) intervals are indicated, corresponding to the 2σ and 3σ range respectively for a Gaussian distributed time series. (a) Gaussian distributed time series of the USN(0.25-0.6 Hz) at site URS02 with a peakfactor of 1.47. (b) Nearly Gaussian distributed time series (NC2) of the USN(0.04-0.09 Hz) at site URS06 with a peakfactor of 1.48. The minor deviations from the Gaussian distribution are small and caused by short transient events with double-amplitudes larger than the range of the 99.73%-interval (left panel). (c) Time series of the USN(0.18-0.25 Hz) at site URS04 dominated by short transient noise signals (NC3) resulting in a peakfactor of 1.85. The histogram is slightly deformed at the tails in comparison to the estimated Gaussian distribution. (d) Time series of the USN(1-25 Hz) at site URS01 dominated by short transient noise signals (NC4) resulting in a peakfactor of 3.1. The histogram is heavily deformed at the tails in comparison to the estimated Gaussian distribution. (e) Time series of the USN(1-25 Hz) at site URS20 with a peakfactor of 1.3 and a non bell shaped multi-modal distribution (NC5). The displayed time series is dominated by sinusoidal signals. (f) Time series of the USN(0.04-0.09 Hz) at site URS26 with an asymmetric distribution (NC6) due to the dominance of asymmetric signals.

Noise analysis

We calculated long-term spectrograms of up to 28 days duration to identify the frequency-dependent behaviour of the time-variable seismic noise in Bucharest. We selected several frequency ranges between 8 mHz and 45 Hz for the time domain classification to capture the frequency-dependent variability of seismic noise. Furthermore we selected 3 time windows with 4 hours duration (0-4, 8-12 and 13-17 local time) for the noise classification to capture the temporal variability of the urban seismic noise with daytime. The results of the time domain classification for the urban seismic noise in Bucharest are given in four frequency ranges (Table 3). These frequency ranges are dominated by ocean-generated microseism (0.09-0.18 Hz), wind (0.6-1 Hz) and human activity (0.6-45 Hz).

Frequency/Hz	Dominating noise sources
0.09-0.18	secondary ocean-generated microseism
0.6-1	wind, human activity
1-25	human activity
25-45	human activity

Table 3: Frequency ranges for the statistical time-series analysis. Depending on the frequency range different noise sources dominate the urban seismic noise in Bucharest.

The noise conditions in terms of noise amplitudes and noise classes are visualised for the 4 hours long time windows at day and night by noise maps of the metropolitan area of Bucharest (Figure 3). The range of the 68%-interval is given as noise amplitude by colour and the noise classification is given as symbol at the station site. The noise amplitudes are interpolated between station sites for visualisation. These maps are tools to analyse large amounts of output data and are not intended to estimate noise amplitudes between station sites.

The influence of human activity can be observed by statistical properties which systematically vary with daytime in the frequency ranges between 0.09 and 45 Hz. The temporal varying amount of transient and periodic man-made signals contributing to the urban seismic noise (USN) significantly

influences the histograms of the analysed time windows.

In the frequency range 0.09-0.18 Hz natural sources of seismic energy, especially secondary ocean-generated microseism, dominate the USN in Bucharest. Due to the larger amplitudes of these naturally induced seismic waves the influence of human activity is not as obvious as at higher frequencies larger than 1 Hz as found from the variation of noise amplitudes between day and night. Nevertheless, the influence of human activity can be observed by changes of the statistical properties with daytime. The amount of time series with significant deviations from the Gaussian distribution (NC3-NC6) increases from less than 20% at night to more than 40% at day. Besides the temporal variability of USN(0.09-0.18 Hz) noise amplitudes in correlation with the ocean-generated microseism, we observe a systematic spatial variation of noise amplitudes. The noise amplitudes increase from the southern part of the metropolitan area towards north. The same spatial effect of ground motion amplification was observed by two amplitude and site effect studies utilising earthquake signals and is explained with resonance effects in the unconsolidated sediments above the dipping Neogene-Cretaceous boundary (Sudhaus & Ritter 2009; Mandrescu et al. 2004). Our similar observation for the noise amplitudes demonstrates the potential of noise amplitude mapping to complement information for site effect studies.

In the frequency range 0.6-1 Hz urban seismic noise in Bucharest is dominated by man-made ground motion as long as the wind velocity is below 3 m/s (Figure 3). The spatial variation of noise amplitude is in well correlation with the varying density of population indicated by an increase of noise amplitudes towards the city centre (Figure 3). Uncommonly large noise amplitudes are observed in vicinity (<500 m) to a heavy industry area in the south-eastern part of Bucharest (Figure 3). The large amount of man-made transient signals during the day results in Gaussian distributed seismic noise at most station sites. At night the remaining transient signals cause significant deviations from the Gaussian

distribution (Figure 3). With wind velocities exceeding 3 m/s the USN is increasingly dominated by wind-induced ground motion. This change of the dominating noise source is accompanied by significant changes of the spatial noise amplitude distribution and the statistical properties.

In the frequency range 1-45 Hz man-made transient signals characterise the USN in Bucharest at day and night. The noise amplitudes in the frequency ranges 1-25 Hz and 25-45 Hz increase towards the city centre at day and night. Inside the inner city area we observe a heterogeneous spatial distribution of the highest noise amplitudes. The amplitude increase corresponds in principle

very well with the increasing population density towards the city centre. However, at some sites distinct higher amplitudes are observed. Except the city centre sites all sites with high noise amplitudes are in vicinity (<500 m) of busy heavy industry areas.

Outlook

Our classification scheme is able to discriminate different seismic noise situations on a quantitative basis. It works well in a complicated area such as a lively city with numerous noise sources. Further studies are under way to apply this method to other seismological and technical situations.

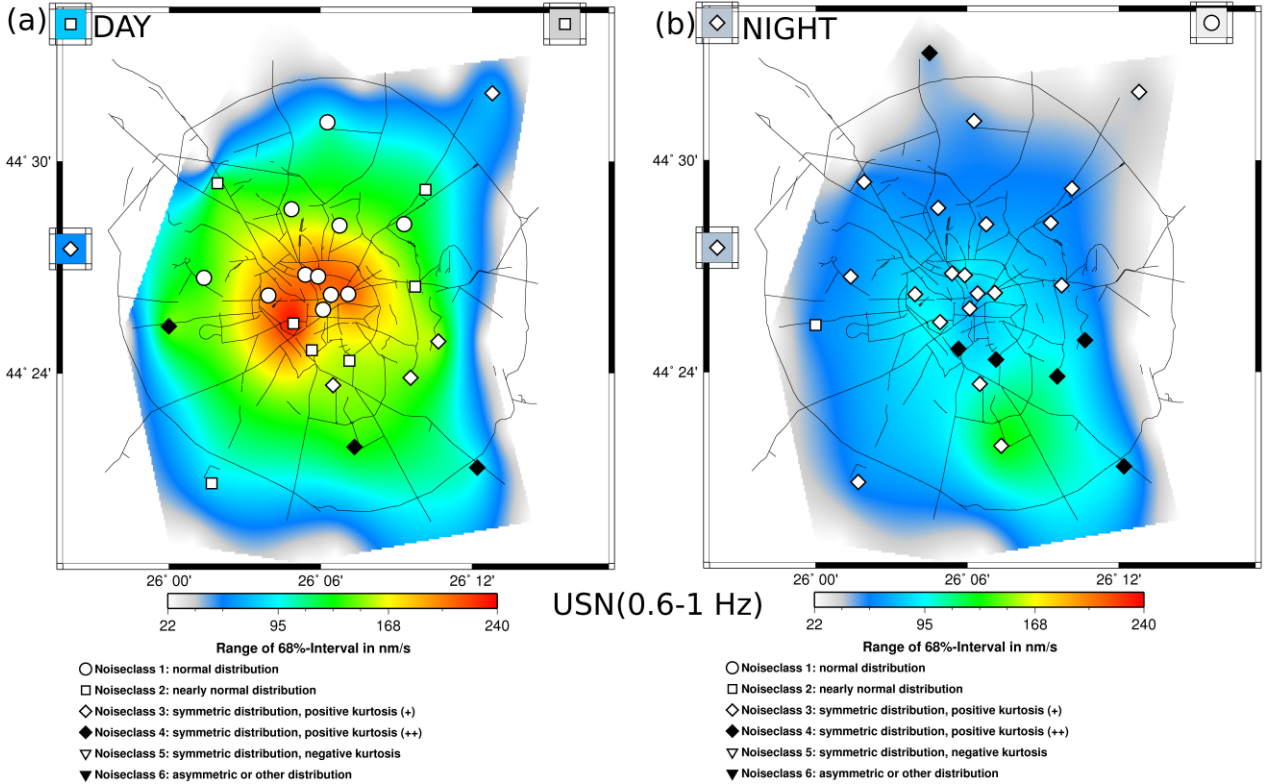


Figure 3: Maps of Bucharest with average urban seismic noise amplitudes and noise classification at station sites (symbols). Displayed are the noise amplitudes (range of the 68%-interval) of the ground motion velocity in nm/s in the frequency range 0.6-1 Hz on 2004-Feb-03. (a) daytime (13-17pm EET). (b) nighttime (00-04am EET). Stations URS06, URS17 and URS19 (outside the city area, see Figure 1) are displayed in separate boxes at the edges. Surface gridding was done by GMT (wwwgmt.soest.hawaii.edu) with the continuous curvature surface gridding algorithm (Smith & Wessel 1990) under a tension of 0.1. This interpolation preserves measured amplitude values at the station sites. The lower limit of the interpolation output is 90 percent of the smallest measured noise amplitude. The upper limit is the largest measured noise amplitude. Between station sites interpolation effects may occur due to partly large inter-station differences in amplitude. Real noise amplitudes cannot be derived between station sites. These maps are mainly visualisation tools to analyse large amounts of output data and search for temporal and spatial variations.

References

- Bonnefoy-Claudet, S., F. Cotton and P-Y. Bard, The nature of noise wavefield and its application for site effects studies – a literature review, *Earth Sc. Rev.*, 79, 205-227, doi:10.1016/j.earscrev.2006.07.004, 2006.
- Campillo, M., Phase and Correlation in Random Seismic Fields and the Reconstruction of the Green Function, *Pure and Applied Geophysics*, 163, 475–502, 2006.
- Curtis, A., P. Gerstoft, H. Sato, R. Snieder and K. Wapenaar, Seismic interferometry – turning noise into signal, *The Leading Edge*, 25, 1082-1092, 2006.
- Mandrescu N., M. Radulian and G. Marmureanu, Site conditions and predominant period on seismic motion in the Bucharest urban area, *Revue Roumaine de Geophysique*, 48, 37-48, 2004.
- Ritter, J. R. R., S. F. Balan, K.-P. Bonjer, T. Diehl, T. Forbriger, G. Marmureanu, F. Wenzel and W. Wirth, Broadband Urban Seismology in the Bucharest Metropolitan Area, *Seismological Research Letters*, 76, 574–580, 2005.
- Sens-Schönenfelder, C. and U. Wegler, Passive image interferometry and seasonal variations of seismic velocities at Merapi volcano, Indonesia, *Geophys. Res. Lett.*, 33, L21302, doi:10.1029/2006GL027797, 2006.
- Shapiro, N. M., M. Campillo, L. Stehly and M. H. Ritzwoller, High-resolution surface-wave tomography from ambient seismic noise, *Science*, 307, 1615-1618, 2005.
- Smith, W. H. F. and P. Wessel, Gridding with continuous curvature splines in tension, *Geophysics*, 55, 293-305, 1990.
- Sudhaus, H. and J. R. R. Ritter, Broadband frequency-dependent amplification of seismic waves across Bucharest, Romania, *Journal of Seismology*, DOI 10.1007/s10950-008-9140-0, 2009.
- Wenzel, F., D. Lungu and O. Novak, *Vrancea earthquakes tectonics, hazard and risk mitigation*, Kluwer Academic Publishers, Dordrecht, Boston, 1999.

Unsupervised Recognition and Interpretation of Patterns in Continuous Seismic Wavefield Records: Application to Small-Scale Array Measurements

Andreas Köhler¹, Matthias Ohrnberger², Frank Scherbaum²

¹ Department of Geosciences, University of Oslo, Norway, E-mail: akoehler@uni-potsdam.de

² Department of Geosciences, University of Potsdam, Germany

Modern acquisition of seismic data on receiver networks worldwide produces an increasing amount of continuous wavefield recordings. Furthermore, over the last two decades, increasing attention has been paid to the estimation of the propagation properties of surface waves from seismic noise, which allows for passive investigations on local and, more recently applied, also on crustal scales. Hence, in addition to manual data inspection, seismogram interpretation requires new processing utilities for pattern recognition and data visualization. When we talk about patterns in seismic recordings, we usually refer to distinct arrivals of wave phases. Within the context of noise analysis, temporal patterns also concern changes in wavefield characteristics on longer time scales (from hours to months). These variations can become important for data processing and, therefore, need to be recognized and investigated. This study applies an unsupervised learning approach for the discovery, imaging and interpretation of temporal patterns in seismic recordings (Köhler et al., 2009). The benefit of unsupervised analysis in seismology lies in its potential to let the data speak for itself with a minimum of domain knowledge as a initial processing step, without being biased by preconceptions of the researcher. For this purpose, the data is parametrized by real-valued feature vectors for short time windows using standard seismic

analysis methods which consider the coherency, polarization and spectral content of the wavefield. We use Self-Organizing Maps (SOMs, Kohonen, 2001) for an intuitive data visualization, i.e. a projection from the high-dimensional feature space into 2D, and clustering procedure, i.e. the automatic grouping of all identified patterns. The goal of this study is to show the practicability of this technique to recognize temporal patterns in a noise wavefield recorded over one day close to the village of Colfiorito (Italy). Furthermore, the effect of these variations on Love wave dispersion curves, estimated using the three-component modified spatial autocorrelation method (3c-MSPAC, Köhler et al., 2007), is investigated. Figure 1 presents the seismograms, the cluster membership of each time window and the averaged Love wave dispersion curves for each hour. The SOM visualization, which is not shown here, is used to assess and to confirm the reliability of the obtained clustering (3 clusters) and to allow the physical interpretation of each cluster. The dark grey cluster (nighttime) is mainly defined by the increased energy contribution at lower frequencies compared to the grey cluster (daytime). Furthermore, high semblance ($f-k$) is observed on radial and tangential components for the dark grey cluster. On the other hand, only the tangential semblance is high for the grey cluster. These observations are expected, since it is known that

man-made noise at daytime mainly generates ground motion above 1 Hz and is dominated by Love waves, whereas Rayleigh-wave-dominated oceanic microseism has a higher contribution below 1 Hz. The right panel of Figure 1 shows that the estimated Love wave dispersion curves become unstable below 1 Hz between 9 p.m. and 1 a.m., i.e. unrealistic high slowness values and increased uncertainties are obtained. During the same time interval, a clear change in the considered wavefield properties can be observed (white cluster). Low semblance and high imaginary SPAC coefficients indicate that the assumption of planar and coherent surface waves is no longer fulfilled. An explanation could be the lack of Love wave energy at night due to less human activity. However, the transition between the white and dark grey clusters at 1 a.m. seems

not to happen continuously, and no disturbed dispersion curves are observed at night between 7 and 9 p.m. or 1 and 2 a.m.. Hence, the discovered phenomenon may additionally be related to a local source inside or close to the array generating non-planar waves. In summary, it is shown that disturbing wavefield patterns may affect dispersion curve estimates, particularly at night when the overall energy of the wavefield is reduced due to the 24-hour cycle. Excluding the corresponding clusters from further processing improves the quality of results. However, no direct effect of the daily variation due to human activity on the phase velocities can be observed. It is planned to use this technique for the analysis of longer records at lower frequencies within the framework of noise cross-correlation.

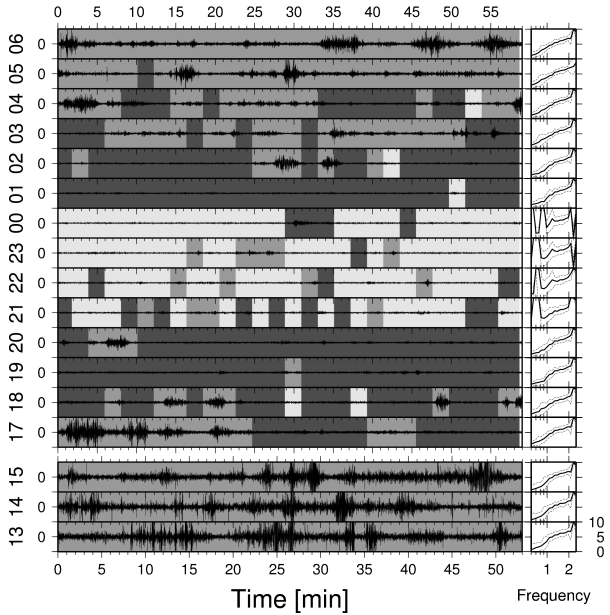


Figure 1. Visualization of patterns in 17 hours of Colfiorito recordings. Y-axis labels indicate hour of day. Background colouring corresponds to SOM clustering using six different wavefield properties (radial and tangential semblance, radial and tangential SPAC coefficients, amplitude spectrum, instantaneous frequency). North component of one array station is shown. The right panel shows the 3c-MSPAC Love wave dispersion curves averaged over each hour. The Y-axis labels are given in slowness (s/km).

References

Köhler, A., M. Ohrnberger, and F. Scherbaum, Unsupervised Feature Selection and General Pattern Discovery Using Self-Organizing Maps for Gaining Insights into the Nature of Seismic Wavefields, Computers and Geosciences, 2009, in press

Köhler, A., M. Ohrnberger, and F. Scherbaum, Assessing the Reliability of the Modified Three-component Spatial Autocorrelation Technique, Geophy. J. Int., v. 168, pp. 779-796, 2007

Ambient vibration analysis for site effect assessment – from measurement to interpretation

Matthias Ohrnberger¹

¹Institut für Geowissenschaften, Universität Potsdam, Germany,
e-mail: mao@geo.uni-potsdam.de

Introduction

The effect of surface geology on seismic motion and its considerable impact on damage distribution during strong ground shaking has already been recognized after the 1923 Kanto Earthquake (Bard, 1998). The modification of seismic ground motion at some locality of interest and its large rapid spatial variability when comparing closely collocated measurement points is the consequence of a number of distinct wave propagation phenomena in the earth and summarized in the term 'site effect'. Observations and modeling results can explain and distinguish between simple amplification of ground motion due to impedance characteristics of shallow soft sediments, reverberations in 1-D layered media leading to frequency selective amplification, site (de-)amplification due to (de-)focusing effects in 2-/3-D subsurface structures (e.g. Stephenson et al., 2000), topographic effects (e.g. hills and ridges, Bouchon and Barker, 1996), significant lengthening of the duration of strong ground motion caused by trapped waves in basin structures (e.g. Cornou et al., 2003), and non-linear behavior of earth materials during very strong shaking.

A direct observation of those effects can be obtained from strong motion earthquake recordings. Typically, spectral analysis including spectral ratio techniques (surface vs. borehole, soil vs. rock) are applied to earthquake recordings to allow for the quantification of site amplification for the strong motion case. However, an obvious disadvantage of these techniques is the need for operating continuously a dense network of strong motion sensors at all sites of interest. An additional problem exists for less seismically active regions. Depending on

the region's seismicity level it may take years to acquire appropriate earthquake data that are suited for the quantitative analysis of site effects. Thus, methods being applicable at any time, like the recording and analysis of ambient vibration wavefields, have become a quasi standard approach for assessing site effects. As the passive observation of microtremor wavefields is a low-cost measurement technique, simple to conduct, and applicable without any environmental concerns (unlike invasive techniques), it is further the natural choice for site effect assessment studies in densely populated urban areas, where alternative (active) geotechnical exploration techniques are difficult to perform. Thus, the number of studies reported from around the globe increased rapidly since the mid of the 1980's (for a review see e.g. Kudo, 1995, Bard, 1998 and Bonnefoy-Claudet et al., 2006a).

However, the interpretation of raw spectra and spectral ratios (H/V) of ambient vibration recordings did not always compare well to historic damage distributions, results obtained from the analysis of strong motion records or the geologic prior information. Therefore, the reliability of techniques exploiting the natural noise wave-field for site effect assessment was questioned and the cause of inconsistent results was much debated (for a review, see Bard, 1998). Discussions centered around measurement conditions and processing details, but also conceptual criticism regarding the interpretation of weak motion data for predicting strong motion and/or the assumptions made about the microtremor wave-field composition (body wave vs. surface wave proportion, P-SV vs. SH wave proportion, stationarity in

space and time, etc.) and site geometry (mainly 1D interpretation). Only in rare cases, an independent quantitative check of the assumptions has been conducted.

The SESAME experience

The rapid spread of microtremor based studies on one hand and the necessity for a better understanding of the nature of the ambient seismic noise wavefield for refined quantitative interpretation of noise recordings finally gave birth to a EU funded research project called SESAME (**S**ite **E**ffect**S** assessment using **A**mbient **E**citations). SESAME tried to thoroughly address open questions regarding the reliability of H/V and ambient vibration array measurement techniques for site effect characterization by putting emphasis on the complete argumentation chain, from measurement via processing to the interpretation of analysis results. Experimental recording conditions and instrumentation issues were tested, documented and guidelines for practical use have been developed (Chatelain et al., 2008, Guillier et al., 2008). The influence of wave-field conditions on analysis results was tested with numerical wave-field simulations (Cornou, 2005) using different algorithms (Hermann, 1996, Hisada, 1994, 1995, Mozco, et al., 2002, Kristek and Mozco, 2003). Many distinct data sets were created by varying the wave-field composition, site geometries (from canonical 1D to realistic 3D basin structures), spatio-temporal distribution of excitation sources (random, sparse, concentrated, etc.) and source-receiver geometries in virtual testbeds. Further, measurements were conducted at a number of sites around Europe to complement synthetic data sets with real data for comparison (diGiulio et al., 2006, Ohrnberger et al., 2004, Roten et al., 2006, Wathelet et al., 2004).

The results of SESAME confirmed the suitability of ambient vibration approaches for site effect characterization in simple environments, i.e. dominantly 1-D soft soil conditions with a strong impedance contrast allows reliable estimation of

fundamental frequencies using H/V techniques. Interestingly, the fundamental peak in the H/V spectral ratio may be explained differently, i.e. either Rayleigh wave fundamental mode ellipticity or fundamental mode Love wave Airy phase or SH body wave resonance can produce the fundamental H/V peak at almost the same frequency, whenever the impedance contrast is high (above 3.5 to 4, see Bonnefoy-Claudet et al., 2006b). The relation of H/V peak frequencies caused by SH-resonance and Rayleigh wave ellipticity as function of the impedance contrast for a single layer over half space situation had been derived previously in a theoretical study by Malischewsky and Scherbaum (2004).

Regarding the estimation of surface wave phase velocity curves using small aperture array recordings the studies in SESAME showed clearly the potential of this approach. Both standard processing techniques, i.e. high resolution f-k (Capon, 1969) and the spatial autocorrelation method SPAC (Aki, 1957) and subsequent modifications like MSPAC (Bettig et al., 2001) can be used to derive dispersion curve branches from ambient vibration wavefields. However, even in very simple structures, the interpretation of the data can be tricky and careful analysis is required to identify potentially problematic wavefield situations. Difficult to recognize is the violation of implicit assumptions underlying some processing algorithm (e.g. dominant noise source direction for SPAC analysis and small number of stations or short recording period). A cross-check between methods relying on distinct assumptions is therefore strongly recommended in order to avoid partial misinterpretation of phase velocity curve estimates (Ohrnberger et al., 2004). Further restrictions apply with respect to the appropriate frequency band in which the surface wave phase velocity interpretation can be considered as reliable: The frequency dependence of the energy partitioning among fundamental and higher modes may be complicated and depends on the structure as well as on the excitation (noise sources).

Additionally, the array recording geometry poses limits on the reliable wavelength range which allows unbiased estimates of horizontal propagation velocities in the wave-field. For soft soil sites with high impedance contrast to the underlying bedrock array settings capable of covering an enormous wavelength range (from few meters to kilometers!) are required. Given these conditions, bedrock velocities (equivalently phase velocities at long periods) are very difficult to obtain from microtremor recordings (Scherbaum et al., 2003). As a consequence, it is mostly impossible to recover the subsurface shear velocity profile down to the bedrock and independent a priori information is needed to constrain bedrock depth and/or bedrock velocity. Combined inversion of H/V and dispersion curve measures (Parolai et al., 2005, Picozzi et al., 2005) seem to be an alternative and may be a first step towards an improvement of this methodological deficiency.

Blind tests and on-going research

The findings within SESAME raised some questions regarding the 'blind' application of microtremor array analysis as standard geotechnical exploration tool. In order to obtain a conclusive result about the reliability of analysis procedures and to raise the awareness of the potential difficulties in phase velocity interpretation, two independent international blind tests were conducted. The USGS invited several groups in the year 2004 to participate in a real-environment blind test including measurements, analysis and inversion. The final comparison of results were done on the shear wave velocity/slowness profiles (Asten and Boore, 2005). The test-site was selected in order to allow for comparison of invasive and non-invasive methods (Boore and Asten, 2008), and both active and passive geophysical exploration techniques were used to derive the shear velocity profiles. In conclusion, the authors found significant variability in the derived shear wave models, however, the site amplification estimated from the provided

blind test results differed by no more than 20%. The interesting question why the variability of shear wave models was such high, could not be finally answered. Each step in the processing chain (measurement, data analysis, data interpretation, inversion strategy and computational implementation) were performed individually by each participating group and thus the obtained differences can not be attached to one particular analysis step.

The 2nd international blind test was conducted in the realm of the 2006 meeting of the IAEE/IASPEI working group on effects of surface geology on seismic motion (ESG). Both synthetic data sets and real data sets from selected reference sites were prepared and provided to contestants. Details about velocity structures, modeling approaches and analysis of this blind test are described in Cornou et al., (2007). A first comparison was then realized for the principle analysis results returned by the participants, i.e. the dispersion curve estimate derived from the synthetic data sets. Similar to the findings in SESAME, a positive conclusion could be given: independent of the applied analysis method, the phase velocity (slowness) estimates were within 10% to 20% from the true values when only the 'reliable' frequency band (i.e. fits the wavelength range of the chosen array geometry) was considered. One interesting and maybe surprising result was the fact, that most participating groups were optimistic regarding the bandwidth of reliability for their observations. At high frequencies the wavelength limitations of the array geometry are rather obvious (aliasing) and there seems to be no major risk for misinterpretation. However, at low frequencies, analysis results look often reasonable and even more easy to be interpreted as scatter seems to decrease. Still the analysis may be biased towards high velocities due to insufficient resolution capabilities of the chosen array geometry. Although SPAC based methods were less affected in this aspect, conservative values for the wavelength

limits should be used for the interpretation. Depending on the complexity of the site, the apparently largest difficulty of this blind test experiment was the correct association of partially observable mode branches. Most participants failed in correctly identifying the fundamental mode dispersion curve mostly due to similar reasons as were found during the SESAME project: there exist a number of simple, but not unrealistic nor uncommon subsurface situations, which can show complicated Rayleigh wave dispersion curve behaviour due to the existence of osculation points. When estimating dispersion curves from these model data, the derived phase velocity curves are well estimated, look apparently simple and can be continuously followed within a broad frequency band. Unfortunately, the simple looks of the estimated dispersion curves is a result of 'mode jumping' in the vicinity of the osculation points. Due to the rapid change of energy partitioning between individual surface wave modes, there is no possibility to obtain the full dispersion branch picture. Again, in these cases, there is only one solution from a practical viewpoint: a cross-check has to be performed with independent data. Useful are the analysis of horizontal component recordings for deriving complementary Love wave dispersion curves as well as using the H/V ratio in combination with the dispersion curve estimates in order to resolve conflicts with the mode interpretation. The final shear wave velocity estimates showed also in this blind test exercise a considerable amount of variability. However, no final conclusion about the cause of the variability could be drawn due to the incorrect association of mode branches by most participants (Cornou et al., 2007). The experience in SESAME indicated a strong variability in the final shear wave velocity profiles simply due to the non-linearity and non-uniqueness of the inversion problem itself (Wathelet et al., 2004, Wathelet et al., 2008 and Wathelet 2008). An independent blind test on dispersion curve inversion might provide an answer about the reliability of final results and thus seems a necessary and important contribution for

improving shear wave velocity profiling from surface wave methods (both active and passive) in future.

Although soft soil sites are of main interest for site effect studies (highest expected amplifications, highest population density and urban agglomeration), there is also considerable interest of employing ambient vibration site characterization techniques to other (and also more complicated) sites. Within NERIES, a FP6 EU infrastructure project, passive microtremor techniques have been applied to 20+ strong motion sites together with other passive and active geophysical exploration techniques (see also <http://www.neries-eu.org>, NERIES Newsletter No. 5). The final aim of this study is to provide a best-practice guideline for site characterization of strong motion recording sites. The EC8 site class of the selected sites were derived from independent measures varies from A to E (rock to soft soil) and site structures comprise different complexity (1D to 3D). Passive measurements were accompanied by active MASW and refraction studies in order to identify the influence of non-1D structures on the final results. Using a newly developed real-time wireless array recording system, allowing for in-field quality control and real-time analysis of dispersion curves, an iterative deployment strategy has been developed in order to enable highly reliable phase velocity estimates for very broad wave length ranges. Starting at very small apertures, the shortest wave length range of interest can be analysed and a first partial dispersion curve branch can be estimated. This estimate is used to derive the recording geometry (array dimension) needed for the next target wavelength range. This procedure is repeated until a satisfying broadband dispersion curve is obtained. This controlled measurement strategy has been proven to be advantageous with respect to 'blind' recording, as unfavorable wavefield situations or array geometry limitations can be immediately dealt with. As a preliminary result, it can be concluded, that site characterization at strong motion

sites (usually with stiff soil or rock conditions) is feasible as long as no strong 2D or 3D effect (topography or subsurface structure) is encountered in the wave-field.

Concluding remarks

Ambient vibration measurements are well suited for site effect estimation by determination of shallow subsurface shear wave velocity profiles using array techniques and further by evaluating the fundamental resonance frequency using single station H/V ratios as proxy measure. Care has to be taken to not exceed the limitations of methods and to cross-check with independent data from geological or geophysical measurements. In case of 2D or 3D structures with dimensions close to the observed wavelengths, standard procedures will almost certainly fail, and newly developed techniques are needed for improved interpretation of those structures. Noise correlation techniques might be useful for these situations in future, although significant longer recording times will be required for obtaining reliable answers.

Acknowledgements: SESAME and NERIES group members, in particular M. Wathelet, C. Cornou, D. Vollmer, F. Scherbaum, B. Endrun, A. Savvaidis, A. Köhler, S. Bonnefoy-Claudet, F. Renalier, N. Theodoulidis and P.-Y. Bard.

Asten, M. W., and D. M. Boore (Editors) (2005). Blind Comparisons of Shear-Wave Velocities at Closely-Spaced Sites in San Jose, California, U.S. Geol. Surv. Open-File Rept. 2005-1169.

Bard, P.-Y. (1998). Microtremor measurements: a tool for site effect estimation?, in 2nd Int. Symp. on the Effects of Surface Geology on Seismic Motion, Yokohama, Japan, 3, 1251–1279.

Bettig, B., Bard, P.-Y., Scherbaum, F., Riepl, J., and Cotton, F., 2003. Analysis of dense array noise measurements using the modified spatial auto-correlation method (SPAC). Application to the Grenoble area, Bollettino di Geofisica Teorica ed Applicata, 42-3/4, 281-304.

Bonnefoy-Claudet, S., Cotton, F., and Bard, P.-Y. (2006a). The nature of noise wavefield

and its applications for site effects studies: A literature review, Earth-Science Reviews Volume 79, Issues 3-4, Pages 205-227.

Bonnefoy-Claudet, S., C. Cornou, P.-Y. Bard, F. Cotton, P. Moczo, J. Kristek, and D. Fäh (2006b). H/V ratio: a tool for site effects evaluation: results from 1D noise simulations, Geophys. J. 167, no. 2, 827–837.

Bonnefoy-Claudet, S., Köhler, A., Cornou, C., Wathelet, M., and Bard, P.-Y., Effects of Love Waves on Microtremor H/V Ratio, BSSA, Feb 2008; 98: 288 - 300.

Boore, D. M. (2006). Determining subsurface shear-wave velocities: a review, in Third International Symposium on the Effects of Surface Geology on Seismic Motion, P.-Y. Bard, E. Chaljub, C. Cornou, F. Cotton and P. Gueguen (Editors), Grenoble, France, 30 August–1 September 2006, Laboratoire Central des Ponts et Chaussées, 67–85

Boore, D.M., and Asten, M.W., Comparisons of Shear-Wave Slowness in the Santa Clara Valley, California, Using Blind Interpretations of Data from Invasive and Noninvasive Methods, BSSA, 98: 1983 - 2003.

Bouchon, M., and Barker, J.S. (1996). Seismic response of a hill: The example of Tarzana, California, BSSA, 86: 66 - 72.

Chatelain, J.-L., B. Guillier, F. Cara, A.-M. Duval, K. Atakan, P.-Y. Bard and the WP02 SESAME team (2007). Evaluation of the influence of experimental conditions on H/V results from ambient noise recordings, Bull. Earthq. Engng., doi: 10.1007/s10518-007-9040-7.

Cornou, C. (2005). Reports D11.10 and D17.10, Set of noise synthetics for H/V and array studies from simulation of real sites and comparison for test sites in European Commission: Research General Directorate, Project No. EVG1-CT-2000-00026, SESAME, 62 pp.: available online at <http://sesame-fp5.obs.ujf-grenoble.fr> (last accessed June 2009).

Cornou, C., Bard, P.-Y., and Dietrich, M. (2003). Contribution of Dense Array Analysis to the Identification and Quantification of Basin-Edge-Induced Waves, Part I: Methodology, BSSA, Dec 2003; 93: 2604 - 2623.

Cornou, C., Bard, P.-Y., and Dietrich, M. (2003). Contribution of Dense Array Analysis to the Identification and Quantification of Basin-Edge-Induced Waves, Part II:

Application to Grenoble Basin (French Alps), BSSA, Dec 2003; 93: 2624 - 2648.

Cornou, C., M. Ohrnberger, D. M. Boore, K. Kudo, and P.-Y. Bard (2007). Derivation of structural models from ambient vibration array recordings: results from an international blind test, in Third International Symposium on the Effects of Surface Geology on Seismic Motion, P.-Y. Bard, E. Chaljub, C. Cornou, F. Cotton and P. Gueguen (Editors), Grenoble, France, 30 August–1 September 2006, Laboratoire Central des Ponts et Chaussées.

Di Giulio, G., Cornou, C., Ohrnberger, M., Wathélet, M. and Rovelli, A. (2006). Deriving Wavefield Characteristics and Shear-Velocity Profiles from Two-Dimensional Small-Aperture Arrays Analysis of Ambient Vibrations in a Small-Size Alluvial Basin, Colfiorito, Italy, BSSA, 96: 1915 – 1933.

Guillier, B., K. Atakan, J.-L. Chatelain, J. Havskov, M. Ohrnberger, F. Cara, A.-M. Duval, S. Zacharopoulos, P. Teves-Costa and the SESAME team (2007). Influence of instruments on H/V spectral ratios of ambient vibrations, Bull. Earthq. Engng., doi: 10.1007/s10518-007-9039-7.

Hermann R.B. "Computer programs in seismology, Version 3.0", 1996.

Hisada, Y. (1994). An efficient method for computing Green's functions for a layered half-space with sources and receivers at close depths, Bull. Seismol. Soc. Am. 84, no. 5, 1456–1472.

Hisada, Y. (1995). An efficient method for computing Green's functions for a layered half-space with sources and receivers at close depths (part 2), Bull. Seismol. Soc. Am. 85, no. 4, 1080–1093.

Köhler, A., M. Ohrnberger, F. Scherbaum, M. Wathélet, and C. Cornou (2007). Assessing the reliability of the modified three-component spatial autocorrelation technique, Geophys. J. Int. 168, no. 2, 779–796.

Kudo, K. (1995). Practical estimates of site response: state-of-art report, in 5th Int. Conf. on Seismic Zonation, Nice, France.

Kristek, J. and Moczo, P. (2003). Seismic-Wave Propagation in Viscoelastic Media with Material Discontinuities: A 3D Fourth-Order Staggered-Grid Finite-Difference Modeling, BSSA, 93: 2273 - 2280.

Malischewsky, P. G. , and F. Scherbaum (2004). Love's formula and H/V-ratio

(ellipticity) of Rayleigh waves, Wave motion, 40, 57-67.

Moczo P., Kristek J., Vavrycuk V., Archuleta R. and Halada L. 2002. 3D heterogeneous staggered-grid finite-difference modeling of seismic motion with volume harmonic and arithmetic averaging of elastic moduli and densities. BSSA, 92, 3042-3066.

Ohrnberger, M., E. Schissele, C. Cornou, M. Wathélet, A. Savvaidis, F. Scherbaum, D. Jongmans, and F. Kind (2004). Microtremor array measurements for site effect investigations: comparison of analysis methods for field data crosschecked by simulated wave fields, in 13th World Conf. on Earthquake Engineering, Vancouver, Canada, paper 940.

Parolai, S., M. Picozzi, S. M. Richwalski, and C. Milkereit (2005), Joint inversion of phase velocity dispersion and H/V ratio curves from seismic noise recordings using a genetic algorithm, considering higher modes, *Geophys. Res. Lett.*, 32, L01303, doi:10.1029/2004GL021115.

Picozzi, M., S. Parolai, and S. M. Richwalski (2005), Joint inversion of H/V ratios and dispersion curves from seismic noise: Estimating the S-wave velocity of bedrock, *Geophys. Res. Lett.*, 32, L11308, doi:10.1029/2005GL022878.

Roten, D., D. Fäh, C. Cornou, and D. Giardini (2006). Two-dimensional resonances in Alpine valleys identified from ambient vibration wave fields, *Geophys. J. Int.* 165, no. 3, 889–905.

Scherbaum, F., K. G. Hinzen, and M. Ohrnberger (2003). Determination of shallow shear wave velocity profiles in the Cologne Germany area using ambient vibrations, *Geophysical Journal International*, 152, 597-612.

Stephenson, W.J., Williams, R.A., Odum, J.K., and Worley, D.M. (2000). High-Resolution Seismic Reflection Surveys and Modeling Across an Area of High Damage from the 1994 Northridge Earthquake, Sherman Oaks, California, BSSA, 90: 643 – 654.

Wathélet, M. (2008). An improved neighborhood algorithm: parameter conditions and dynamic scaling. *Geophys. Res. Lett.*, 35, L09301, doi:10.1029/2008GL033256.

Wathélet, M., D. Jongmans, and M. Ohrnberger (2004). Surface wave inversion using a direct search algorithm and its application to ambient vibration

measurements, Near Surface Geophysics, 2, 211—221.

Wathelet, M., D. Jongmans, M. Ohrnberger, and S. Bonnefoy-Claudet (2008). Array performances for ambient vibrations on a shallow structure and consequences over V_s inversion. Journal of Seismology, 12, 1-19.

Array observations of a significant Love wave contribution to the ambient vibration H/V ratio

Brigitte Endrun¹, Matthias Ohrnberger¹

¹ Institute of Geosciences, University Potsdam, 14476 Potsdam, Germany, E-mail: brigitte.endrun@geo.uni-potsdam.de

Measurements of the horizontal-to-vertical spectral ratio (H/V) of ambient vibrations (Nakamura 1989) are widely used as a cheap, fast and non-invasive method for site characterization. If the H/V curve shows a well-defined amplitude peak, it is well established that the frequency at which this peak occurs relates to the fundamental resonance frequency at the site. Accordingly, H/V measurements are used to map variations in resonance frequency over larger areas (e.g. in earthquake-prone cities), to infer the thickness of the sedimentary overburden or its average velocity by rule-of-thumb calculations, to estimate the amplification factor of ground motion or to infer S-velocity-depth profiles by inversion, either alone or jointly with other types of data.

If the ambient vibration wavefield is dominantly composed of surface waves, the H/V amplitude peak can be explained by the frequency-dependent ellipticity of Rayleigh waves, which show horizontal polarization at the peak. However, synthetic tests (e.g. Bonnefoy-Claudet et al. 2008) as well as some autocorrelation measurements with arrays (see Bonnefoy-Claudet et al. 2006) indicate that, depending on sources and site structure, other contributions to the wavefield, specifically Love waves, can also be important. A large Love wave contribution may change the amplitude of the H/V peak significantly, which has to be considered in all applications that make use of amplitude information, i.e. inversion or estimation of the amplification factor. Nevertheless, the contribution of Love waves is often not considered at all in practise or ad hoc fixed at some value, e.g. 50%.

Within the EC-funded NERIES project (JRA4), ambient vibration array measurements were conducted at 20 European sites. For further analysis, we select six sites

where clear and consistent H/V peaks were observed, most of them located in Greece. We investigate the composition of the noise wavefield around the H/V peak by comparing, within narrow frequency windows, the main source directions as derived from FK-analysis to the polarisation direction observed with the array. For all sites, urban as well as rural and shallow (<20m) to deep (~200m) ones, a large part of the wavefield shows a polarisation shifted by 90° compared to the propagation directions. This is a clear indication for the contribution of Love waves (Airy phase) to the H/V peak. Interestingly, this observation not only holds for sites with a strong velocity contrast between sediments and basement, i.e. a large-amplitude H/V peak, where a possible strong contribution of the Love wave Airy phase has been considered before based on synthetic examples (Bonnefoy-Claudet et al. 2008), but also for sites with a broader and weaker H/V peak. A quantitative estimate of the Rayleigh wave contribution is obtained by cross-correlating the distribution of propagation and polarisation directions. It indicates that for all sites, the amount of Rayleigh waves in the wavefield around the H/V peak is less than 50% and lies between 15% and 40%.

The results of our analysis are compared to independent estimates of the relative Rayleigh-wave contribution to the wavefield around the H/V peak from three-component modified spatial autocorrelation functions determined from the array data. Both methods lead to consistent results. Investigation of the complete frequency range of the array recordings also shows that the Rayleigh wave contribution to the wavefield varies strongly with frequency, especially between 1 and 15 Hz, where values between 10% and 60% are observed. At lower and higher frequencies, the contribution seems more stable and lies

around 50%. This might however be due to limited resolution in the array analysis of the data in these frequency ranges.

Our analysis shows that the contribution of Love waves should definitely not be neglected when interpreting amplitude information from the H/V curves. While some single-station methods to extract solely the Rayleigh wave part of the H/V curves are under development (e.g. raydec, Hobiger et al. LGIT; wavelet analysis, Fäh et al. NERIES JRA4 B2), array data, if available, provide an alternative - not only in the form of dispersion curves that can be used to further constrain the subsurface structure, but also in the form of information on the noise wavefield that can be utilized to correct the H/V curves.

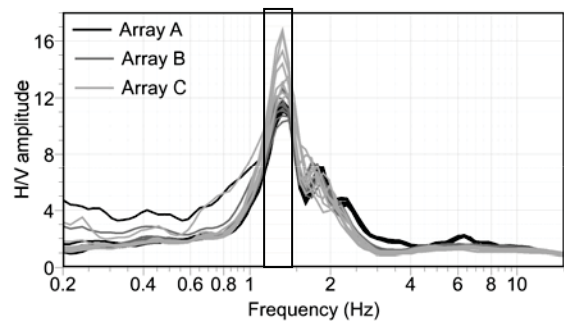


Figure 1. H/V curves measured with three concentric eight-station arrays at Nestos, north-eastern Greece. Note the clear and consistent amplitude peaks at 1.3 Hz. Black box outlines the frequency range that was analysed in Figure 2

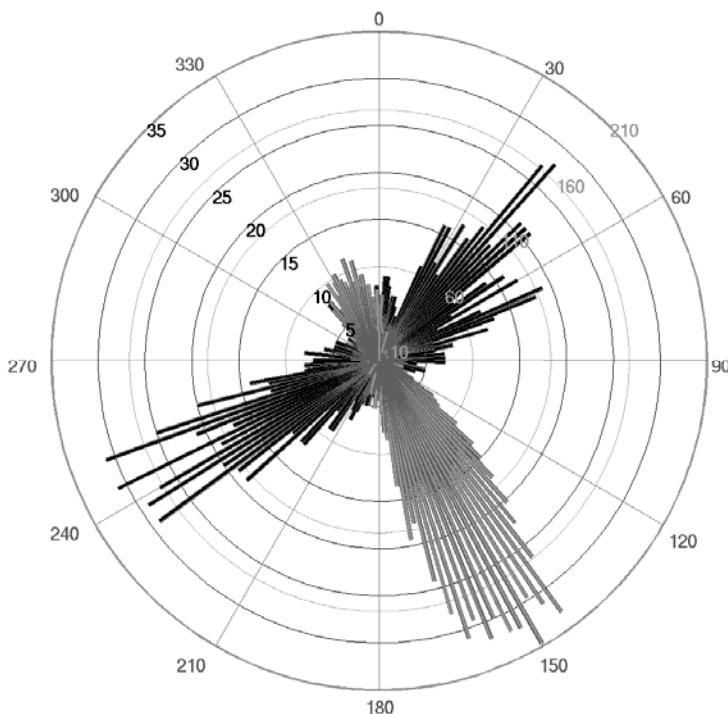


Figure 2. Propagation directions (black) vs. polarisation directions (grey) derived from recordings of Nestos array C (~170 m radius) within the frequency band around 1.3 Hz (H/V curve amplitude peak). The polarisation directions (150°/330°) show a clear phase shift of 90° from the main propagation directions (60°/240°), indicating the strong presence of Love waves (80% of the wavefield from quantitative analysis).

References

Bonnefoy-Claudet, S., A. Köhler, C. Cornou, M. Wathelet and P.-Y. Bard, Effects of Love waves on microtremor H/V ratio, Bull. Seism. Soc. Am, v. 98, pp. 288-300, doi:10.1785/0120070063, 2008.

Bonnefoy-Claudet, S., F. Cotton and P.-Y. Bard, The nature of noise wavefield and its

applications for site effect studies. A literature review, Earth-Sci. Rev., v. 79, pp. 205-227, doi:10.1016/j.earscirev.2006.07.004, 2006.

Nakamura, Y., A method for dynamic characteristics estimation of subsurface using microtremor on the ground surface, Q.R. Rail. Tech., v. 30, pp. 25-30, 1989.

Building Responses Extracted from Seismic Background Signals

Lisa Rehor¹, Thomas Forbriger^{1, 2}

¹ Geophysical Institute, Universität Karlsruhe (TH), Germany, E-mail: lisa.rehor@gpi.uni-karlsruhe.de, thomas.forbriger@gpi.uni-karlsruhe.de

² Black Forest Observatory (BFO), Research Facility of the Universität Karlsruhe (TH) and Universität Stuttgart, Germany, E-mail: thomas.forbriger@gpi.uni-karlsruhe.de

We calculated building responses with the continuously recorded seismic background signals inside a building (Rehor, 2008). For this purpose we modified a method created by Snieder and Şafak (2006) based on the concept of seismic interferometry. The building is described by a linear filter. The recorded wavefield in the basement represents the input signal and the recorded wavefield at the top floor is used as the output signal. By deconvolving the output signal with the input signal we obtain a frequency response function and an impulse response function respectively both describing the mechanical properties of the building. Snieder and Şafak (2006) originally developed their method for the calculation of the building response from earthquake signals. To investigate whether this method is also suited to calculate the building response with background signals we used data from a multi-storey building in Bucharest.

The data was recorded during the Urban Seismology (URS) Project (Ritter et al., 2005) within the CRC 461 “Strong Earthquakes”. As a part of this project the physics tower in Bucharest-Măgurele was instrumented with two stations of the Karlsruhe Broadband Array (KABBA) during a time interval of three months. Station URS34 was located in the basement and station URS35 was located at the top floor. Both stations continuously recorded three-component seismograms.

To extract the frequency response function we used time series of 24 hours length and segmented them into 120 s long time windows. In each time window a complex frequency response function

$$D(\omega) = \frac{\tilde{u}_{\text{URS35}} \tilde{u}_{\text{URS34}}^*}{|\tilde{u}_{\text{URS34}}|^2 + \varepsilon}$$

was calculated, where \tilde{u}_i represents the Fourier transform of the input and output signal respectively and the asterisk denotes complex conjugation. The parameter ε is used for stabilisation and was set to 10% of the average spectral energy density of the input signal (here station URS34). By stacking the complex frequency response functions from all short time windows we obtained one representative frequency response function showing a clear maximum at the resonance frequency of the building (Figure 1). For the physics tower in Bucharest we determined a resonance frequency of 1.66 Hz. This was confirmed by analysing earthquake signals. The advantage of stacking the complex frequency response functions in contrast to stacking their amplitude spectra only is that incoherent signals cancel partly or even totally. Therefore the maximum in the amplitude spectrum obtained by complex stacking of the frequency response functions is smaller than the maximum in the median of all amplitude response functions in different time windows (Figure 1).

To which kind of resonant deformation the observed eigenfrequency should be attributed is still under debate. Observations from two seismometers only do not allow to discriminate between different eigenmodes of the building. Snieder and Şafak (2006) used the model of a pure shear beam only. However, the deformation of the building due to horizontal excitation at its base can also be the bending like that of a cantilever beam.

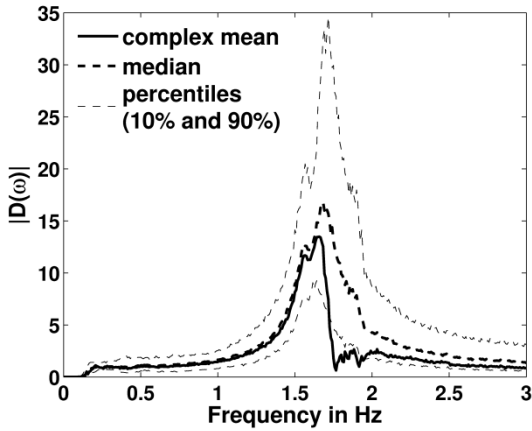


Figure 1: Amplitude spectrum of the frequency response function calculated with the background signal of Saturday July 17th 2004. The thick line shows the result obtained by stacking the complex frequency response functions of the different time windows. The median of all amplitude response functions is displayed by the thick dashed line together with the 10% and the 90% percentiles (thin dashed lines).

Torsional modes may contribute to the observed signals too. Recently Todorovska (2009) suggested to include rocking of the foundation due to soil-structure interaction also into the model. Since the majority of observations can be explained by shear deformation of the building we expect this mode to dominate the resonant vibrations.

The original method proposed by Snieder and Şafak (2006) uses earthquake signals to extract the building response. Therefore we compared the results derived from background signals and earthquake signals. The used earthquakes took place at the Vrancea area at 100 km to 150 km depth and approximately 150 km epicentral distance to the physics tower. The amplitude spectra of the frequency response functions both show a clear maximum at the building's resonance frequency (Figure 2). Their amplitude at this frequency however is quite different. Up to now we can't explain this observation. By calculating the inverse Fourier transformation we extract also the impulse response functions $G(t)$ (Figure 3). The impulse response function revealed from earthquake signals is causal because the building is excited dominantly at its basement. At

positive times one can see the damped resonant oscillation of the building. This observation can be explained by one-dimensional shear waves reverberating inside the building (Snieder and Şafak, 2006). In contrast, the impulse response function calculated with background signals seems to be symmetric to the time origin. This difference is possibly due to the different signal character. In contrast to earthquake signals the continuously recorded background signal is a superposition of waves excited of course also at the building's basement but additionally at its roof and its walls (e.g. by wind) or inside the building (e.g. by an elevator). Due to variations of the location of dominating sources, full phase coherence cannot be expected over 24 hours. The impulse response may even become acausal when referring the signals to an apparent source at the base of the building.

Liss (2008) calculated the building response from continuously recorded seismic background signals to investigate a multi-storey building in Istanbul. In contrast to our results she obtained a more complex frequency response function possibly suggesting a more complex structural design of the building in Istanbul than of the building in Bucharest. The impulse response function of the building in Istanbul is also acausal but

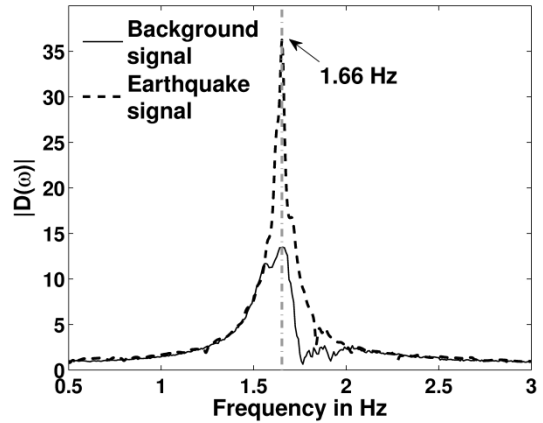
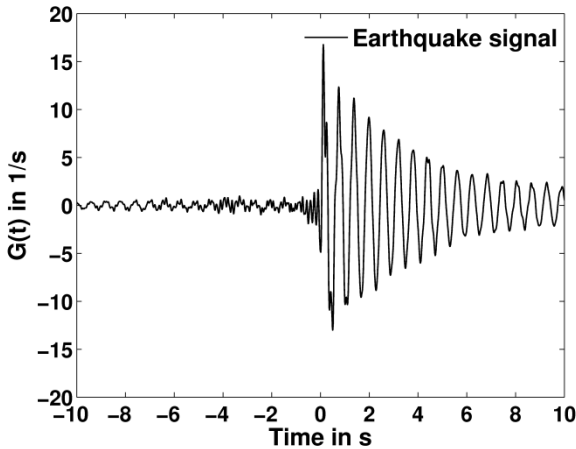


Figure 2: Amplitude spectra of the frequency response functions calculated with the background signal of July 17th 2004 and with the earthquake signal of July 10th 2004. The building's resonance frequency determined from these results is marked by the grey dash-dotted line.

(a)



(b)

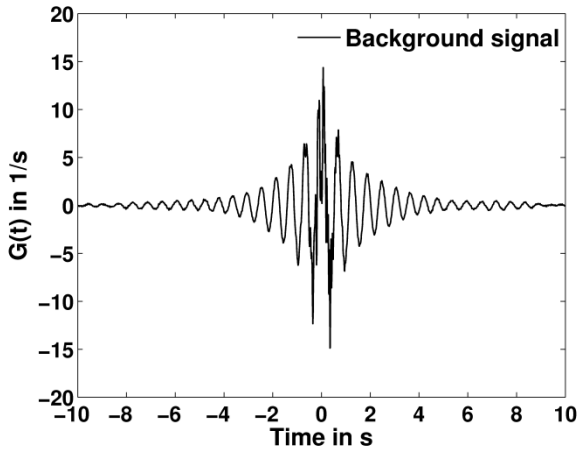


Figure 3: Impulse response functions calculated with (a) the earthquake signal of July 10th 2004 and with (b) the background signal of July 17th 2004.

it contains no clear structure like the damped resonant oscillation in the case of the building in Bucharest. On the other hand, some of her seismic background data revealed a single travelling pulse, when referring the signals in the basement to those from the upper station. This was not the case for the URS data in the present study.

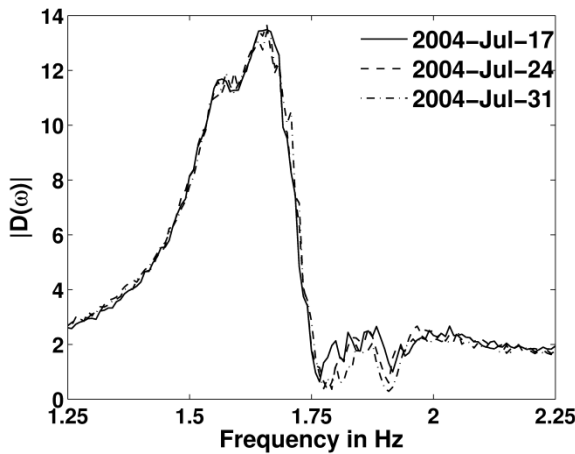
To investigate the robustness of the results in the case of using background signals we calculated frequency response functions with the background signal of different days (always 24 h time series). In doing so we recognised a difference in the obtained frequency response functions depending on whether the background signal of a day at the weekend or of a working day is used (Figure 4). In the frequency response functions extracted from background signal of working days a second maximum at approximately 1.9 Hz appears beside the maximum at the resonance frequency (1.66 Hz). Because the maximum at 1.9 Hz occurs only in the frequency response functions calculated with the background signal of working days it is possibly caused by a source which is located near the station at the top floor and which is only active during working days. Because the physics tower in Bucharest is an office building there is less man-made signal excited inside the building during weekends. Therefore

imaginable sources are e.g. an air conditioner or the engine of an elevator.

We conclude that the resonance frequency of the physics tower could be determined very precisely from the frequency response functions extracted from seismic background signals. Furthermore, the amplitude spectra of the frequency response functions are relatively similar in the case of earthquake signals and background signals. In contrast, the corresponding impulse response functions differ from each other. One of them is causal, the other not. These differences are possibly caused by the different excitation of the building. In the case of earthquake signals the building is excited dominantly at its basement whereas in the case of background signal sources at different locations inside the building have to be considered.

Currently we investigate whether the component of seismic background signal with a causal phase relation to the station on the basement can be extracted by appropriate analysis. If possible, large existing datasets of earthquake recordings from seismic stations in cities could be used to estimate realistic motion of the top of a building after previously recorded earthquakes by applying an impulse response function of the building obtained from a short observation of seismic background signal with two instruments. This could serve as a tool for seismic hazard assessment.

(a)



(b)

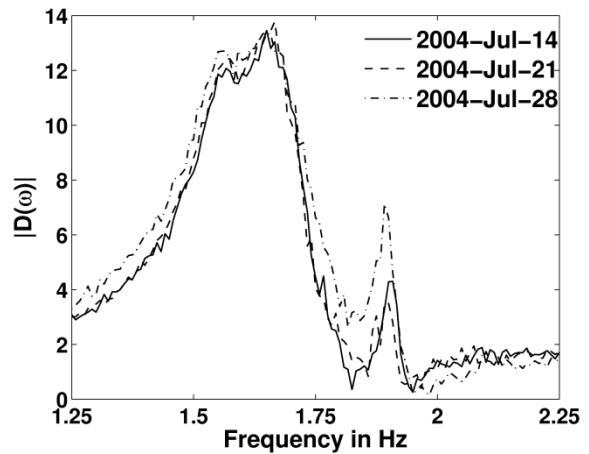


Figure 4: Amplitude spectra of the frequency response functions calculated with the background signal of (a) three different Saturdays (days at the weekend) and (b) three different Wednesdays (working days).

References

Liss, B., Frequency and time analysis of seismic noise: Application for estimating the response of buildings. Studienarbeit, Angewandte Geowissenschaften, Technische Universität Berlin, 2008.

Rehor, L., Bestimmung von Antwortfunktionen mit seismischer Interferometrie. Diplomarbeit, Geophysikalisches Institut, Universität Karlsruhe (TH), 2008.

Ritter, J., S. Balan, K.P. Bonjer, T. Diehl, T. Forbriger, G. Mărmureanu, F. Wenzel and W. Wirth, Broadband urban seismology in the Bucharest metropolitan area. Seism. Res. Lett., 76(5), pp. 574-580, 2005.

Snieder, R. and E. Şafak, Extracting the building response using seismic interferometry: Theory and application to the Millikan Library in Pasadena, California. Bull. Seism. Soc. Am., 96(2), pp. 586-598, 2006.

Todorovska, M. I., Seismic interferometry of a soil-structure interaction model with coupled horizontal and rocking response. Bull. Seism. Soc. Am., 99(2A), pp. 611-625, 2009.

Radiative transfer of seismic waves: theoretical approach and applications

Ludovic Margerin

Centre Européen de Recherche et d'Enseignement de Géosciences de l'Environnement, Université Aix-Marseille-C.N.R.S., Europôle Méditerranéen de l'Arbois, BP 80, 13545 Aix en Provence, France

The field of multiple scattering of seismic waves is in rapid development with many new applications to tomographic imaging and monitoring of temporal variations. In this review, I will show that the modern theory of radiative transfer based on approximations of the exact Dyson and Bethe-Salpeter equations offers a unifying approach to understand many key concepts in the multiple scattering of seismic waves such as diffusion, equipartition, coherent backscattering and Green function reconstruction from coda waves. The focus will be primarily on the theoretical approach but applications based on field and laboratory experiments will also be presented.

Radiative Transfer of Elastic Waves in Random Media with Multiple Scales

Jens Przybilla¹, Michael Korn¹, Ulrich Wegler²

¹ Institute for Geophysics and Geology, University of Leipzig, Germany,

² Federal Institute for Geosciences and Natural Resources (BGR)

E-mail: jprzybilla@uni-leipzig.de, mikorn@uni-leipzig.de, wegler@sdac.hannover.bgr.de

Radiation transport theory (RTT) describes the propagation of wave energy in scattering media that means especially in media with small scale heterogeneities. For this we look at squared seismogram envelopes which are proportional to wave energy. RTT is one of the most powerful tools to analyse the multiple scattering regime of waves and to obtain informations about small scale heterogeneities. Basic validity assumptions of RTT are: fluctuations of wave velocities are weak, waves are scattered incoherently and correlation length is of the same order of magnitude as the wavelength. We solve the elastic radiative transfer equations numerical with Monte Carlo methods (Przybilla and Korn, GJI, 2008). In Monte Carlo simulations only wave energy is simulated not the waves themselves. The probabilities for scattering are estimated with Born scattering coefficients.

One of the simplest models for small scale heterogeneities is a medium with random fluctuations around a constant background velocity, that is characterized by an autocorrelation function (ACF), a characteristic scale called the correlation length a and fluctuation strength of the wave velocities ϵ . However, results from borehole velocity logs show, that there is a need for more than one scale to correctly characterise small scale heterogeneities of the earth medium (e.g. Goff und Holliger, JGR, 1999).

Here we present Monte Carlo simulations of RTT in random media with more than one scale. To obtain such a random medium we superpose two and three Gaussian ACFs, with different correlation lengths and for simplicity with the same fluctuation strength. The numerical simulations show, how wave energy can propagate through such a random medium with multiple scales. We compare our results with Monte Carlo simulations in a single scale

random medium. This comparison shows, that in a multiscale random medium coda is mainly influenced by that scale, that is in the range of $a k=1$ (fig.1). Figure 1 shows envelopes which are calculated by Monte Carlo simulations. This envelopes represent the energy density of waves and are proportional to squared seismogram envelopes.

If multiple scattering occurs, the characteristic of wave energy is diffusive. We compared our Monte Carlo simulations in multiple scale random media with solutions of the diffusion equation (fig. 2). The agreement between Monte Carlo simulations and the solutions of the diffusion equation for late times is very good.

Continuous random media with one correlation length and fluctuation strength are some of the simplest models for small scale heterogeneities of the earth and it is possible to obtain good inversion results if we compare our Monte Carlo simulations in a single scale random medium with data (e.g. Przybilla et. al., 2009). But in general these models are too simple for real earth heterogeneities as shown in borehole analysis (e.g. Goff und Holliger, JGR 1999). If the medium contains more than one typical scale, waves interact most intensively with scales that are of the order of the wavelengths. Here we used a Gaussian medium with one and a Gaussian medium with more than one scale only. Superpositions of different random media for instance von Karman media are also possible and probably necessary to find a good agreement between data and simulations, but we think that this superposition is only an approximate step to describe the complicated structure in the small scale range of the earth medium.

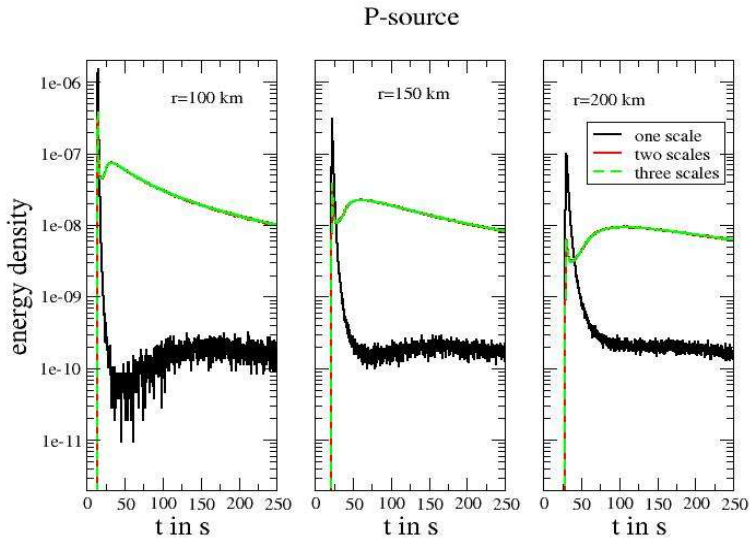


Figure 1.

Monte Carlo simulations of one- (black curves), two- (red curves) and three-scale Gaussian random media (green curves) for three radial distances r . The source is a P wave source without generation of S waves. In the one scale medium $a_1 k_s = 16$, in the two scale medium $a_1 k_s = 16$ and $a_2 k_s = 1,6$, and in the three scale medium $a_1 k_s = 16$, $a_2 k_s = 1,6$ and $a_3 k_s = 0,16$. In all random media fluctuation strength is $\varepsilon = 3\%$. The difference between the single and the two scale medium is big. The third scale has no important influence on the envelopes compared with the two scaled medium.

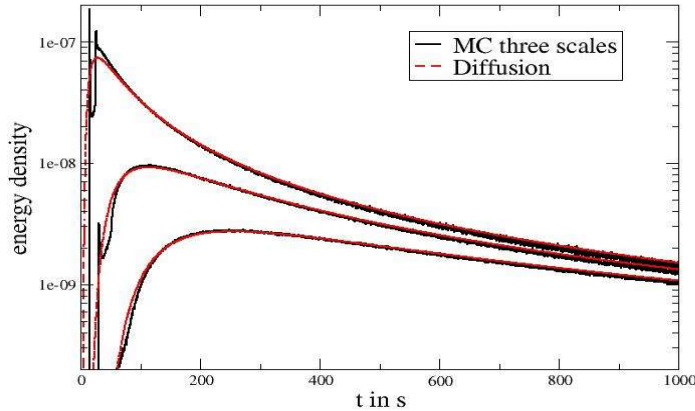


Figure 2. Monte Carlo simulations in a three scale Gaussian random medium (red curves) compared with solutions of the diffusion equation (black curves) for three radial distances ($r=100$ km, 200 km, 300 km). Medium parameters are the same as in fig.1, but the source radiates S wave energy too. There is a very good agreement between both solutions after the S wave onsets.

References

Goff, J.A. and Holliger, K., Nature and origin of upper crustal seismic velocity fluctuations and associated scaling properties: Combined stochastic analysis of KTB velocity and lithology logs, *J. Geophys. Res.*, Vol.104, pp. 13169-13182, 1999.

Przybilla, J., Wegler, U., Korn, M., Estimation of crustal scattering parameters with elastic radiative transfer theory, *Geophys. J. Int.*,

(early view), doi: 10.1111/j.1365-246X.2009.04204.x, 2009.

Przybilla, J. and Korn, M., Monte Carlo simulation of radiative energy transfer in continuous elastic random media - three component envelopes and numerical validation, *Geophys. J. Int.*, Vol. 173, pp. 566-576 ,doi: 10.1111/j.1365-246X.2008.03747.x1 , 2008.

Retrieval of the Green function having coda for a scattering medium from noise correlation: the Born approximation

Haruo Sato

Graduate School of Science, Tohoku University, Aoba-ku, Sendai 980-8578, Japan, E-mail: sato@zisin.geophys.tohoku.ac.jp

Introduction

Noise correlation method is now widely used for the retrieval of the Green function of the earth medium even if there is no real explosive source [Campillo and Paul, 2003; Shapiro et al., 2005]. Some geophysicists pay attention not only to the peak lag of the cross correlation function (CCF) but also to the coda portion. Wegler and Sens-Schonfelder [2007] recently reported the temporal change in the coda phases of the correlation function of ambient noises before and after a crustal earthquake.

The spatial autocorrelation (SPAC) method of Aki [1957] is one of the roots of these approaches. Ambient noises are thought to be composed of omnidirectional waves with the same amplitude, as a realization of the equipartition state in the wavenumber space. The equipartition state is often used as the basic assumption for the retrieval of the Green function from noise correlation even for elastic waves [e. g. Sánchez-Sesma et al., 2006].

There have been theoretical studies how to derive the Green function for a given medium illuminated by noise sources. In most studies noise sources are supposed to be stationary in time and their distribution is randomly isotropic and homogeneous in space; however, there are different models for the range of noise distribution in space. One is a distribution on a closed surface enclosing the study medium. Weaver and Lobkis [2004] and Wapenaar and Fokkema [2006] mathematically showed the Green function retrieval from the CFF by using the reciprocal theorem of the correlation type in the case of no dissipation. When the medium is illuminated by noise sources distributed on a spherical shell with large radius compared with the dimension of the scattering medium, waves at receivers can be approximated as omnidirectional plane waves. Sato [2009]

successfully derived the retrieval of the Green function having coda from the CFF for a scattering medium by using the first order Born approximation. Another manifestation is a uniform distribution of noise sources in space. Snieder [2004] used the method of steepest descent for the Green function retrieval for a homogenous medium. Roux et al. [2006] used the prolate spheroidal coordinates for the Green function retrieval for a homogeneous medium with dissipation.

Here, using a specific model for a scattering medium, we study how the Green function is retrieved from noise CCF for different two types of noise source distributions.

Green function for a scattering medium with dissipation

Let us imagine a distribution of velocity anomalies (scattering medium) D_s with the maximum radius R_s (see Figure 1 (a)) in a 3-D homogenous medium with background velocity V_0 and small dissipation κ . When the spatial dimension of each velocity anomaly d is much smaller than the wavelength, we may write the inhomogeneous velocity by using a delta function as $V(\mathbf{x}) = V_0 + V_0 \sum_{j=1}^N \varepsilon_j d^3 \delta(\mathbf{x} - \mathbf{y}_j)$, where ε_j is a small parameter characterizing the j -th scatterer at location \mathbf{y}_j . The wave equation for real wave field $\phi(\mathbf{x}, t)$ for an external source N is given by

$$\begin{aligned} \Delta\phi(\mathbf{x}, t) - \frac{1}{V_0^2} (\partial_t + V_0 \kappa)^2 \phi(\mathbf{x}, t) \\ + 2 \frac{d^3}{V_0^2} \sum_{j=1}^N \varepsilon_j \delta(\mathbf{x} - \mathbf{y}_j) \partial_t^2 \phi(\mathbf{x}, t) = N(\mathbf{x}, t). \end{aligned} \quad (1)$$

According to the first order Born approximation, we have the Green function in

the angular frequency domain for a receiver at \mathbf{x}_A and a source \mathbf{x}_B as

$$\begin{aligned}\hat{G}(\mathbf{x}_A, \mathbf{x}_B, \omega, \kappa) &= -\frac{1}{4\pi h_{AB}} e^{ik_0 h_{AB} - \kappa h_{AB}} \\ &+ 2d^3 k_0^2 \sum_{j=1}^N \varepsilon_j \frac{e^{ik_0 h_{Aj} - \kappa h_{Aj}}}{4\pi h_{Aj}} \frac{e^{ik_0 h_{Bj} - \kappa h_{Bj}}}{4\pi h_{Bj}},\end{aligned}\quad (2)$$

where $h_{AB} = |\mathbf{x}_A - \mathbf{x}_B|$, $h_{Aj} = |\mathbf{x}_A - \mathbf{y}_j|$ and $h_{Bj} = |\mathbf{x}_B - \mathbf{y}_j|$.

Distribution of noise sources in infinite 3-D space

Stationary noise sources with the spectrum $\hat{N}(\mathbf{x}, \omega)$ are distributed in infinite 3-D space. Waves excited by those noise sources are given by

$$\begin{aligned}\hat{\phi}(\mathbf{x}_A, \omega) &= \iiint_{-\infty}^{\infty} \hat{G}(\mathbf{x}_A, \mathbf{x}, \omega, \kappa) \hat{N}(\mathbf{x}, \omega) d\mathbf{x}, \\ \hat{\phi}(\mathbf{x}_B, \omega) &= \iiint_{-\infty}^{\infty} \hat{G}(\mathbf{x}_B, \mathbf{x}, \omega, \kappa) \hat{N}(\mathbf{x}, \omega) d\mathbf{x}.\end{aligned}\quad (3)$$

We imagine an ensemble of noise sources $\{N\}$: the spatial distribution of noise sources is randomly uniform and isotropic (See Figure 1 (b)) and each stationary noise source has the same power spectral density function $\hat{S}_N(\omega)$. Then, we may write the ensemble average of the noise as

$$\lim_{T \rightarrow \infty} \frac{\langle \hat{N}(\mathbf{x}, \omega)^* \hat{N}(\mathbf{x}', \omega) \rangle}{T} = \delta(\mathbf{x} - \mathbf{x}') \hat{S}_N(\omega), \quad (4)$$

where T is the time window length. It is clear that the resultant wave fields are randomly uniform and isotropic, that is, an equipartition state is realized. Taking the average of the CCF of waves at two receivers over the ensemble of noise sources, we have

$$\begin{aligned}\lim_{T \rightarrow \infty} \frac{1}{T} \int_{-T/2}^{T/2} \langle \phi(\mathbf{x}_A, t - \tau) \phi(\mathbf{x}_B, t) \rangle dt \\ = \frac{1}{2\pi} \int_{-\infty}^{\infty} d\omega e^{-i\omega\tau} \hat{S}_N(\omega) \\ \times \iiint_{-\infty}^{\infty} \hat{G}(\mathbf{x}_A, \mathbf{x}, \omega, \kappa)^* \hat{G}(\mathbf{x}_B, \mathbf{x}, \omega, \kappa) d\mathbf{x}.\end{aligned}\quad (5)$$

Substituting (2) into (5) and neglecting the second and higher order terms of ε_j , we have

$$\begin{aligned}&\iiint_{-\infty}^{\infty} d\mathbf{x} \hat{G}(\mathbf{x}_A, \mathbf{x}, \omega, \kappa)^* \hat{G}(\mathbf{x}_B, \mathbf{x}, \omega, \kappa) \\ &= \iiint_{-\infty}^{\infty} d\mathbf{x} \frac{e^{-ik_0 r_{Ax} - \kappa r_{Ax}}}{4\pi r_{Ax}} \frac{e^{ik_0 r_{Bx} - \kappa r_{Bx}}}{4\pi r_{Bx}} \\ &- 2k_0^2 d^3 \sum_{j=1}^N \varepsilon_j \frac{e^{ik_0 h_{Bj} - \kappa h_{Bj}}}{4\pi h_{Bj}} \iiint_{-\infty}^{\infty} d\mathbf{x} \frac{e^{-ik_0 r_{Ax} - \kappa r_{Ax}}}{4\pi r_{Ax}} \frac{e^{ik_0 r_{jx} - \kappa r_{jx}}}{4\pi r_{jx}} \\ &- 2k_0^2 d^3 \sum_{j=1}^N \varepsilon_j \frac{e^{-ik_0 h_{Ax} - \kappa h_{Ax}}}{4\pi h_{Ax}} \iiint_{-\infty}^{\infty} d\mathbf{x} \frac{e^{-ik_0 r_{jx} - \kappa r_{jx}}}{4\pi r_{jx}} \frac{e^{ik_0 r_{Bx} - \kappa r_{Bx}}}{4\pi r_{Bx}}, \\ \text{where } r_{Ax} &= |\mathbf{x}_A - \mathbf{x}|, r_{Bx} = |\mathbf{x}_B - \mathbf{x}| \quad \text{and} \\ r_{jx} &= |\mathbf{y}_j - \mathbf{x}|.\end{aligned}\quad (6)$$

For a pair of receivers A and B, noise sources on a hyperboloid $r_{Ax} - r_{Bx} = V_0 \tau$ coherently contribute to the CCF at lag time τ . Therefore, it is convenient for us to use the prolate spheroidal coordinates (w, v, ϕ) having \mathbf{x}_A and \mathbf{x}_B as the foci, where w and v determine a hyperboloid and an ellipsoid scaled by the receiver separation as $r_{Bx} - r_{Ax} = h_{AB} w$ and $r_{Ax} + r_{Bx} = h_{AB} v$. We can introduce prolate spheroidal coordinates for a pair of receiver and scatterer, too. Performing the integration by using those prolate spheroidal coordinates, we have

$$\begin{aligned}\iiint_{-\infty}^{\infty} d\mathbf{x} \hat{G}(\mathbf{x}_A, \mathbf{x}, \omega, \kappa)^* \hat{G}(\mathbf{x}_B, \mathbf{x}, \omega, \kappa) \\ = -\frac{1}{2k_0 \kappa} \text{Im} \left[-\frac{e^{ik_0 h_{AB} - \kappa h_{AB}}}{4\pi h_{AB}} + 2k_0^2 d^3 \sum_{j=1}^N \varepsilon_j \frac{e^{ik_0 h_{Aj} - \kappa h_{Aj}}}{4\pi h_{Aj}} \frac{e^{ik_0 h_{Bj} - \kappa h_{Bj}}}{4\pi h_{Bj}} \right] \\ = -\frac{1}{2k_0 \kappa} \text{Im} \hat{G}(\mathbf{x}_A, \mathbf{x}_B, \omega, \kappa),\end{aligned}\quad (7)$$

where geometrical decay factor and exponential dissipation effect correctly appear in the single scattering term. We note that the effective distance range κ^{-1} should be larger than R_s and h_{AB} . Substituting (7) into (5), we have

$$\begin{aligned}\frac{1}{V_0} \frac{d}{d\tau} \left[\lim_{T \rightarrow \infty} \frac{1}{T} \int_{-T/2}^{T/2} \langle \phi(\mathbf{x}_A, t - \tau) \phi(\mathbf{x}_B, t) \rangle dt \right] \\ = \frac{1}{4\pi} \int_{-\infty}^{\infty} [G(\mathbf{x}_A, \mathbf{x}_B, \tau - \tau', \kappa) - G(\mathbf{x}_A, \mathbf{x}_B, -\tau - \tau', \kappa)] S(\tau') d\tau'.\end{aligned}\quad (8)$$

The derivative of CFF with respect to lag time is equivalent to the convolution of the anti-symmetrized Green function and the noise ACF. The proportional relation $\iiint_{-\infty}^{\infty} d\mathbf{x} \hat{G}(\mathbf{x}_A, \mathbf{x})^* \hat{G}(\mathbf{x}_B, \mathbf{x}) \propto \text{Im} \hat{G}(\mathbf{x}_A, \mathbf{x}_B)$ is the key for the derivation of (8). This derivation for a scattering medium is an extension of Roux et al. [2005] for a homogenous medium. As an example, we schematically illustrate the time derivative of CCF having coda tails for a scattering medium in Figure 2.

Distribution of noise sources in a spherical shell

We study another case that the distribution of noise sources are randomly uniform and isotropic in a spherical shell of radius R with small thickness ΔR , where $R \gg R_s > h_{AB} \gg \Delta R$. If there is dissipation, the wave intensity decreases as the radius decreases. In order to satisfy the equipartition state in the scattering medium for this type of noise illumination, we suppose no dissipation, $\kappa = 0$, that is, the system is time reversal. Changing the integral region in (6) into a spherical shell of radius R , we have

$$\begin{aligned} & \iint \int_{\text{Shell } R} d\mathbf{x} \hat{G}(\mathbf{x}_A, \mathbf{x}, \omega, \kappa = 0)^* \hat{G}(\mathbf{x}_B, \mathbf{x}, \omega, \kappa) \\ & \approx \Delta R \oint \frac{1}{16\pi^2} e^{ik_0 h_{AB} \cos \theta} \sin \theta d\theta d\phi \\ & - \Delta R \frac{d^3 k_0^2}{8\pi^2} \sum_{j=1}^N \varepsilon_j \frac{e^{-ik_0 h_{Aj}}}{4\pi h_{Aj}} \oint e^{ik_0 h_0 \cos \theta} e^{ik_0 h_j \cos \psi_j} \sin \theta d\theta d\phi \\ & - \Delta R \frac{d^3 k_0^2}{8\pi^2} \sum_{j=1}^N \varepsilon_j \frac{e^{ik_0 h_{Bj}}}{4\pi h_{Bj}} \oint e^{ik_0 h_0 \cos \theta} e^{-ik_0 h_j \cos \psi_j} \sin \theta d\theta d\phi, \end{aligned} \quad (9)$$

where θ is the angle between \mathbf{x} and \mathbf{x}_A at the origin, and ψ_j is the angle between \mathbf{y}_j and \mathbf{x} at the origin: $\cos \psi_j = \cos \theta \cos \theta_j + \sin \theta \sin \theta_j \cos(\phi - \phi_j)$. We used the approximation $r_A \approx r_B \approx r_j \approx R$ in geometrical factors since $R \gg R_s$. We further approximated the distance in the exponent in each term as follows: $r_A \approx R - h_0 \cos \theta$, $r_B \approx R + h_0 \cos \theta$, and $r_j \approx R - h_{0j} \cos \psi_j$. This is the plane wave approximation. Then Eq. (9) can be written as

$$\begin{aligned} & \iint \int_{\text{Shell } R} d\mathbf{x} \hat{G}(\mathbf{x}_A, \mathbf{x}, \omega, \kappa = 0)^* \hat{G}(\mathbf{x}_B, \mathbf{x}, \omega, \kappa = 0) \\ & = -\frac{\Delta R}{k_0} \text{Im} \left[-\frac{e^{ik_0 h_{AB}}}{4\pi h_{AB}} + 2k_0^2 \sum_{j=1}^N \varepsilon_j d^3 \frac{e^{ik_0 h_{Aj}}}{4\pi h_{Aj}} \frac{e^{ik_0 h_{Bj}}}{4\pi h_{Bj}} \right] \\ & = -\frac{\Delta R}{k_0} \text{Im} G(\mathbf{x}_A, \mathbf{x}_B, \omega, \kappa = 0). \end{aligned} \quad (10)$$

This relation for the scattering medium is derived in Sato [2009]. The retrieval of the Green function having coda is possible as follows:

$$\begin{aligned} & \frac{1}{V_0} \frac{d}{dt} \left[\lim_{T \rightarrow \infty} \frac{1}{T} \int_{-T/2}^{T/2} \langle \phi(\mathbf{x}_A, t - \tau) \phi(\mathbf{x}_B, t) \rangle dt \right] = \frac{\Delta R}{2} \\ & \times \int_{-\infty}^{\infty} [G(\mathbf{x}_A, \mathbf{x}_B, \tau - \tau', \kappa = 0) - G(\mathbf{x}_A, \mathbf{x}_B, -\tau - \tau', \kappa = 0)] S(\tau') d\tau'. \end{aligned} \quad (11)$$

Conclusion

We have theoretically studied the retrieval of the Green function having a coda tail for a scattering medium from the CCF of waves generated by distributed stationary noise sources. We examined two types of noise source distributions that lead to the equipartition state.

For the case that the distribution of noise sources is randomly homogeneous and isotropic in an infinite 3-D media with dissipation, we have shown that the Green function is well retrieved from the CFF on the basis of the first order Born approximation: the derivative of CCF with respect to lag time is proportional to the anti-symmetrized Green function which has a coda tail caused by single scattering in the scattering medium and an exponential decay term caused by dissipation. The Green function retrieval is possible even when the time reversal symmetry is broken.

Another case is that a scattering medium and receivers are illuminated by noise sources distributed on a spherical shell with large radius compared with the dimension of the scattering medium. In the case of no dissipation, The Green function having coda can be retrieved from the CFF.

We find that the retrieval of the Green function for a scattering medium from noise CFF is possible for the equipartition state even if there is dissipation. When we focus on the coda portion of CFF of noises in observation, it is necessary for us to pay more attention to the configuration of noise sources and examine whether the equipartition is established. This study is limited to the case of single scattering, therefore, it will be necessary for us to examine the retrieval of the Green function having multiple scattering terms of higher orders. We used a model composed of delta function anomalies; however, it will be necessary to examine different types of anomalies that lead to nonisotropic scattering and phase shifts depending on frequency.

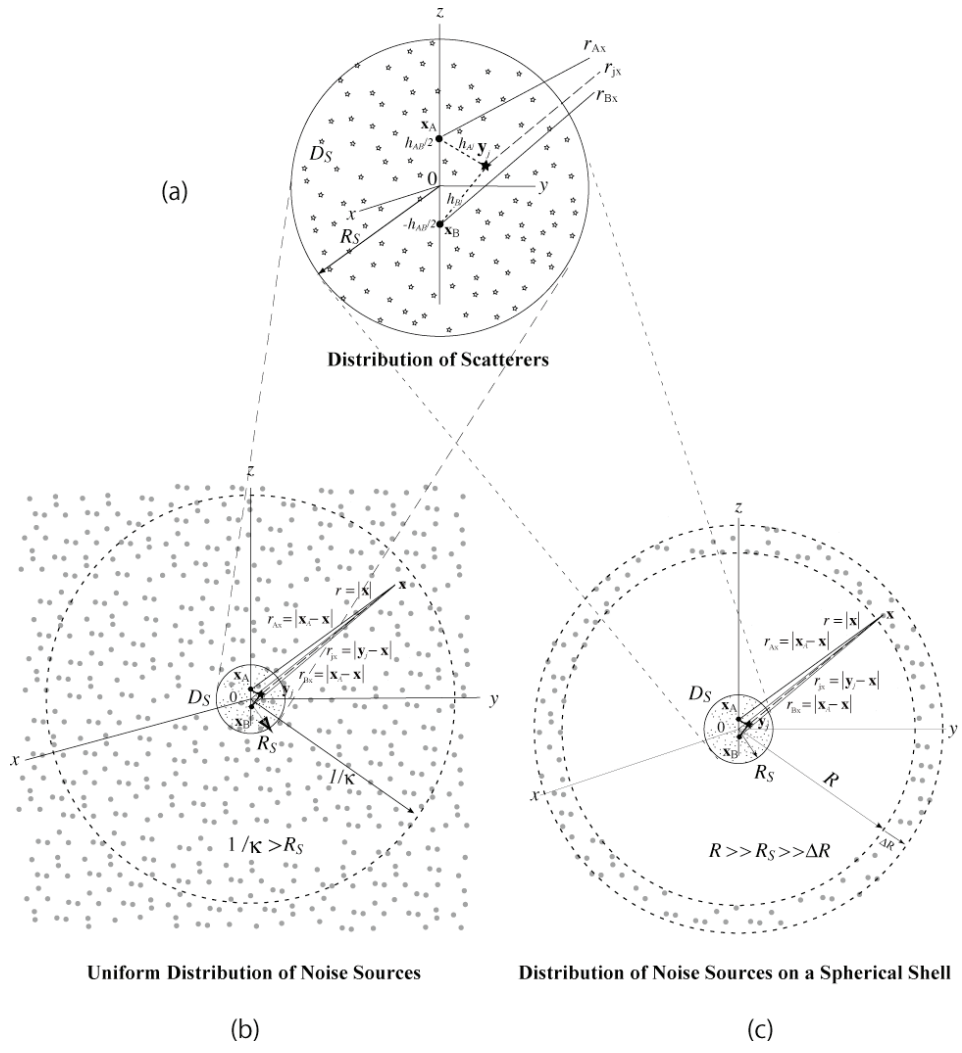


Figure 1. (a) Scattering medium D_s as a distribution of scatterers (stars). (b) Scattering medium D_s is illuminated by noise sources (gray circles) randomly distributed in an infinite 3-D medium with small dissipation κ . (c) Scattering medium D_s is illuminated by noise sources (gray circles) randomly distributed in a thin spherical shell of radius R .

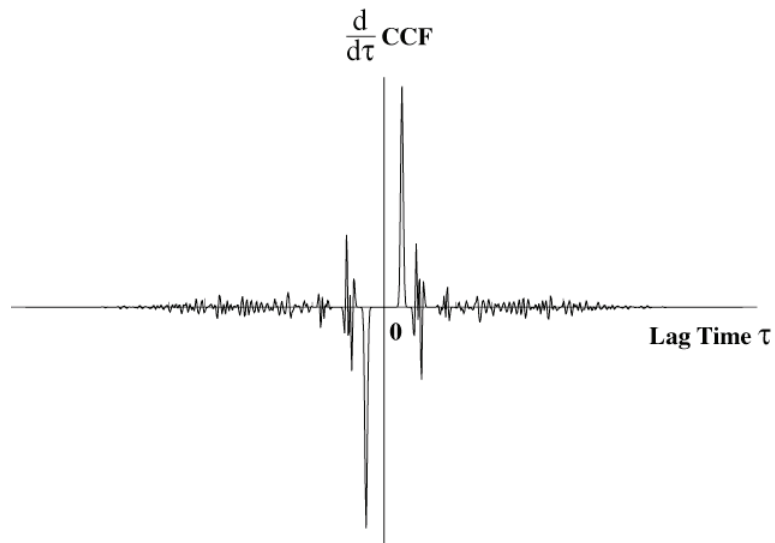


Figure 2. Schematic illustration of the time derivative of CCF having coda in a scattering medium.

References

- Aki, K. (1957) Space and time spectra of stationary stochastic waves, with special reference to microtremors, *Bull. Earthq. Res. Inst.*, 35, 415–456.
- Campillo M. and A. Paul (2003) Long-range correlations in the diffuse seismic coda, *Science*, 299, 547–549.
- Roux, P., K. G. Sabra, W. A. Kuperman, and A. Roux (2005) Ambient noise cross correlation in free space: Theoretical approach, *J. Acoust. Soc. Am.*, 117, 79–84.
- Sánchez-Sesma, F. J., J. A. Pérez-Ruiz, M. Campillo, and F. Luzón (2006), Elastodynamic 2D Green function retrieval from cross-correlation: Canonical inclusion problem, *Geophys. Res. Lett.*, 33, L13305, doi:10.1029/2006GL026454.
- Sato, H. (2009) Retrieval of the Green function having coda from the cross-correlation function in a scattering medium illuminated by surrounding noise sources on the basis of the first order Born approximation, preprint.
- Shapiro, N. M., M. Campillo, L. Stehly, M. H. Ritzwoller (2005) High-Resolution Surface-Wave Tomography from Ambient Seismic Noise, *Science*: 307, 1615 – 1618, DOI: 10.1126/science.1108339.
- Snieder, R. (2004), Extracting the Green's function from the correlation of coda waves: A derivation based on stationary phase, *Phys. Rev. E*, 69, 046610, 1-8. DOI: 10.1103/PhysRevE.69.046610
- Wapenaar, K. and J. Fokkema (2006) Green's function representations for seismic interferometry, *Geophys.*, 71, SI33–SI46,
- Weaver, R. L. and O. L. Lobkis (2004) Diffuse fields in open systems and the emergence of the Green's function, *J. Acoust. Soc. Amer.*, 116, 2731–2734.
- Wegler, U. and C. Sens-Schonfelder (2007), Fault zone monitoring with passive image interferometry, *Geophys. J. Int.*, 168, 1029–1033.

Detection of subtle changes in materials by Coda Wave interferometry

Simon Stähler¹, Ernst Niederleithinger², Stephan Pirskawetz², Thomas-Rudolf Nowak², Frank Weise²

¹ Institute of Geophysics and Geology, University of Leipzig, Germany, E-mail: sstaehtler@gmx.de

² BAM Federal Institute for Material Research and Testing, Berlin, Germany, E-mail: Ernst.Niederleithinger@bam.de

Ultrasonic velocity measurements are an established tool in material science to detect structural information and changes in lab samples. Difficulties arise, when small changes in velocity have to be detected or the wavelength of the ultrasonic signals is in the order of magnitude of the internal structure of the samples.

Coda Wave Interferometry (CWI) is currently mainly used to detect slight velocity changes on one side in the earth's crust due to seismic effects, mining influence or seasonal variations and on rock samples on the other. The coda of seismic or ultrasonic signals before during and after events or loads is evaluated to detect time shifts.

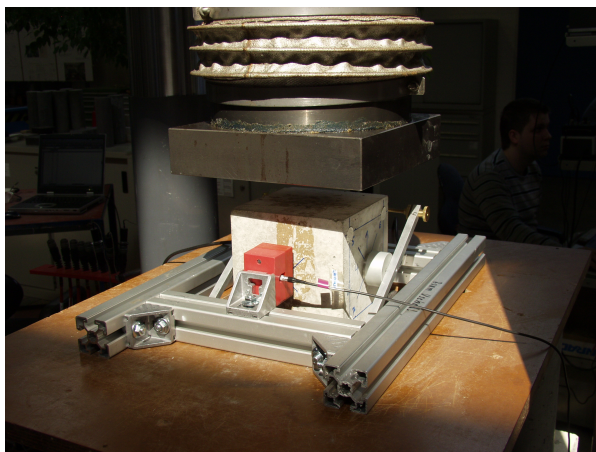


Figure 1. Experimental setup: Concrete cube under 1 MN load frame, equipped with 125 kHz point contact (red, front/back) and 250 kHz conventional piezo transducers (silver, left/right).

An preliminary experiment on two concrete cubes ($15 \times 15 \times 15 \text{ cm}^3$) has been conducted at BAM to evaluate the potential of CWI and to support a field study at the University of Leipzig. Two ultrasonic setups, normally used for time of flight measurements, were used to generate and receive signals in transmission mode (Fig. 1). Similar and more sophisticated

experiments have been published e. g., by Larose et al (2009).

Time of Flight – the classic approach

In a first step the ultrasonic transmission data (Fig. 2 top) was evaluated by evaluating the time of flight (TOF). Due to the high noise level caused by the load frame we had to stack 32 measurements. The Akaike information criterion (AIC) as proposed by Tronicke (2007) was used to pick most of the arrival times.

The Compression wave velocity for zero load calculated from TOF was $(4550 \pm 150) \text{ ms}^{-1}$. The velocity changes for different loads are plotted in Figure 3. The slight velocity change expected at small to medium loads ("acoustoelastic effect") is not visible due to the up to 5% scatter caused by noise and sample interval. The first arrival times are almost identical (Fig. 2 middle). The irreversible velocity drop during high loads (caused by microcracking) is about 10%.

Coda Wave Interferometry

To detect smaller velocity changes, the time series were evaluated by the stretching correlation proposed by Sens-Schönfelder & Wegler (2006) in a time window of 0.5 ms, starting 0.25 ms after the trigger. This way different stress-related effects could be seen. Even for small stress changes of 50 kPa, the acoustoelastic effect was visible, contributing to velocity changes of $(2.4 \pm 0.1) \cdot 10^{-3} \text{ MPa}^{-1}$ (Fig. 4).

The correlation coefficient between the reference trace and the stretched second trace was well above 0.9 for all displayed measurements.

When evaluating a larger range of loads, other effects were visible (Fig. 3). After loading the cube with 500 kN ($\sim 22 \text{ MPa}$), and releasing

the stress back to zero, the velocity had dropped for approx. 2.5 %. (Figure 5) When increasing the pressure, the old velocities were reached again. At about 35 MPa, the velocity began to decrease, as seen in the TOF results. Above 45 MPa the correlation coefficient dropped below 0.3 as the signal shapes changed significantly so that an evaluation with this method was not possible anymore.

Conclusion

The Coda wave interferometry using the stretching correlation allows it to detect very subtle wave velocity changes in concrete which are not detectable by evaluation of the direct wave's Time of Flight. As the TOF measurements are more stable against changes in the signal shape, this method is easier applicable for large stress changes.

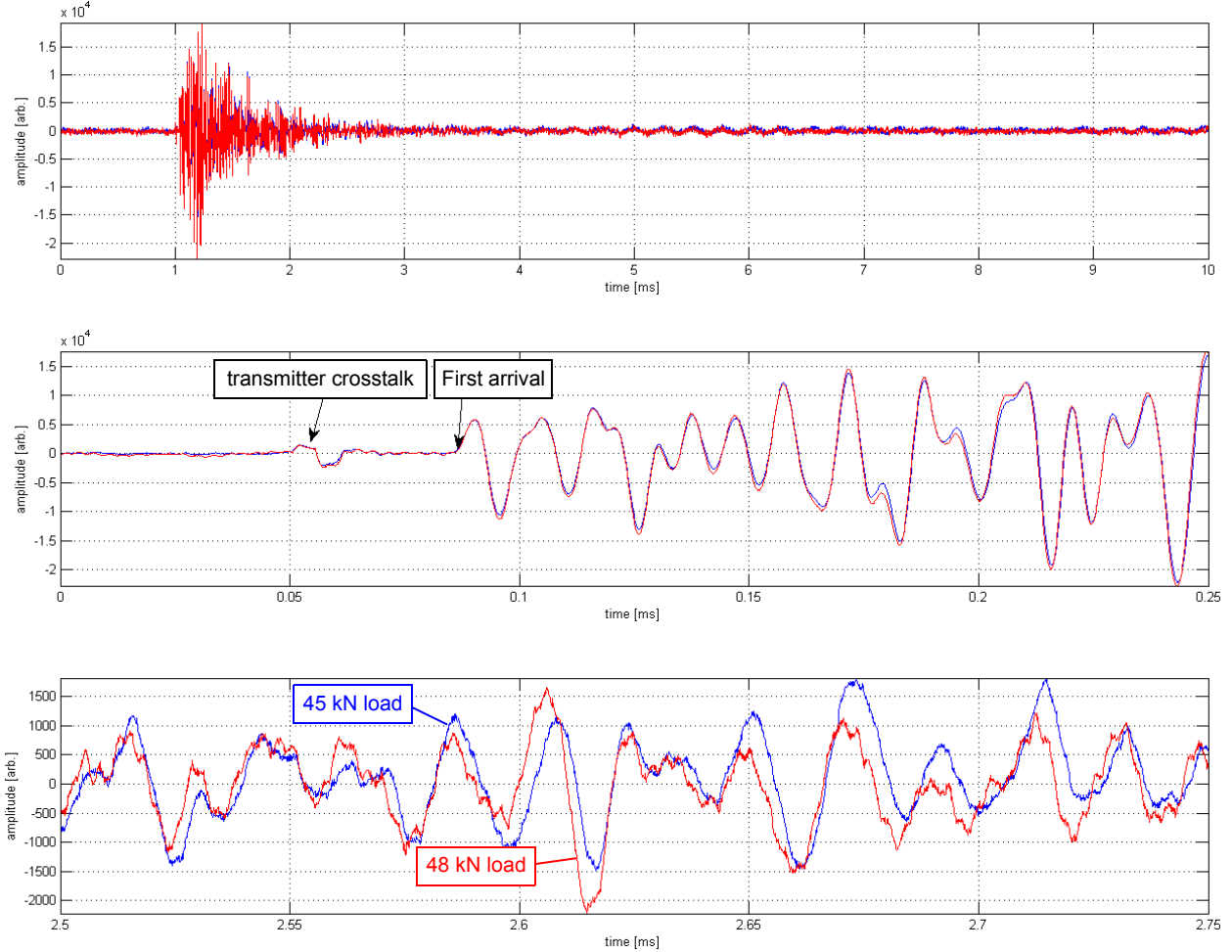


Figure 2. Typical time series (point contact transducers, 32 stacks, 1 ms pre-trigger, 10 ms sampling time, 10 MHz sampling frequency) at 45 kN (2 MPa, blue) and 48 kN load (2.13 MPa, red). Top: Entire signal. Middle: Detail near first arrival Bottom: Detail of coda wave. Significant phase shift visible

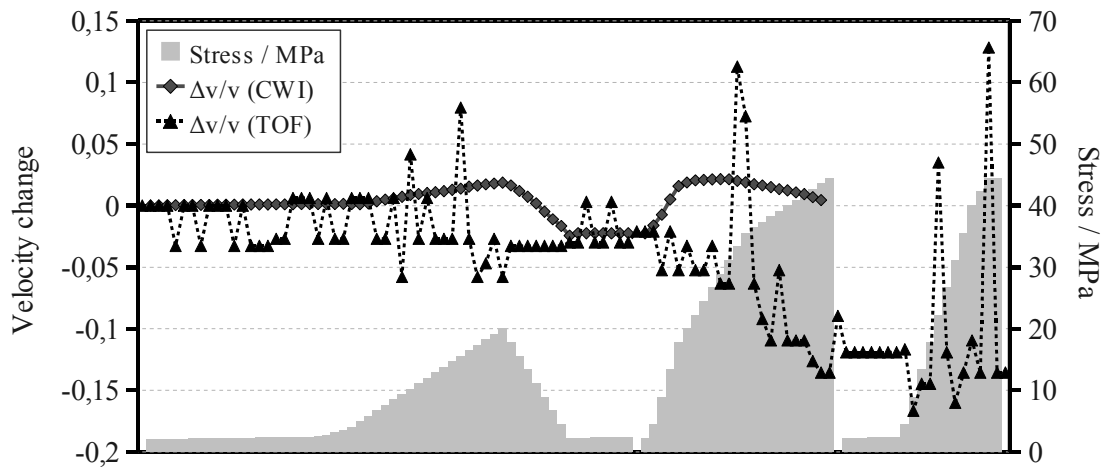


Figure 3. Comparison of Wave velocity change estimations from TOF and CWI in dependence of load cycles. CWI suitable for detecting small velocity changes but problematic for larger ones. For TOF the velocity drop after high load is visible, velocity increase at small loads is not.

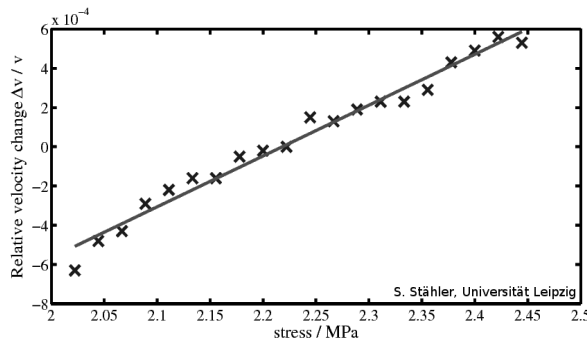


Figure 4. Velocity changes at small stress levels (acoustoelastic effect) evaluated by CWI. Corresponds to load step 1 to 21 of Fig. 3.

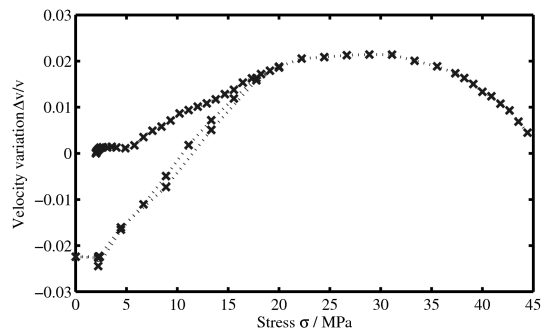


Figure 5. Wave velocity hysteresis curve evaluated by CWI. Visible is the acoustoelastic effect, the 2.5% velocity drop after first load of 20 MPa and the beginning of the larger velocity drop above 32 MPa. Corresponds to load steps 1 to 80 of Fig. 3

References

- A. Zoëga & H. Wiggenhauser, 2008: Propagation time of elastic surface waves on concrete specimens under uniaxial loads. Proceedings of SMT, Oakland, CA.
- E. Larose & S. Hall, 2009: Monitoring stress related velocity variation in concrete with a 2.10-5 relative resolution using diffuse ultrasound. J. Acoust. Soc. Am. 125, 4 (2009) 1853-1856.
- J. Tronicke, (2007): The influence of high frequency uncorrelated noise on first-break arrival times and crosshole traveltime tomography. Journal of Environmental and Engineering Geophysics, 12, 173-184.
- C. Sens-Schönfelder & U. Wegler, 2006: Passive Image Interferometry and seasonal variations of seismic velocities at Merapi volcano, Indonesia. Geophys. Res. Lett 33, L21302.

Monitoring Temporal Changes in Seismically Active Areas Using Ambient Seismic Noise

Ulrich Wegler¹, Hisashi Nakahara², Christoph Sens-Schönfelder³, Michael Korn³, Katsuhiko Shiomi⁴

¹ Federal Institute for Geosciences and Natural Resources (BGR), Hannover D-30655, Germany, E-mail: ulrich.wegler@bgr.de

² Graduate School of Science, Tohoku University, Aoba-ku, Sendai 980-8578, Japan, E-mail: naka@zisin.geophys.tohoku.ac.jp

³ Institute of Geophysics and Geology, University of Leipzig, Germany, E-mail: mikorn@uni-leipzig.de, sens-schoenfelder@uni-leipzig.de

⁴ National Research Institute for Earth Science and Disaster Prevention, Ibaraki 305-0006, Japan, E-mail: shiomi@bosai.go.jp

Ambient seismic noise can be used to monitor small temporal changes in the earth's crust. First, the elastic Green's tensor between two seismometers is computed by cross-correlating seismic noise recorded during a certain time period. In a second step, the constructed seismograms of different time periods are treated as earthquake multiplets and small time shifts in their coda are used to invert a relative change in mean shear wave velocity. We call this technique "Passive Image Interferometry (PII)". The major advantage of using noise as a source is that it is continuously available, which results in a denser temporal coverage of measurements than in active source or earthquake multiplet studies.

We applied Passive Image Interferometry to the source region of the Mid Niigata Prefecture earthquake of 2004, Japan, which had a centroid-depth of 5 km and a moment Magnitude of 6.6 (Wegler and Sens-Schönfelder, 2007; Wegler et al., in press). We used noise recorded at 5 seismometers of Hi-net, the Japanese High-Sensitivity seismograph network, and one station of F-net, the Japanese Broadband Seismograph Network (Figure 1). All stations are located in a distance of less than 25 km from the epicenter. We constructed seismograms using noise in the two different frequency bands of 0.1 - 0.5 Hz and of 2 - 8 Hz. Using high frequency noise (2 - 8 Hz) one day of data is generally sufficient to estimate the source-receiver co-located Green's function, which leads to a temporal resolution of one day.

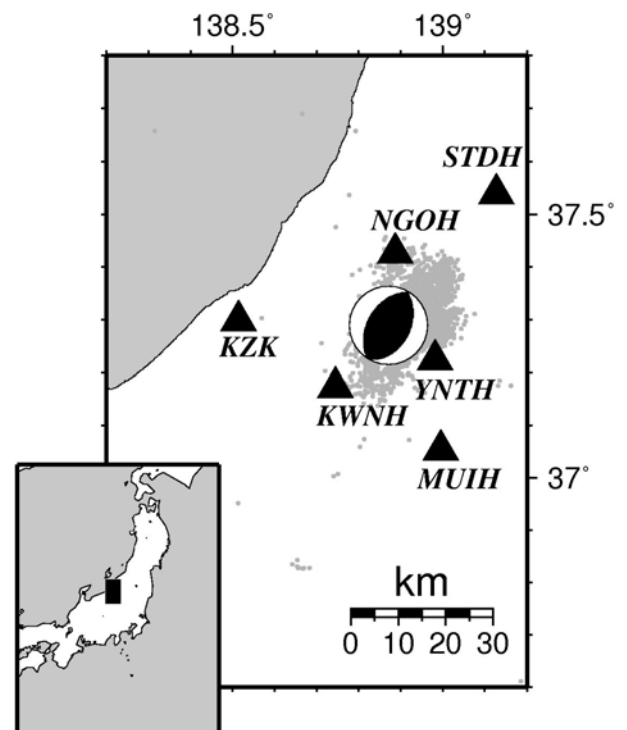


Figure 1. Source region of the Mid Niigata prefecture earthquake of Oct. 23., 2004: Locations of Hi-net sensors KWNH, MUIH, NGOH, STDH, and YNTH as well as F-net station KZK (triangles). The beachball indicates the hypocenter of the mainshock according to JMA and its focal mechanism determined by F-net. Small gray dots indicate hypocenters of aftershocks during Oct. 23-31 according to the JMA catalogue.

Using lower frequencies (0.1 - 0.5 Hz), on the other hand, much longer noise time series in the order of weeks are required to compute the Green's function. The advantage of using lower frequencies is that Green's functions for larger station distances can be computed,

whereas for high frequencies due to the lack of coherence in many cases only source-receiver co-located Green's functions can be constructed from the auto-correlation of noise at a single station. Applying the technique to the source region of the Mid-Niigata earthquake we revealed a rapid co-seismic drop in relative seismic velocity of some tenths of a percent (figures 2 and 3), that spatially roughly coincides with the earthquake source area. The fact that the velocity decrease measured in the 2 – 8 Hz frequency band has a similar amplitude as the velocity decrease measured in the 0.1 - 0.5 Hz frequency band is some indication that the change is not restricted to the shallow subsurface.

Based on Passive Image Interferometry, a co-seismic decrease of seismic velocity was also revealed for the 2007 Noto Hanto, Japan,

earthquake (Ohmi et al., 2008), the 2004 Parkfield, California, earthquake (Brenguier et al. 2008), and the 2005 Fukuoka-Ken Seiho-Oki, Japan, earthquake (Nakahara et al., submitted). The fact of crustal seismic velocity reductions during large crustal earthquakes and the validity of Passive Image Interferometry are therefore well established. The physical mechanism causing the co-seismic velocity drop, on the other hand, could not be completely clarified. A non-linear site response in the shallow subsurface layer due to strong ground motion and structural weakening due to the creation of new fractures in the fault zone are consistent with our data. Static stress changes, on the contrary, cannot explain the fact that only decreases in velocity are observed, whereas regions of increasing velocity are not observed in our study.

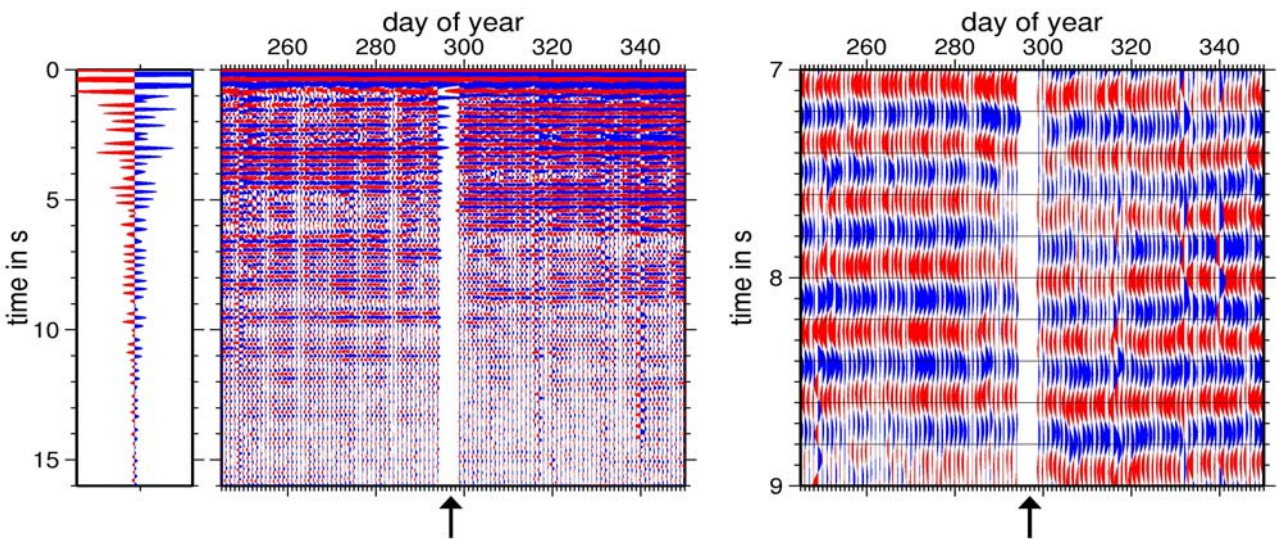


Figure 2. Temporal evolution of the source-receiver co-located Green's function constructed from the auto-correlation of seismic noise at station KZK during a period of four months. The Green's function is averaged over one day and shown as a function of the day of the year. The black arrow indicates the occurrence of the Mid-Niigata earthquake. Red and blue wiggles correspond to positive and negative amplitudes of the Green's function, respectively. White space near the day of the Mid-Niigata earthquake is caused by the lack of data for four days. Right: Same as left, but for an enlarged time window from 7 to 9 s. Note the time-shift in the Green's function after the earthquake.

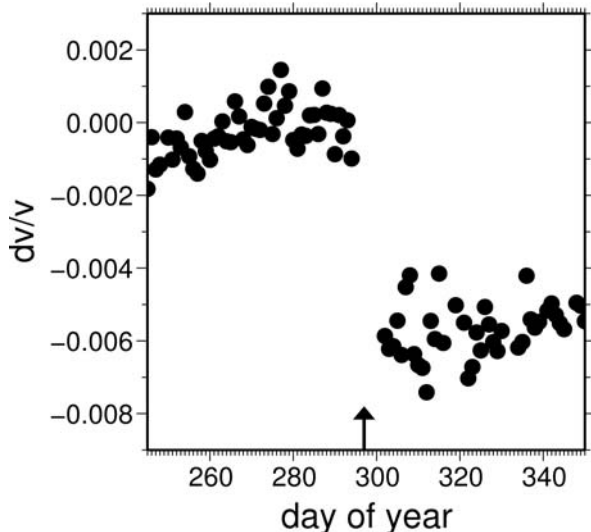


Figure 3. Relative seismic velocity dv/v as a function of the day of the year. The arrow indicates the day of the Mid-Niigata earthquake.

References

Brenguier, F., M. Campillo, C. Hadzioannou, N. M. Shapiro, R. Nadeau, and E. Larose (2008), Postseismic relaxation along the San Andreas fault at Parkfield from continuous seismological observations, *Science*, v. 321, pp. 1478–1481.

Nakahara, H., U. Wegler, and K. Shiomi (submitted), Monitoring seismic velocity changes using Passive Image Interferometry: an application to the 2005 West Off Fukuoka Prefecture, Japan, earthquake (Mw 6.6), *Geophys. J. Int.*

Ohmi, S., K. Hirahara, H. Wada, and k. Ito (2008), Temporal variations of crustal structure in the source region of the 2007 Noto Hanto earthquake, central Japan, with Passive Image Interferometry, *Earth Planets Space*, v. 60, pp.1069–1074.

Wegler, U. and C. Sens-Schönfelder (2007), Fault zone monitoring with Passive Image Interferometry, *Geophys. J. Int.*, v. 168, pp. 1029-1033, doi:10.1111/j.1365-246X.2006.03284.x.

Wegler, U., H. Nakahara, C. Sens-Schönfelder, M. Korn, and K. Shiomi (in press), Sudden Drop of Seismic Velocity after the 2004 Mw 6.6 Mid-Niigata earthquake, Japan, Observed with Passive Image Interferometry, *J. Geophys. Res.*, doi:10.1029/2008JB005869.

Temporal changes in site response associated with strong ground motion of 2004 Mw6.6 Mid-Niigata earthquake sequences in Japan

Chunquan Wu¹, Zhigang Peng¹, Dominic Assimaki²

¹ School of Earth and Atmospheric Sciences, Georgia Institute of Technology, Atlanta, GA, 30332, USA, E-mail: chunquanwu@gatech.edu, zpeng@gatech.edu

² School of Civil and Environmental Engineering, Georgia Institute of Technology, Atlanta, GA, 30332, USA, E-mail: dominic.assimaki@ce.gatech.edu

Surface-to-borehole spectral ratio (SSR) analysis generally involves comparisons of strong and weak-motion responses based on the spectral ratio between a pair of co-located surface and borehole stations (Sawazaki et al., 2006, 2009; Wu et al., 2009). Here we apply a sliding-window SSR technique to track nonlinear behavior and temporal changes of the site response associated with the Mw6.6 2004 Mid-Niigata earthquake sequence in Japan. The Mid-Niigata earthquake is followed by a rigorous aftershock sequence with at least 3 with ~Mw6, which is ideal to quantify the effects of the input ground motion on the observed temporal changes. The seismic data is recorded at a site NIGH06 with surface and borehole instruments, which belongs to the Japanese Strong Motion Network KiK-Net. We use the spectral ratios between the surface and borehole stations to track temporal changes in the top 100 m of the upper crust. The observed peak spectral ratio decreases 40-60% and the peak frequency drops 30-70% immediately after earthquakes with PGV larger than ~5 cm/s. The co-seismic changes are followed by an apparent recovery with time scale ranging from several tens to more than one hundred of seconds. We find that the co-seismic peak frequency drop, peak spectral ratio drop, and the post-seismic recovery time roughly scale with the PGV. In comparison, no clear relationship is found between the measured temporal changes and the small PGV (i.e., < ~5 cm/s) or between apparent recovery speed and PGV.

Temporal changes of material properties within the surface soil layer induced by the strong ground motion of the large earthquakes are likely to be the main origin of the observed variations in the spectral ratios and

peak frequencies, because the seismic sources and the propagation path are almost identical for the co-located surface and borehole stations. Our results suggest that at a given site the input PGV plays an important role in controlling the degrees of nonlinearity and post-seismic recovery in site response. So far the mechanisms and controlling parameters for the time scale of recovery are still under investigation. Possible mechanisms include fluid diffusion and increasing contact area of crack surfaces or grains for sedimentary rocks.

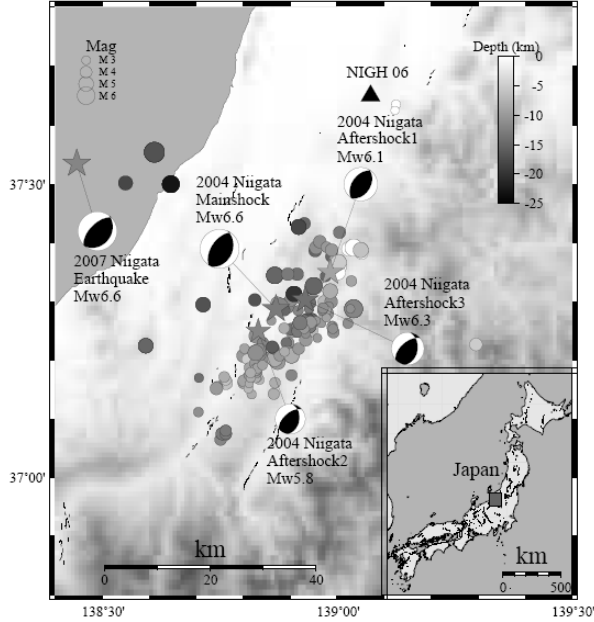


Figure 1. Topography map of the area along the west coast of Honshu, Japan. Shaded background indicates topography with white being low and dark being high. Epicenters of the 2004 Mw6.6 Mid-Niigata main shock, three large aftershocks, and the 2007 Mw6.6 Niigata-ken Chuetsu-oki earthquake are shown in stars together with their moment tensor solution. Other events are shown in circles. The size of circle indicates the magnitude of each event and gray scale shows the depth with white being shallow and dark being deep. Location of the KIK-Net station NIGH06 is shown in black triangle. Black dash lines show the faults in this region. The inset shows the map of Japan. The box indicates the region shown in the topography map.

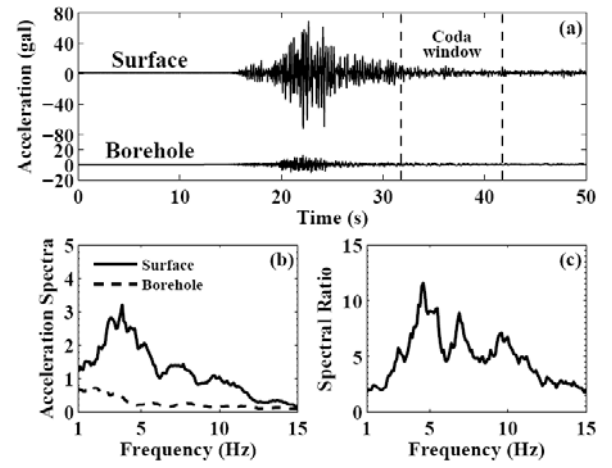


Figure 2. (a) East-component ground accelerations recorded at the station NIGH06 generated by an M5.2 earthquake on Nov 04, 2004. Surface recording is shown at the top and borehole recording is shown at the bottom. The dashed lines indicate the coda window that is used to compute the acceleration spectra in (b) and spectral ratio in (c).

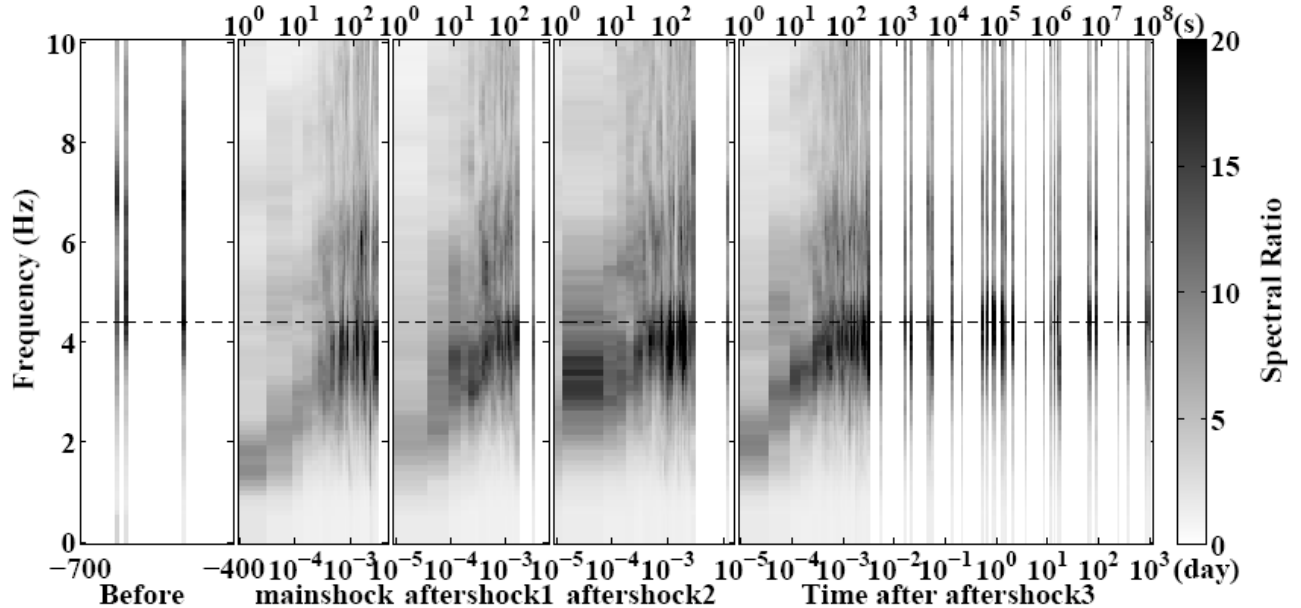


Figure 3. Temporal changes of spectral ratio at station NIGH06 during the 2004 Mid-Niigata earthquake sequence. The left bin shows gray-scale-coded spectral ratios for events before the main shock. The middle and right bins show those for the main shock and three aftershocks. Values shown on the top and bottom of the figure indicate lapse times after the main shock and large aftershocks in seconds and in days, respectively. Gaps represent no data. The horizontal black dashed line shows the pre-main shock value of peak frequency.

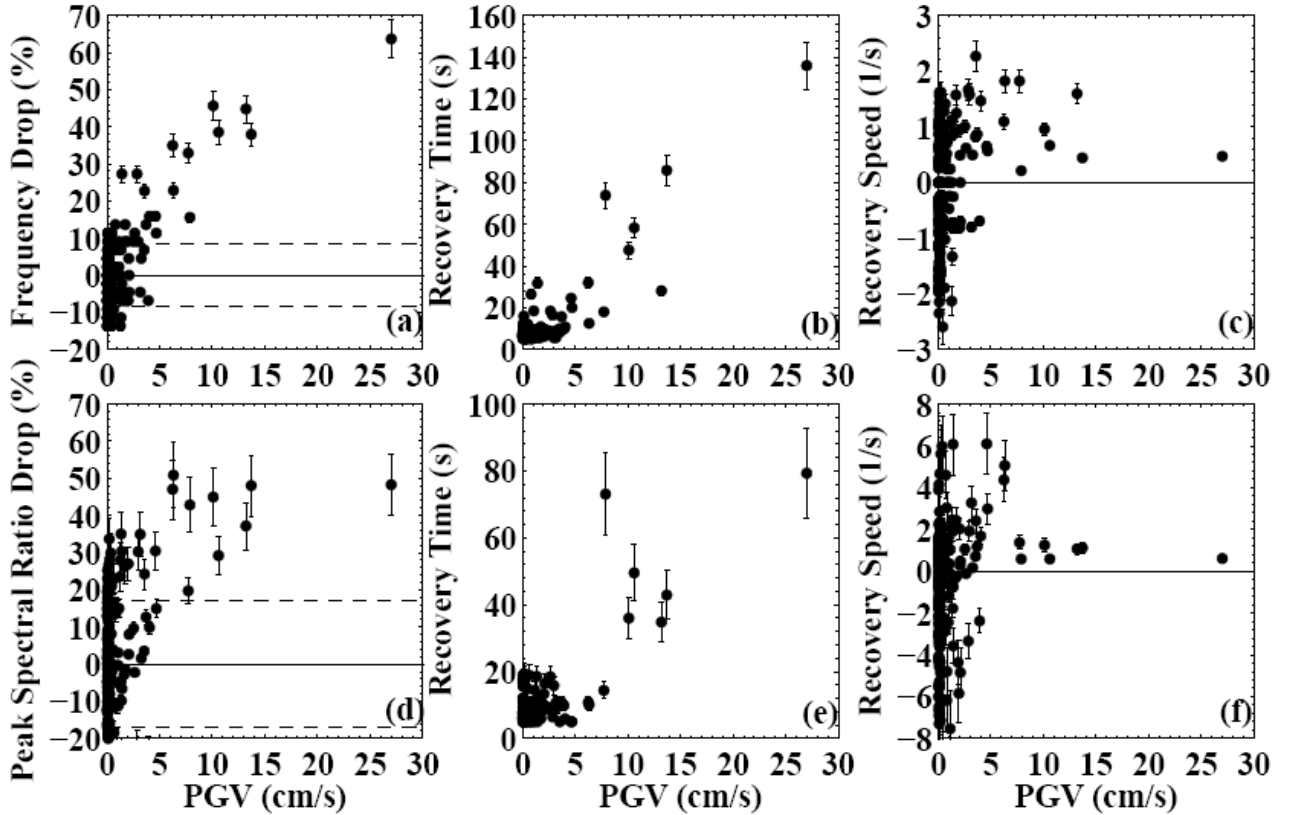


Figure 4. (a) Percentage drop of the peak frequency plotted against the peak ground velocity (PGV) at NIGH06 for all the 236 events. Vertical solid bar centered at each data point shows the standard deviation. The solid and dashed lines indicate the pre-shock value and standard deviation, respectively. (b) Recovery time to the reference peak frequency versus the PGV. (c) Apparent recovery speed of peak frequency versus the PGV. (d) Percentage drop of the peak spectral ratio versus the PGV. (e) Recovery time to the reference peak spectral ratio versus the PGV. (f) Apparent recovery speed of peak spectral ratio versus the PGV.

References

Sawazaki, K., H. Sato, H. Nakahara, and T. Nishimura, Temporal change in site response caused by earthquake strong motion as revealed from coda spectral ratio measurement, *Geophys. Res. Lett.* 33, no. 21, L21303, doi:21310.21029/22006GL027938, 2006.

Sawazaki, K., H. Sato, H. Nakahara, and T. Nishimura, Time-Lapse Changes of Seismic Velocity in the Shallow Ground Caused by

Strong Ground Motion Shock of the 2000 Western-Tottori Earthquake, Japan, as Revealed from Coda Deconvolution Analysis, *Bull. Seism. Soc. Am.* 99, no. 1, 352-366, 2009.

Wu, C., Z. Peng, and Y. Ben-Zion, Non-linearity and temporal changes of fault zone site response associated with strong ground motion, *Geophys. J. Int.* 176, no. 3, 265-278, 2009.

Energy Densities of Diffuse Seismic Fields as a Tool for Imaging

Francisco J. Sánchez-Sesma¹, Frank Scherbaum², Francisco Luzón³, Miguel A. Santoyo³, Antonio García-Jerez³, Alejandro Rodríguez-Castellanos⁴, Mathieu Perton¹, Michel Campillo⁵, and Richard L. Weaver⁶

¹ Instituto de Ingeniería, Universidad Nacional Autónoma de México, CU, Coyoacán 04510 DF, Mexico,

E-mail: sesma@servidor.unam.mx, Mathieu.Perton@imi.cnrc-nrc.gc.ca

² Institut fuer Geowissenschaften, Universitaet Potsdam, Potsdam, Germany,

E-mail: Frank.Scherbaum@geo.uni-potsdam.de

³ Departamento de Física Aplicada, Universidad de Almería, 04120 Almería, Spain,

E-mail: fluzon@ual.es, msantoyo@ual.es, agj574@ual.es

⁴ Instituto Mexicano del Petróleo, L. Cárdenas 152, 07730 DF, Mexico,

E-mail: arcastel@imp.mx

⁵ LGIT, Université J. Fourier, BP 53, 38041 Grenoble Cedex, France,

E-mail: Michel.Campillo@ujf-grenoble.fr

⁶ Department of Physics, University of Illinois, Urbana, Illinois 61801, USA,

E-mail: r-weaver@uiuc.edu

The coda or “tail” of seismograms is the late part of records and it is due to multiple scattering. Therefore, the intensities of waves composing the coda follow diffusive regimes. These late waves are similar to the noise in that they sample the medium and carry information along their paths. It is well known that for elastic inhomogeneous, or anisotropic medium under equipartitioned, isotropic illumination, the Green’s function can be retrieved from averaging cross correlations of recorded motions of such diffuse field (*e.g.* Campillo and Paul, 2003; Weaver and Lobkis, 2004; Wapenaar, 2004; Sánchez-Sesma and Campillo, 2006; Gouédard *et al.*, 2008).

The pioneering studies of Aki (1957) have contributed to the understanding of coda waves and seismic noise. Various scattering formulations have been developed in order to explain coda features (see Aki and Chouet, 1975; Sato and Fehler, 1998). When multiple scattering takes place the intensities (which are related to energy densities) follow diffusion-like equations. Due to

multiple scattering, coda waves arrive at a given site from different directions.

In this work we assume that source and receiver are both at the same point and explore the consequences. This is remarkable because from the observable side, the autocorrelation is proportional to the energy density at a given point. On the other hand, the imaginary part of the Green function at the source is finite because the singularity of the Green’s function is restricted to the real part. Thus, the energy density at a point is proportional to the trace of the imaginary part of Green’s function tensor at the source itself which is indeed such point. The relationships among energy densities and its partitions have been studied by Perton *et al.* (2009) and Margerin *et al* (2009). The Green’s function may be useful to imaging or inverting the subsurface structure at the site. In fact, the connection of the imaginary part of the Green’s function at the source with the optical theorem has been explored by Snieder *et al.* (2009). For horizontally layered systems this relationship for Green’s function was discovered by Claerbout (1968). His

formulation states the relationship between the transmission response and the reflection response for P waves in a horizontally layered medium and vertical incidence. Scherbaum (1987) developed an algorithm to identify reflection coefficients based upon Claerbout's results. This single station inversion method allows the imaging of the subsurface impedance structure. It was originally conceived to deal with locally recorded SH waves records.

Nowadays, the known relationship between energy densities and the imaginary part of the Green's function at the source allows us to generalize Scherbaum's (1987) results. From the normalized average autocorrelations, via Fourier inversion, pseudo-reflection seismograms, for the three components, can be obtained which in turn can be inverted for the impedance structure by exploiting Levinson recursion. For a horizontally layered medium the horizontal components should be equal. In reality the similitude of horizontal motions gives an indication of the flatness of the site.

Here we explore synthetic examples and assess the resolution of the technique. The limitations arise in the high-frequency content of the signals because of the combined effects of absorption, recording system, and signals band limit. In his original treatment, Scherbaum (1987) found that the influence of noise may drastically reduce the resolution of the inversion procedure. We expect that the normalized averages may reduce

significantly the unwanted noise. However, the absorption may remain as the most significant limiting factor.

In what follows, we review the Green's function retrieval from correlations of field fluctuations and study a simple model of an elastic layer with free surface overlaying a rigid basement and compute the imaginary part of the Green function when source and receiver are at the free surface. The resulting spectrum is indeed closely related to the layer dynamics because the corresponding resonant frequencies are revealed. On the other hand, the Fourier inversion the imaginary part of the Green function at the source leads to the pseudo-reflection seismograms and exhibits them as intrinsic site properties.

From these results two implications emerge: (1) the stabilization of the normalized average autocorrelation means that the resulting illumination is indeed equipartitioned, and thus (2) the resulting spectra and the pseudo-reflection seismograms can be regarded as the signatures of the site.

These results show that the seismic response of a site can be estimated even if strong ground motions are scarce. It suffices having reasonable complete illumination from micro earthquakes and noise. The imaginary part of Green's function at the source is *the* spectral signature of the site. The relative importance of the peaks of this energy spectrum, ruling out non linear effects, may control the seismic response for future earthquakes.

The Retrieval of the Green Function from Correlations

For the sake of establishing concepts we will proceed using a 2D formulation. The results apply for 1D and 3D as well. The corrections for dimensionality will be introduced in due time. It has been demonstrated (*e.g.* Sánchez-Sesma *et al.*, 2008) that if a 2D diffuse harmonic displacement vector field $u_i(\mathbf{x}, \omega)$ is

established within an elastic medium, the average cross-correlations of such motions at points \mathbf{x}_A and \mathbf{x}_B leads to the expression:

$$\langle u_i(\mathbf{x}_A, \omega) u_j^*(\mathbf{x}_B, \omega) \rangle = -4E_s k^2 \text{Im}[G_{ij}(\mathbf{x}_A, \mathbf{x}_B, \omega)]. \quad (1)$$

In this equation, the Green's function $G_{ij}(\mathbf{x}_A, \mathbf{x}_B, \omega)$ is the displacement at \mathbf{x}_A in direction i produced by a unit harmonic point force acting at \mathbf{x}_B in direction j , ω is the circular frequency, $k = \omega/\beta$ the shear wavenumber, β the shear wave propagation velocity, and $E_S = \rho\omega^2 S^2$ the average energy density of shear waves. Note that the asterisk

implies the complex conjugate and the angular brackets mean azimuthal average. Eq. 1 is the analytical consequence of a correlation-type elastic representation theorem and has been verified recently in canonical examples of a full space (Sánchez-Sesma and Campillo, 2006) and an elastic inclusion embedded in for various elastic cases (Sánchez-Sesma *et al.*, 2006; 2008).

Energy Densities at Given Points and Directions

In what follows we compute the total theoretical energy density at a given point

$$E(\mathbf{x}_A) = \rho\omega^2 \langle u_m(\mathbf{x}_A) u_m^*(\mathbf{x}_A) \rangle = -4\mu E_S \times \text{Im}[G_{mm}(\mathbf{x}_A, \mathbf{x}_A)] \quad (2)$$

The energy density of shear waves E_S is a measure of the strength of the diffuse illumination. We see that the total energy density at a point is proportional to the imaginary part of the trace of the Green tensor for coincident receiver and source. Note that this is possible because the singularity of Green's function is restricted to the real part. The imaginary part is finite and regular and represents the rate of energy injected by the unit

harmonic load at that point. This quantity "detects" the energy that goes back to the source-receiver and may be used to imaging. Equation 2 is valid even if the summation convention is ignored. In that case we write $E(\mathbf{x}_A) \equiv E_m(\mathbf{x}_A)$ and the energy density is associated to a particular direction (for discussions see Perton *et al.*, 2009 and Snieder *et al.*, 2009).

The 2D Half-Space. Antiplane SH Problem

Consider the anti-plane SH case and a half-space. The Green's function can be

$$G_{22}(\mathbf{x}_A, \mathbf{x}_B) = \frac{1}{4i\mu} \left\{ H_0^{(2)}(kr) + H_0^{(2)}(kr') \right\}, \quad (3)$$

where μ = shear modulus, $H_0^{(2)}(\cdot)$ = cylindrical Hankel function of the second kind and zero order defined by $J_0(\cdot) - iY_0(\cdot)$, where $J_0(\cdot)$ and $Y_0(\cdot)$ are the Bessel functions of the first and

obtained superimposing the mirror image of the reflection. Thus we have

second kinds and zero order. Moreover, r = distance source-receiver and r' = distance image-receiver. Therefore, the imaginary part of the Green function is given by

$$\text{Im}[G_{22}(\mathbf{x}_A, \mathbf{x}_B)] = \frac{-1}{4\mu} (J_0(kr) + J_0(kr')). \quad (4)$$

At the source $r = 0$ and $r' = 2z$. According to Eq. 3 the energy density is proportional to the imaginary part of the Green's function at the source. As we

This expression gives the SH energy density as a function of both frequency and distance to the free surface. At the surface the energy density is constant and twice the value of the infinite space.

have only SH waves, $E_\infty = E_S$. Moreover, $J_0(0) = 1$: we can write

$$E(z, \omega) = E_\infty \times (1 + J_0(2kz)). \quad (5)$$

In Fig. 1 we depict the ratio $E(kz)/E_\infty$ against kz , a normalized depth because $k = 2\pi/\Lambda$ with Λ = wavelength of shear waves.

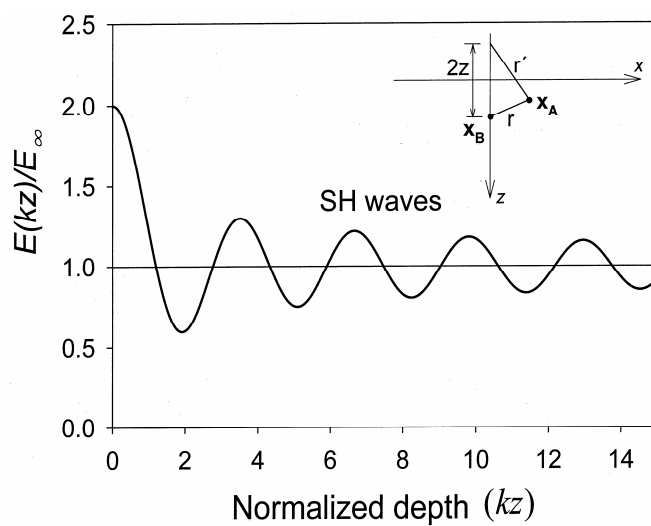


Fig. 1 Normalized energy density for a diffuse SH wave field in a 2D half-space.

This result shows that for a SH diffuse field in 2D the energy density at the surface is twice the reference level (E_∞).

The ratio depicted in Fig. 1 reveals fluctuations that depend from with depth and frequency.

The Antiplane Layer

Consider a layer of thickness h and free boundary conditions at the top with a rigid base (see Fig. 2).

The 2D Green's function for this problem can be computed using the method of

images, as in the half-space, but now including the contributions of all the reflections (note the phase change of reflections from rigid bottom). Therefore, we can write

$$\text{Im}[G(0,0)] = \{1 - 2J_0(\omega\tau) + 2J_0(2\omega\tau) - 2J_0(3\omega\tau) + \dots\}/2, \quad (6)$$

where $\tau = 2h/\beta$ = travel time source-reflector-source. The series within brackets has a sum in terms of a series of

reciprocal square roots (see Gradshteyn and Ryzhik, 1994). Thus, we have

$$\text{Im}[G(0,0)] = (\pi\tau)^{-1} \sum_{n=1}^{\infty} \frac{H(f - (2n-1)/2\tau)}{\sqrt{f^2 - ((2n-1)/2\tau)^2}}. \quad (7)$$

In Fig. 3 the first five peaks can be seen at the resonant frequencies $(2n-1)/2\tau$ of the 2D free-fixed layer. It is also clear

that the frequency $1/2\tau$ is a cut-off frequency. In order to consider a damped medium $Q = 50$ we used the expression

$$\text{Im}[G(0,0)] = \text{Re}\{H_0^{(1)}(0) - 2H_0^{(1)}(\omega\tau) + 2H_0^{(1)}(2\omega\tau) - 2H_0^{(1)}(3\omega\tau) + \dots\}/2 \quad (8)$$

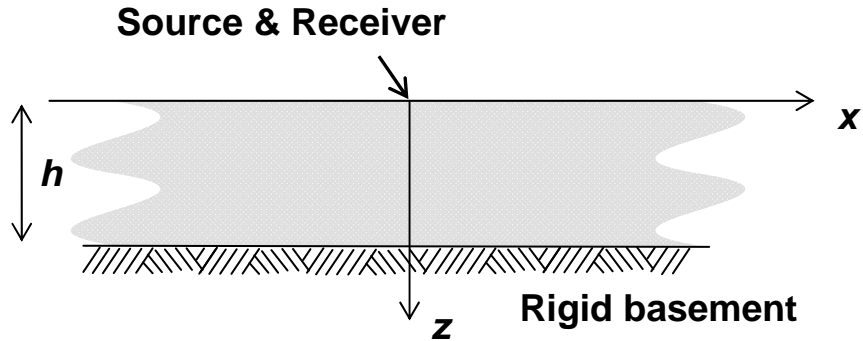


Figure 2. Layer with rigid basement.

and let the shear wave velocity be complex. That means $\beta = \beta_0(1+i/2Q)$ with β_0 = reference value and then

$\tau = 2h/\beta$ is allowed to be complex. The damped case was computed with Eqn. 8 using 50 terms.

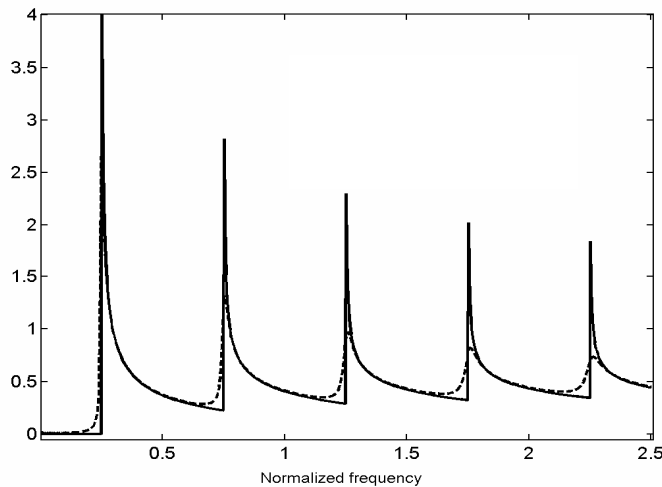


Figure 3. $\text{Im}[G(0,0)]$ against normalized frequency $f\tau$, with $\tau = 2$ sec, for a 2D layer with free-fixed boundary conditions. Solid line, $Q^1=0$, no damping. Dashed line, $Q = 50$.

Pseudo-Reflection Seismograms for the Layer

It is possible to show that the Fourier inversion of Eq. 7, namely the inversion of $i \operatorname{sgn} \omega \times \operatorname{Im}[G(0,0;\omega)]$, leads to the non

$$\frac{1}{\pi\mu} \sum_{n=0}^{\infty} \varepsilon_n (-1)^n \frac{H(t - n\tau)}{\sqrt{t^2 - (n\tau)^2}}, \quad (9)$$

where ε_n = Neumann factor ($=1$ if $n=0$; $=2$ for $n>0$). This result exhibits a remarkable

causal signal. The causal part, however, is the pseudo-reflection seismogram which in our example is:

isomorphism of both the frequency and time responses.

Conclusions

From the fact that the imaginary part of the Green's function at the source is proportional to the average energy density we propose that the Green's function at a given point (assuming source and receiver to be the same) is the theoretical energy density of a diffuse field generated by a background excitation.

We studied the cases of a half space and a simple layer model under antiplane excitation and compute the imaginary part of the Green functions at the source in each case. For the layer, the theoretical energy densities display the effect of the reflector of the lower boundary. The peaks reveal the resonant frequencies of the system.

The imaginary part of the Green's function at the source is then *the* spectral signature of the site. The relative

importance of the peaks of this energy spectrum, ruling out non linear effects, may control the seismic response for future earthquakes. This finding may be useful seismic zonation.

For the simplest case, namely the horizontally layered medium, the identity of energy density and the Green function at the source allows imaging the structure of the site using the approach by Scherbaum (1987) from inverted pseudo-reflection seismograms.

Theoretically, the energy densities allows for imaging under more general conditions. In fact, the connection with the optical theorem has been explored by Snieder *et al.* (2009). The full imaging of a site to detect underground features will require the analysis of spatial variations and further scrutiny.

Acknowledgements

Thanks are given to Roel Snieder and Kees Wapenaar for enlightening discussions. Partial supports from DGAPA-UNAM, Project IN121709, Mexico; from Project MCIN CGL2008-

06426-C02-02/BTE, Spain; from Project DyETI of INSU-CNRS, France, and from Instituto Mexicano del Petróleo are greatly appreciated.

References

- Aki K. (1957). Space and time spectra of stationary stochastic waves with special reference to microtremors, *Bull. Earthq. Res. Inst.* **35**, 415-456.
- Aki K. & Chouet B. (1975). Origin of coda waves: Source, attenuation and scattering effects, *J. Geophys. Res.* **80**, 3322-3342.
- Campillo M. & Paul A. (2003). Long range correlations in the seismic coda, *Science* **299**, 547-549.
- Claerbout J. F. (1968). Synthesis of a layered medium from its acoustic transmission response, *Geophysics* **33**, 264-269.
- Gouédard P., Stehly L., Brenguier F., Campillo M., Colin de Verdiére Y., Larose E., Margerin L., Roux P., Sánchez-Sesma F. J., Shapiro N. M. & Weaver R. L. (2008). Cross-correlation of random fields: mathematical approach and applications, *Geophys. Prospecting* **56**, 375-393.
- Gradsshteyn I. S. & Ryzhik I. M. (1994). *Table of Integrals, Series and Products Fifth Edition*, Academic Press, London.
- Margerin L., Campillo M., van Tiggelen B. A. & Hennino R. (2009). Energy partition of seismic coda waves in layered media: theory and application to Pinyon Flats Observatory, *Geophys. J. Int.* **177**, 571-585.
- Perton M., Sánchez-Sesma F.J., Rodríguez-Castellanos A., Campillo M. & Weaver R.L. (2009). Two perspectives on equipartition in diffuse elastic fields in three dimensions, *J. Acoust. Soc. Am.*, submitted.
- Sánchez-Sesma F. J. & Campillo M. (2006). Retrieval of the Green function from cross-correlation: The canonical elastic problem, *Bull. Seism. Soc. Am.* **96**, 1182-1191.
- Sánchez-Sesma F. J., Pérez-Ruiz J. A., Campillo M. & Luzón F. (2006). The elastodynamic 2D Green function retrieval from cross-correlation: The canonical inclusion problem, *Geophys. Res. Lett.* **33**, L13305, doi:10.1029/2006GL026454.
- Sánchez-Sesma F. J., Pérez-Ruiz J. A., Luzón F., Campillo M. & Rodríguez-Castellanos A. (2008). Diffuse fields in dynamic elasticity, *Wave Motion* **45**, 641-654.
- Sato H. & Fehler M. (1998). *Wave Propagation and Scattering in the heterogeneous Earth*, Springer-Verlag, New York.
- Scherbaum F. (1987). Seismic imaging of the site response using microearthquake recordings. Part 1. Method, *Bull. Seism. Soc. Am.* **77**, 1905-1923.
- Snieder R., Sánchez-Sesma F. J. & Wapenaar K. (2009). Field fluctuations, imaging with backscattered waves, a generalized energy theorem, and the optical theorem, *SIAM J. Imaging Sciences*, in press.
- Wapenaar K. (2004). Retrieving the elastodynamic Green's function of an arbitrary inhomogeneous medium by cross correlation, *Phys. Rev. Lett.* **93**, 254301-1-4.
- Weaver R. L. & Lobkis O.I. (2004). Diffuse fields in open systems and the emergence of the Green's function, *J. Acoust. Soc. Am.* **116**, 2731-2734.

Comparing Interferometric Migration and Mirror Imaging of 3D-VSP Free-Surface Multiples

Hugues Djikpesse¹, Shuqian Dong², Jakob Haldorsen¹, Douglas Miller¹

¹ Schlumberger-Doll Research, 1 Hampshire street, Cambridge, MA 02139, USA, E-mail: HDjikpesse@slb.com

² University of Utah, Department of Geology and Geophysics, 719 WBB, 135 South, 1460 East, Salt Lake City, UT 84112, USA

Introduction

The classical way of imaging the subsurface from VSP data consists of migrating or inverting deconvolved up-going reflections (e.g., Miller, et al., 1984, 1987; Dupal and Miller, 1985; Payne, 1994; Haldorsen, et al., 1994, 1995; Djikpesse and Barnes, 2000; and Djikpesse et al., 2006). While benefitting from reduced attenuation and improved velocity control with respect to migrated surface data, the resulting migrated VSP images are restricted to a relatively narrow illuminated aperture lying below the borehole receivers. Downgoing signal, including signal scattered from the free surface, is, in the classical approach, not used for imaging.

In recent years, significant progress has been made in the use of seismic interferometry (SI) to enable subsurface imaging with signals previously considered as noise. This is typically achieved by a redatuming process in which new seismic responses corresponding to virtual sources or receivers are constructed by crosscorrelating seismic observations either recorded at different locations or carrying complementary information (e.g., Schuster, 2001; Wapenaar et al., 2002; Curtis, et al., 2006). Wapenaar, Draganov, and Robertsson (2006, as editors of a dedicated supplement of *Geophysics*) and Schuster (2009) provided two excellent reviews on the state of the art in the field of seismic interferometry, its theory, and applications.

One such application of interferometry has been to VSP-multiple interferometric migration (e.g., Jiang et al., 2005; Yu and Schuster, 2006). This procedure creates virtual common midpoint gathers as if the

sources and receivers were located at the surface. This virtual surface data has a zone of illumination that extends to the surface and is wider than that of the singly scattered VSP data. While these methods are now becoming a more common practice in the industry, SI still suffers from two major limitations: (1) a high computational cost associated with calculating the crosscorrelograms and (2) a significant difficulty tracking and correcting the amplitudes of the redatumed seismograms when they are compared to the ones that would be collected with true receivers at the surface.

Mirror imaging is an alternative way to use free-surface reflections in VSP data. It dated from the end of the eighties (e.g., Hu and McMechan, 1986, Wapenaar et al., 1987, Alam, 1988) and has recently gained new attention (e.g., Lou et al., 2007, Jiang et al., 2007). Here, one simply makes use of the virtual receivers created by the free surface mirror. Because the mirror receivers lie in a mirrored medium above the free-surface, the mirrored experiment has a zone of illumination that extends to the surface.

In this note, we compare mirror-imaging and interferometric migration methods using synthetic examples.

Free-Surface Acoustic Media Boundary

Consider an acoustic 3-D subsurface model characterized, at any location \mathbf{x} , (i.e., $\mathbf{x} = (x, y, z) \in \mathbf{R}^3$), by two acoustic parameters such as bulk modulus $[k(\mathbf{x})]$ and density $[p(\mathbf{x})]$. The two acoustic parameters are assumed invariant with respect to time t (or frequency ω). Given a pressure source

field $S(\mathbf{x}, t)$, the acoustic pressure inside the subsurface model can be described by the acoustic wave equation:

$$\left[\frac{1}{\kappa(\mathbf{x})} \frac{\partial^2}{\partial t^2} - \frac{1}{\rho(\mathbf{x})} \Delta \right] p(\mathbf{x}, t) = S(\mathbf{x}, t). \quad (1)$$

The solution to Eq. 1 can be stated in terms of Green's function as

$$p(\mathbf{x}, t) = \int_V dx' \int_T dt' G(\mathbf{x}, t; \mathbf{x}', t') S(\mathbf{x}', t'), \quad (2)$$

where the Green's function $G(\mathbf{x}, t; \mathbf{x}', t')$ represents the solution to the wave equation with a temporal Dirac source emitted at time t' and at single point location \mathbf{x}' . It thus satisfies

$$\begin{aligned} & \frac{1}{\kappa(\mathbf{x})} \frac{\partial^2 G(\mathbf{x}, t; \mathbf{x}', t')}{\partial t^2} - \\ & \frac{\partial}{\partial x^j} \left[\frac{1}{\rho(\mathbf{x})} \frac{\partial G(\mathbf{x}, t; \mathbf{x}', t')}{\partial x^i} \right] \\ & = \delta(t - t') \delta(\mathbf{x} - \mathbf{x}'). \end{aligned} \quad (3)$$

In seismic experiments, sources and receivers are typically considered located at single points. The forward problem of relating the recorded data to the subsurface model parameters for a given acquisition geometry of sources and receivers can be solved by evaluating Eq. 2 at receiver positions. For a given receiver location \mathbf{x}_r , the seismogram that would be recorded due to a temporal source function $S(t)$ emitted from location \mathbf{x}_s , can be modeled, given that $S(\mathbf{x}', t') = S(t') \delta(\mathbf{x}_s - \mathbf{x}')$, as

$$p(\mathbf{x}_s, \mathbf{x}_r, t) = \int_T dt' G(\mathbf{x}_r, t; \mathbf{x}_s, t') S(t'). \quad (4)$$

The formalism laid out by Eqs. 1 to 4 applies to an unbounded medium. When we wish to consider a medium bounded above by a flat, pressure-free boundary, we restrict the domain of definition to the lower half-space $\mathbf{R}_-^3 = \{(x, y, z) : z \leq 0\}$ and add the boundary condition (valid for all x, y, t, \mathbf{x}', t'):

$$G((x, y, 0), t; \mathbf{x}', t') = 0. \quad (5)$$

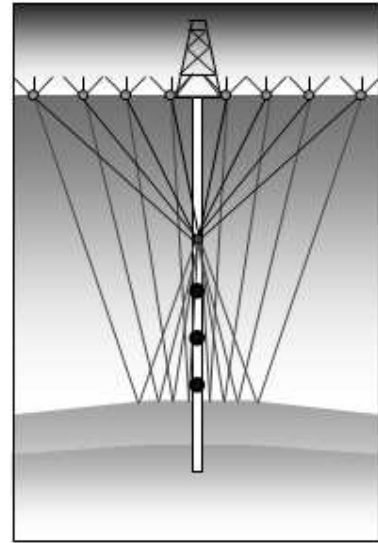


Figure 1. A simple VSP walkaway experiment illustrating the different components of the total recorded wave fields.

The Green's function for the bounded medium is related to the Green's function of a corresponding symmetric unbounded medium by the following well-known result:

Let \mathbf{M} be an acoustic medium defined in \mathbf{R}_-^3 and let $\bar{\mathbf{M}}$ be the symmetric medium obtained by reflecting \mathbf{M} in the plane $\{\mathbf{x} : z = 0\}$. Suppose $G(\mathbf{x}, t; \mathbf{x}', t')$ is the Green's function for $\bar{\mathbf{M}}$ (i.e., satisfying Eq. 3 everywhere). Let

$$\begin{aligned} \bar{G}((x, y, z), t; \mathbf{x}', t') = \\ G((x, y, z), t; \mathbf{x}', t') - G((x, y, -z), t; \mathbf{x}', t'), \end{aligned} \quad (6)$$

then the restriction of \bar{G} to $\mathbf{R}_-^3 \times \mathbf{R}$ is the Green's function for \mathbf{M} (i.e., satisfying Eqs. 3 and 5).

Note that, if \mathbf{M} is defined by material parameters $\mathbf{m}(\mathbf{x}) = (\kappa(\mathbf{x}), \rho(\mathbf{x}))$, then $\bar{\mathbf{M}}$ has material parameters $\bar{\mathbf{m}}$ satisfying $\bar{\mathbf{m}}(x, y, z) = \mathbf{m}(x, y, -|z|)$. Note also that

$$\bar{G}((x, y, z), t; \mathbf{x}', t') = -\bar{G}((x, y, -z), t; \mathbf{x}', t'). \quad (7)$$

We will refer to \bar{G} as the antisymmetric Green's function. It solves the acoustic wave equation in the symmetric medium for arbitrary antisymmetric sources and wave fields.

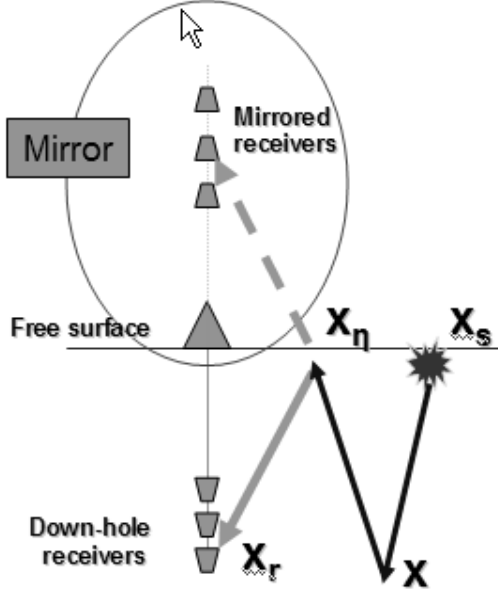


Figure 2. Mirror imaging principle in the case of offset VSP acquisition. It is the mirror image of the receivers, relative to the flat free surface, that gives the extra aperture. This also produces an image of the formation between the physical sources and the physical receivers with the proper amplitudes.

Interferometric VSP Migration

For illustration, consider a walkaway VSP experiment as shown in Figure 1. A set of seismic sources are located at the surface at \mathbf{x}_s , while seismic waveforms are recorded at varying depths \mathbf{x}_r using downhole receivers located in a wellbore. The recorded seismograms include direct waves, primary reflected waves, and multiply reflected waves. According to what is commonly referred to as the weak-scattering approximation, the recorded field $p(\mathbf{x}_s, \mathbf{x}_r, \omega)$ (after a Fourier transform) described by Eq. 4 is considered to be dominated by a direct field

$$p_0(\mathbf{x}_s, \mathbf{x}_r, \omega) = G(\mathbf{x}_s, \mathbf{x}_r, \omega)S(\omega), \quad (8)$$

and a singly scattered field

$$\begin{aligned} p_1(\mathbf{x}_s, \mathbf{x}_r, \omega) &= \int d\mathbf{x} G(\mathbf{x}_s, \mathbf{x}, \omega)O(\mathbf{x}, \omega) \\ &\quad G(\mathbf{x}, \mathbf{x}_r, \omega)S(\omega), \end{aligned} \quad (9)$$

Where $O(\mathbf{x}, \omega)$ is ω^2 times the scattering potential at a point \mathbf{x} in the formation. Within this approximation, and in analogy to Miller, et al. (1987, Eq. 8), the total field is written:

$$\begin{aligned} p(\mathbf{x}_s, \mathbf{x}_r, \omega) &= p_0(\mathbf{x}_s, \mathbf{x}_r, \omega) + \\ &\quad p_1(\mathbf{x}_s, \mathbf{x}_r, \omega) + \dots \\ &\approx G(\mathbf{x}_s, \mathbf{x}_r, \omega)S(\omega) \\ &\quad + \int G(\mathbf{x}_s, \mathbf{x}, \omega)O(\mathbf{x}, \omega) \\ &\quad G(\mathbf{x}, \mathbf{x}_r, \omega)S(\omega)d\mathbf{x}, \end{aligned} \quad (10)$$

where the Green's function $G(\mathbf{x}_2, \mathbf{x}_1, \omega)$, also often referred to as the "wave-field propagator" for the medium, describes the propagation of a wave field from point \mathbf{x}_1 to point \mathbf{x}_2 . The "... represent additional components of the wave field with more complicated ray paths.

By writing

$$G(\mathbf{x}_2, \mathbf{x}_1) = A(\mathbf{x}_2, \mathbf{x}_1) e^{i\omega\tau(\mathbf{x}_2, \mathbf{x}_1)}, \quad (11)$$

one may separate the phase and amplitude parts of the Green's function. Here and in most of the following, we are omitting the argument ω in G , A , O , and in the different components of the wavefield data p .

In addition to the direct and singly scattered wave fields specified in Eq. 10, a portion of the energy will, after having been scattered from the medium inhomogeneities, reach the free surface where it is reflected and later recorded by the downhole receiver at \mathbf{x}_r .

Denoting the free-surface reflection point by \mathbf{x}_η , we have

$$\begin{aligned} p_2(\mathbf{x}_s, \mathbf{x}_r; \mathbf{x}, \mathbf{x}_\eta) &= A(\mathbf{x}_r, \mathbf{x}_\eta)A(\mathbf{x}_\eta, \mathbf{x})O(\mathbf{x}) \\ &\quad A(\mathbf{x}, \mathbf{x}_s)S(\omega) \\ &\quad e^{i\omega[\tau(\mathbf{x}_r, \mathbf{x}_\eta) + \tau(\mathbf{x}_\eta, \mathbf{x}) + \tau(\mathbf{x}, \mathbf{x}_s)]}, \end{aligned} \quad (12)$$

and may rewrite the total wave field as:

$$\begin{aligned} p(\mathbf{x}_s, \mathbf{x}_r) &= p_0(\mathbf{x}_s, \mathbf{x}_r) + \int d\mathbf{x} p_1(\mathbf{x}_s, \mathbf{x}_r; \mathbf{x}) \\ &\quad + \int d\mathbf{x}_\eta \int d\mathbf{x} p_2(\mathbf{x}_s, \mathbf{x}_r; \mathbf{x}, \mathbf{x}_\eta) + \dots \end{aligned}$$

$$\begin{aligned} &\approx A(\mathbf{x}_r, \mathbf{x}_s)S(\omega)e^{i\omega\tau(\mathbf{x}_r, \mathbf{x}_s)} \\ &\quad + \int d\mathbf{x} A(\mathbf{x}_r, \mathbf{x})O(\mathbf{x})A(\mathbf{x}, \mathbf{x}_s) \\ &\quad S(\omega)e^{i\omega[\tau(\mathbf{x}_r, \mathbf{x}) + \tau(\mathbf{x}, \mathbf{x}_s)]} \\ &\quad + \int d\mathbf{x}_\eta \int d\mathbf{x} A(\mathbf{x}_r, \mathbf{x}_\eta)A(\mathbf{x}_\eta, \mathbf{x}) \\ &\quad O(\mathbf{x})A(\mathbf{x}, \mathbf{x}_s)S(\omega) \\ &\quad e^{i\omega[\tau(\mathbf{x}_r, \mathbf{x}_\eta) + \tau(\mathbf{x}_\eta, \mathbf{x}) + \tau(\mathbf{x}, \mathbf{x}_s)]}. \end{aligned} \quad (13)$$

In typical processing of VSP data, only primary reflections are considered. Preprocessing typically includes steps to decompose the received signal as a sum of upgoing and downgoing signal at the receiver array and to design a deconvolution operator based on the extracted downgoing signal. In this process, multiple reflections are regarded as noise and attempts are being made to eliminate them. However, free-surface-related multiples contain valuable information about the subsurface structures, and if they are properly migrated, they can provide wider illumination of the subsurface properties than when imaging using primaries only. Seismic interferometric migration is a method recently developed to create migrated images from VSP data after transforming the recorded raw data into wider-aperture virtual surface data using previously neglected multiple reflections (e.g., Jiang et al., 2005; Yu and Schuster, 2006).

Data generated by sources located at the surface at \mathbf{x}_s and recorded by receivers located at the surface at \mathbf{x}_η can be written as:

$$p(\mathbf{x}_s, \mathbf{x}_\eta) = S(\omega) \int d\mathbf{x} A(\mathbf{x}_\eta, \mathbf{x}) O(\mathbf{x}) A(\mathbf{x}, \mathbf{x}_s) e^{i\omega[\tau(\mathbf{x}_\eta, \mathbf{x}) + \tau(\mathbf{x}, \mathbf{x}_s)]} + \dots \quad (14)$$

Several authors, including Jiang et al. (2005) and Yu and Schuster (2006), suggest transforming the VSP data to an "equivalent" surface-seismic data set correlating all shot files and summing over the borehole receivers (their Eqs. 2 and 5 reworded here in terms of the walkaway VSP geometry of Figure 1):

$$\Phi(\mathbf{x}_s, \mathbf{x}_\eta, t) = \int d\mathbf{x}_r p(\mathbf{x}_s, \mathbf{x}_r, t) \otimes p(\mathbf{x}_\eta, \mathbf{x}_r, t), \quad (15)$$

where \mathbf{x}_s and \mathbf{x}_η are source positions on the surface and the integral is taken over receiver positions in the borehole.

Despite successful field applications, this correlation technique suffers from two major limitations: (1) the expensive computation cost required to construct the crosscorrelograms, and (2) the fact that

although the predicted travel times of the redatumed data seem well approximated, their waveforms may be significantly distorted due to their incorrect amplitude spectra. In particular, when sources are not pure impulses, correlation techniques generally repair the phase of the signal, but magnify any irregularities in the source amplitude spectrum.

Yu and Schuster (2006) observed that if one separates the wavefield $p(\mathbf{x}_s, \mathbf{x}_r)$ from Eq. 13 into upgoing and downgoing fields; separate the direct field, $p_0(\mathbf{x}_s, \mathbf{x}_r, \omega)$, Eq. 8, from the total downgoing field; and finally shift the residual downgoing field by the measured travel time $\tau(\mathbf{x}_r, \mathbf{x}_\eta')$ from any point \mathbf{x}_η' on the surface to a receiver at \mathbf{x}_r , one is left with

$$p(\mathbf{x}_s, \mathbf{x}_r; \mathbf{x}_\eta') = \int d\mathbf{x}_\eta \int d\mathbf{x} A(\mathbf{x}_r, \mathbf{x}_\eta) A(\mathbf{x}_\eta, \mathbf{x}) O(\mathbf{x}) A(\mathbf{x}, \mathbf{x}_s) S(\omega) e^{i\omega[\tau(\mathbf{x}_r, \mathbf{x}_\eta) - \tau(\mathbf{x}_r, \mathbf{x}_\eta') + \tau(\mathbf{x}_\eta, \mathbf{x}) + \tau(\mathbf{x}, \mathbf{x}_s)]} + \dots$$

Although the specular free-surface reflection points \mathbf{x}_η are not known, following the principle of stationary phase, an approximation can be found by stacking over the array of downhole receivers:

$$p(\mathbf{x}_s, \mathbf{x}_\eta') \approx \sum_{r=1}^{N_r} p(\mathbf{x}_s, \mathbf{x}_r; \mathbf{x}_\eta'). \quad (16)$$

Yu and Schuster (2006) refer to this method as "specular interferometry". It improves computational performance, gets the travel times correct, and gives a more desirable "effective source signature," but nevertheless leaves an extra term $A(\mathbf{x}_r, \mathbf{x}_\eta)$, the transmission response between physical locations of the source and receivers, in the effective-source term.

Mirror Imaging of VSP multiples

From Eq. 7, we have $\tilde{G}((x, y, z), t; \mathbf{x}', t') = -\tilde{G}((x, y, -z), t; \mathbf{x}', t')$. It follows that data recorded in an experiment performed with monopole sources in a medium bounded by a free surface can be

viewed as the result of an equivalent experiment performed in a symmetric, unbounded medium performed with paired, antisymmetric sources. The presence of the ghost source, a virtual source whose time signature is minus one times the actual signature, is a well-known problem for imaging in general. The use of free surface multiples can be viewed either as a problem of using the recorded data to image the upper half of the unbounded symmetric medium or as a problem of imaging the lower half of the unbounded medium using ghost receivers whose locations are symmetric to the actual receiver locations, and whose data is the recorded data multiplied by -1 . Thus, the data can be processed by the simple steps:

- 1) Replace receiver locations (x_r^i, y_r^i, z_r^i) with their ghost locations $(x_r^i, y_r^i, -z_r^i)$.
- 2) Replace receiver data $p(\mathbf{x}_r, t)$ with ghost data $p((x_r^i, y_r^i, -z_r^i), t) = -p(\mathbf{x}_r, t)$.
- 3) Proceed with your favorite algorithm for deconvolution and imaging with VSP data.

The principle of mirror imaging in the case of an offset VSP is illustrated in Figure 2. The free surface is replaced by a medium and an acquisition geometry that is symmetric about the free surface. It is the mirror image of the receivers, relative to the flat free surface, that gives the extra image aperture. In addition, and with the redatuming approach discussed in the previous section, one also gets an image of the formation between the physical sources and the physical receivers with the proper amplitudes.

Note that free-surface-related multiples become the reflections from sources to the mirrored receivers. No extra computation for redatuming is involved. Furthermore, the problem of correctly treating amplitudes, prefilters, angular weighting, etc. is exactly as it was for the original problem, using physical, rather than virtual, sources and receivers. The use of mirror imaging does not solve the problem of imaging with an antisymmetric finite dipole source, but it clarifies the nature of this problem which was present in any case.

Note also that the method is applicable to single or multiple offset VSP data where the sources are not necessarily finely sampled spatially. There are issues regarding proper balancing of contributions from the various sources, but they are the same issues that occur in migrating the primaries.

Numerical Example

A 2D acoustic synthetic data set was created using the model and geometry shown in Figure 3, using 101 point sources at 20 m intervals from -1000 m to 1000 m, 2.5 m below the free surface, and 1301 pressure-sensitive receivers at 2.5 m interval from 2.5 m below the free surface to a depth of 1300 m. The vertical borehole was located at $x=0$. Figure 4 shows a sample common shot gather. The source was given by a 40 Hz Ricker wavelet.

Yu and Schuster (2006) suggest imaging the data using a prestack Kirchhoff surface seismic migration operator. Instead of this, we have used an algorithm based on the Generalized Radon Transforms (GRT, according to Miller, et al., 1987), which essentially uses Eq. 16 with appropriate weighting terms in the integrand. We processed the data in a number of different ways:

- 1) Conventional VSP migration,
- 2) Using Eq. 15,
- 3) Using Eq. 16,
- 4) Using the algorithm for mirror imaging outlined in the previous section.

For the images discussed next, we have used a depth sampling of 25 m for the geophones along the wellbore (every 10th level from the raw synthetics exemplified by Figure 4), and 20 m along the surface. Figure 5 shows the image obtained by conventional VSP migration of the raw total data files. The image shows quite apparent artifacts related to the coarse depth sampling. Figure 6 compares images resulting from applying the imaging algorithm described by Yu and Schuster (2006) to the mirror-imaging algorithm.

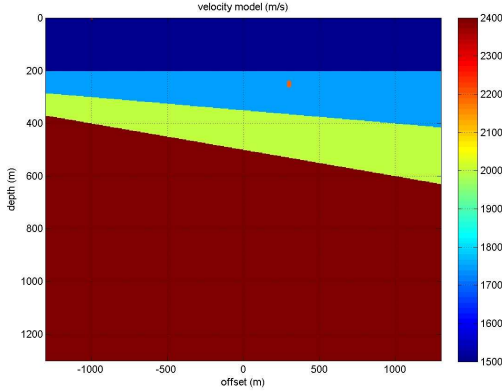


Figure 3. A simple acoustic model made of a set of dipping layers below the sea floor. The sea floor is at a depth of 200 m, about 50 m below which is a buried point scatterer.

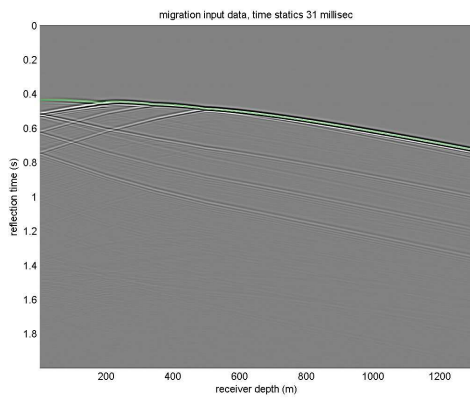


Figure 4. Sample of raw data generated over the simple model shown in Figure 3, with the source at about 500 m, 2.5 m below the free surface, and receivers every 2.5 m from the free surface to a depth of 1300 m.

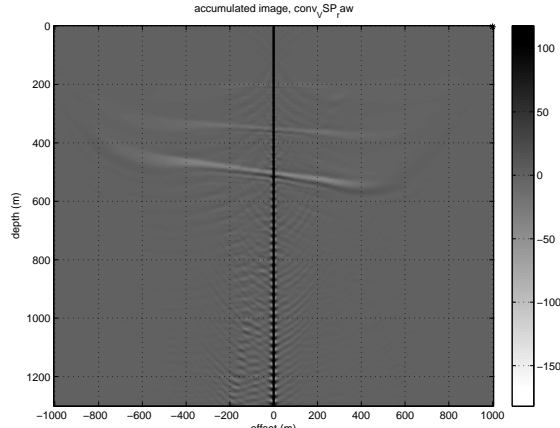


Figure 5. Comparison of images obtained from the raw synthetics exemplified by the data displayed in Figure 4, using conventional VSP migration.

We have applied the processes to the separated downgoing wavefield (as recommended by Yu and Schuster, 2006). For all images, we used 2D ray tracing through the exact velocity model, and a maximum $\pm 45^\circ$ reflector dip angle. The "mirrored image" is very similar to the two corresponding versions of the interferometric image. Of the two interferometric images, the simplest, straightforward, correlation and stacking image (Eq. 15) may have marginally fewer artifacts.

Either method provides an image of the structures between the sources and receivers. Whereas the processing for the two interferometric images are about the same, the mirrored image was generated in about one-half the time. All images show artifacts associated with higher-order multiples.

Conclusions and open questions

We have compared, using a synthetic model, interferometric migration to mirror-imaging of VSP multiples. Both methods give practically identical coverage of the subsurface. Because the steps of correlation and summation are avoided, the mirrored experiment is computationally trivial to create. Moreover, it has the same possibility for careful balancing of terms in the inversion integral as is afforded by a singly scattered experiment.

However, because mirror-imaging assumes virtual receivers set relatively to a flat free surface and requires wave propagation in the medium between the surface and the downhole receivers, it may suffer from limitations due to non-planar free surface and sensitivity to the errors in the velocity model (above the receivers).

References

- Alam, A. M., 1988, Method for extending the lateral subsurface coverage in vertical seismic profiling surveys: European Patent, EP 0 317 288 B1, submitted 16.11.88, issued 28.04.93
- Curtis, A. P., Gerstoft, H. Sato, R. Snieder and K. Wapenaar, 2006, Seismic interferometry turning noise into signal: The Leading Edge, 25, 1082-1092.

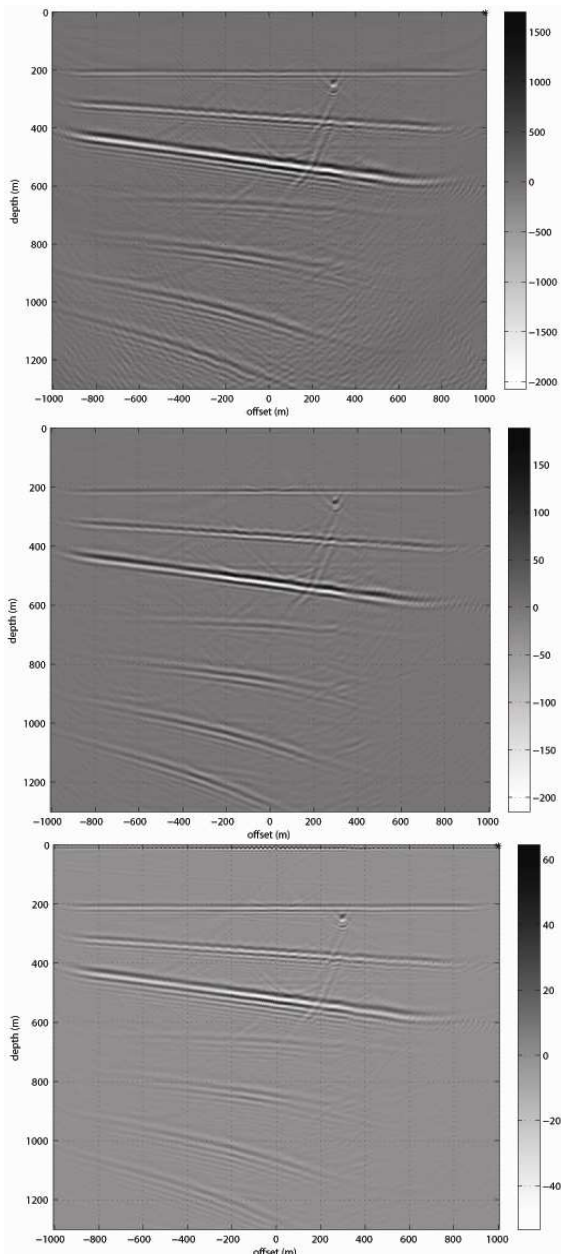


Figure 6. Comparison of images obtained from the estimated down-going wave fields derived from the synthetics exemplified by the data displayed in Figure 4, using interferometric migration according to equation 15 (top), according to equation 16 (middle), and mirror-imaging (bottom).

Djikpesse, H.A., and C. Barnes, 2000, Integrating surface reflection data inversion and offset-VSP modeling for imaging converted S-waves in Gulf coast hydrocarbon reservoirs, in Hansen, P.C., Jacobsen, B.H., and Mosegaard, K., eds., Methods and applications of inversion: Springer, Lecture notes in earth sciences, 92, 82-96.

Djikpesse, H.A., W. Meghirbi, I. Nizkous, and D. Cao, 2006, Borehole-guided AVO analysis of P-P and P-S reflections: quantifying uncertainty on density estimates: Geophysical Prospecting, 54, no.5, 515-523.

Dupal, L. and D. Miller, 1985, Reef delineation by multiple offset borehole seismic profiles: A case study, SEG Technical Program Expanded Abstracts, 105-107

Haldorsen, J., D. Miller, and J. Walsh, 1994, Multichannel Wiener deconvolution of vertical seismic profiles: Geophysics, 59, 1500-1511.

Haldorsen, J., D.E. Miller, and J.J. Walsh, 1995, Walk-away VSP using drill noise as source: Geophysics, 60, 978-997.

Hu, L.Z. and McMechan, G.A., 1986, Migration of VSP data by ray equation extrapolation in 2-D variable velocity media, Geophysical Prospecting 34, 704-734.

Jiang, Z., J. Yu, G.T. Schuster, and B.E. Hornby, 2005, Migration of multiples: The Leading Edge, 24, no.3, 315-318.

Jiang, Z., J. Sheng, J. Yu, G.T. Schuster, and B.E. Hornby, 2007, Migration methods for imaging different-order multiples, Geophysical Prospecting: 55, 1-19.

Lou, M., X. Zhao, F. Doherty and J. Jackson, 2007, Vector Migration of 1st order free surface related downgoing multiples from VSP data, EAGE expanded abstracts, 26, no. 1, 3059-3063.

Miller, D., M. Oristaglio, and G. Beylkin, 1984, A new formalism and an old heuristic for seismic migration, SEG Technical Program Expanded Abstracts, 704-707

Miller, D., M. Oristaglio, and G. Beylkin, 1987, A new slant on seismic imaging: Migration and integral geometry: Geophysics, 52, 943--964.

Payne, M.A., 1994, Looking ahead with vertical seismic profiles: Geophysics, 59, 1182-1191.

Schuster, G.T., 2001, Theory of Daylight/Interferometric Imaging - Tutorial: 63rd Meeting, EAGE, Expanded Abstracts, Session: A-32.

Schuster, G.T., 2009, Seismic Interferometry: Cambridge University Press.

Wapenaar, C.P.A., J.A. Harwijanto, and A.J. Berkhouwt, 1987, VSP migration by single shot record inversion, First Break 5, p 247-255.

Wapenaar, K., D. Draganov, J. Thorbecke, and J. Fokkema, 2002, Theory of acoustic daylight imaging revisited: 72nd Annual International Meeting, SEG, Expanded Abstracts, 2269-2272.

Yu, J., and G. T. Schuster, 2006, Crosscorrelogram migration of inverse vertical seismic profile data: Geophysics, 71, no.1, S1-S12.

Processing seismic ambient noise data at onshore-offshore networks

Andreas Schmidt¹ and the EGELADOS working group

¹ Institute of Geology, Mineralogy, and Geophysics; Ruhr University Bochum, Universitaetsstr. 150 NA 3/176, 44801 Bochum, E-mail: schmidt@geophysik.rub.de

It is shown by various authors that the method of cross-correlating ambient seismic noise records is reliable in direct determination of Rayleigh wave Green functions (RWGF). Here we present the procedure in case of the onshore-offshore EGELADOS network. Therefore, the seismic records of 65 three-component land stations (Guralp, Mark, STS-2) and 22 ocean bottom seismographs (OBS, only Hydrophone component) are available. The network was deployed in the southern Aegean from October 2005 to April 2007. This includes a recording time of 10 months for OBS delimited by project.

The data processing procedure can be divided into following steps: First, we read in seismic records of a specified time interval for two single stations to prepare data by detrending, resampling, and filtering. Further, we identify seismic events and weight down the signal in a specific segment to avoid an additive autocorrelation signal. In addition the amplitudes at both ends of time interval have to be weighted down before cross-correlation. Then a smoothing and whitening procedure of the cross-correlation spectrum follows in frequency domain, complementary. Finally the temporal stacking permits an extraction of the RWGF by increasing the signal-to-noise ratio.

Dispersion analysis of resulting seismograms provides group velocity curves which give information about the crustal and uppermost mantle structure that cannot be obtained from earthquake data. Besides, the slant stacking procedure gives extra information about phase velocity dispersion. In addition we retrieve Love wave dispersion from rotated seismic record components.

Especially inter-station paths between two ocean bottom hydrophones needs more attention because appearance of several

induced wave forms like the acoustic water wave or a pressure wave generated at boundaries. Hence, the bathymetry is a further important impact for onshore Rayleigh wave dispersion analysis.

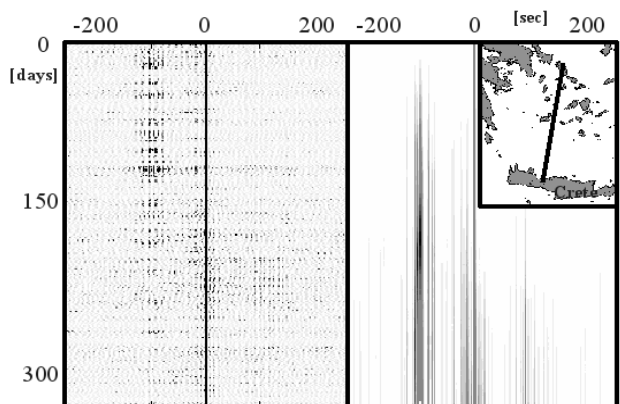


Figure 1. Example of cross-correlation at a single inter-station path. On the left hand side the signal amplitude is plotted for each calculated day. Time vector in positiv direction corresponds to the cross-correlation lag of the path from north to south. Accordant to stronger noise sources the absolut amplitude is significantly higher in negative direction. The development of increasing signal-to-noise ratio is shown on the right hand side. Here, the ordinate is equivalent to the number of stacked days.

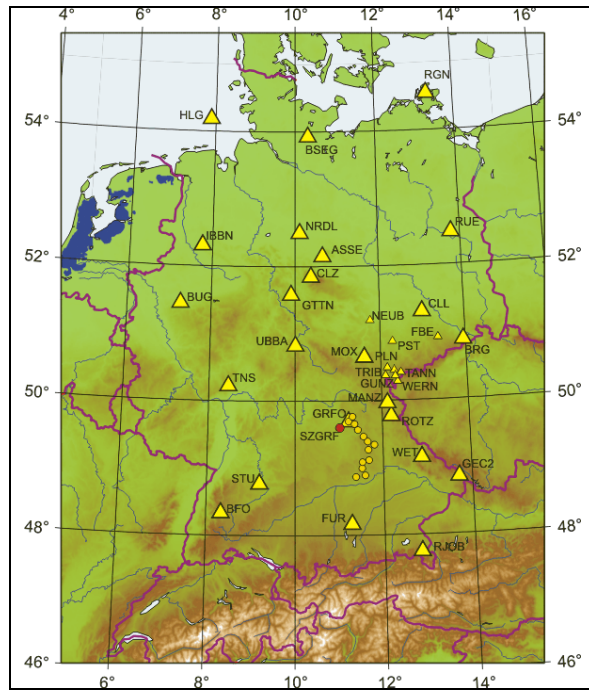
The characteristic of the cross-correlation of ambient noise for some of the stations of the German Regional Seismic Network

Danuta Garus¹, Ulrich Wegler²

Federal Institute for Geosciences and Natural Resources (BGR), Hannover D-30655, Germany, E-mail: ¹ danuta.garus@bgr.de, ² ulrich.wegler@bgr.de

Information about the Earth structure can be retrieved by computing the cross-correlation of the ambient noise (Yang et al., 2008; Larose et al., 2008; Snieder et al., 2007).

Here, we show preliminary characteristic of the cross-correlation of the ambient noise for a few stations of the GRSN array. There are three regional seismic arrays in Germany: GRSN, GRF and GERESS.



The German Regional Seismic Network (GRSN) which includes broadband seismograph stations and is distributed throughout Germany (Korn, 2002). The Broadband Digital Seismic Array Gräfenberg (GRF) which is located in the Franconian Jura of Southern Germany. And the German Experimental Seismic System (GERESS) which includes the short-period stations and is installed in the Bavarian Forest. The distance between the stations for GRSN array is about several

100 km, for GRF array about several 10 km and for GERESS about several 100 m.

We start with a few chosen stations of GRSN array. In figures 1-4 we present the cross-correlation signal between the stations: BFO, BRG, CLL, GEC2, GRA1, MOX, TNS, WET (28 different combinations) relative to the interstation distance [km] and the lag time [s]. The station combination is shown to the right of the traces.

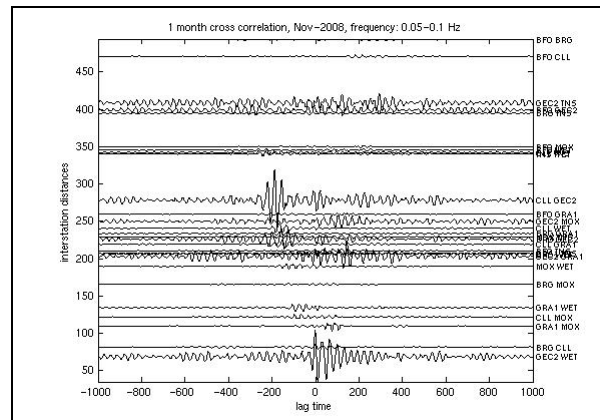


Figure 1. Example of 1-month of cross-correlation. The frequency band covers the primary microseism band (0.05 – 0.1 Hz).

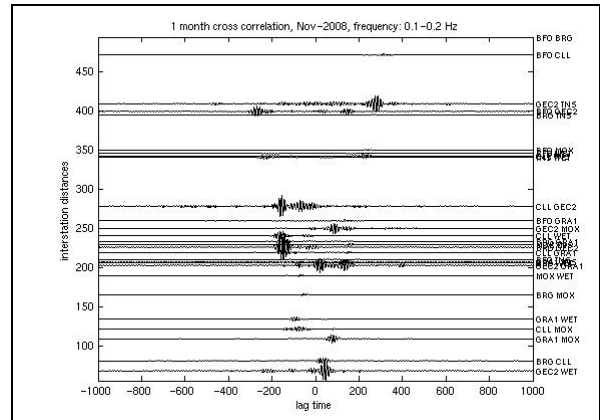


Figure 2. Example of 1-month of cross-correlation. The frequency band covers the secondary microseism band (0.1 – 0.2 Hz).

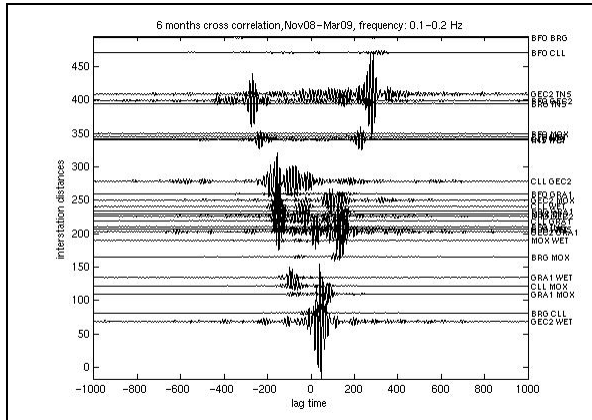


Figure 3. Example of 6-months of cross-correlation. The frequency band covers the secondary microseism band (0.1 – 0.2 Hz).

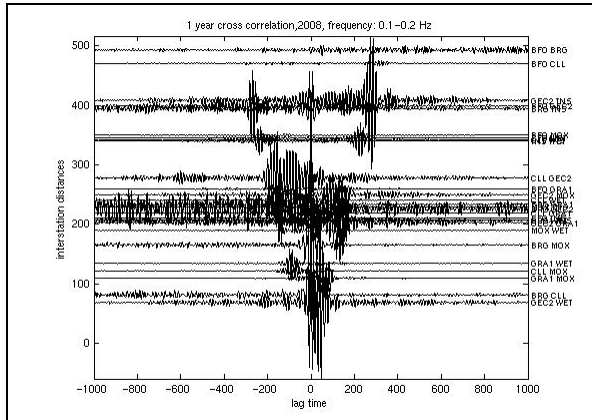


Figure 4. Example of 1-year of cross-correlation. The frequency band covers the secondary microseism band (0.1 – 0.2 Hz).

We used the continuous vertical component seismic signal over 1, 6, and 12 months. We calculated the cross-correlation for all stations pairs for each time window (819,2 s) and then stacked up to receive 1-month, 6-months and 1-year time series. The trend was removed and data were band-pass filtered from 5 to 10 s, and from 10 to 20 s. The RMS threshold values (upper and lower) were used to cut both the earthquakes and the gaps from the noise signal. In figures 2-4 we used the same amplitude scale for all data. In figure 1 the scale is larger because the amplitude of the signal is much smaller compared to the results presented in fig. 2-4.

In all figures 1-4 we can see the Rayleigh wave signal, but only in a few cases the signal appears symmetrical to the zero arrival time. It indicates heterogeneous azimuthal distribution of ambient noise.

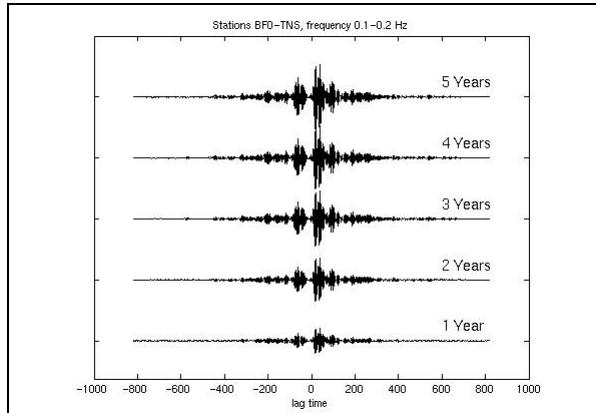


Figure 5. The cross-correlation between stations BFO and TNS summed up over different periods. The frequency band covers the secondary microseism band (0.1 – 0.2 Hz).

Next, for each year from 1st of the January 2004 to 31st of December 2008, we calculated the 1-year time series and then added to one another to receive 1, 2, 3, 4 and 5-years time series. Figure 5 shows the cross-correlation between stations BFO and TNS. Here, the ambient noise sources have more homogeneous azimuthal distribution. We can observe that the characteristic of the signal is constant and only its amplitude rises.

References

- Y. Yang, M. Ritzwoller, 2008: Characteristics of ambient seismic noise as a source for surface wave tomography. *Geochemistry, Geophysics, Geosystems*, 9, Q02008, doi:10.1029/2007GC001814
- E. Larose, A. Derode, P. Roux, M. Campillo, 2008: Fluctuations of correlations and Green's functions reconstruction: role of scattering. *The Journal of Applied Physics*
- R. S. Snieder, K. Wapenaar, U. Wegler, 2007: Unified Green's function retrieval by cross-correlation with energy principles. *Physical Review E* 75, 036103
- Korn M., 2002: Ten Years of German Regional Seismic Network (GRSN). WILEY-VCH DFG, Report 25 of the Senate Commission for Geosciences

Time Reverse Localization of Sources in Non-Destructive Testing and Exploration Geophysics: Similarities and Differences

Erik H. Saenger¹, Georg Karl Kocur², Roman Jud³, Brian Steiner⁴

¹ Geological Institute, ETH Zürich, Switzerland and Spectraseis AG, 8005 Zürich, Switzerland, E-mail: erik.saenger@erdw.ethz.ch

² Institute of Structural Engineering, ETH Zürich, Switzerland, E-mail: kocur@ibk.baug.ethz.ch

³ Seminar for Applied Mathematics, ETH Zürich, Switzerland, E-mail: roman.jud@gmx.ch

⁴ Spectraseis AG, 8005 Zürich, Switzerland, E-mail: brian.steiner@spectraseis.com

Time Reverse Modeling (TRM) is applied in several fields of science such as Medical and Earth Sciences (Fink, 1999). We want to transfer a TRM-approach within exploration geophysics to applications within the field of non-destructive-testing (NDT).

Steiner et al. 2008 applied TRM of the recorded surface wave field to better understand the passive low-frequency seismic wave field around hydrocarbon reservoirs and to investigate whether some of the low-frequency signals originate from hydrocarbon reservoirs. The TRM methodology uses numerical algorithms for elastic wave propagation in combination with a new imaging condition. The imaging condition therein is implemented because the measured low-frequency tremor signals were more or less continuous in time and no individual events or first arrival times could be detected. During TRM recorded seismic energy is propagated back to its origin. The seismograms recorded with synchronized three-component seismometers are reversed in time and implemented as sources for numerical wave extrapolation. The signals are propagated backwards through the velocity model. The backward propagated energy will focus at the source location, if the velocity model is accurate (Figure 1).

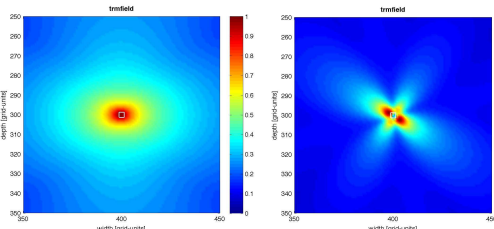


Figure 1. Different TRM-maximum particle displacement patterns for explosion (left hand side) and double-couple sources (right hand side) will allow their characterization.

Concrete is a strongly heterogeneous and high-packed composite material and represents a very important but also very difficult object for ultrasonic non-destructive-testing methods (Figure 2). Due to the high scatterer density, ultrasonic wave propagation in this material consists of a complex mixture of multiple scattering, mode conversion and diffusive energy transport. In order to obtain a better understanding of the effect of aggregates and porosity on elastic wave propagation in concrete and to optimise inverse reconstruction techniques, e.g. impact echo methods, it is useful to simulate the wave propagation and scattering process explicitly in the time domain.

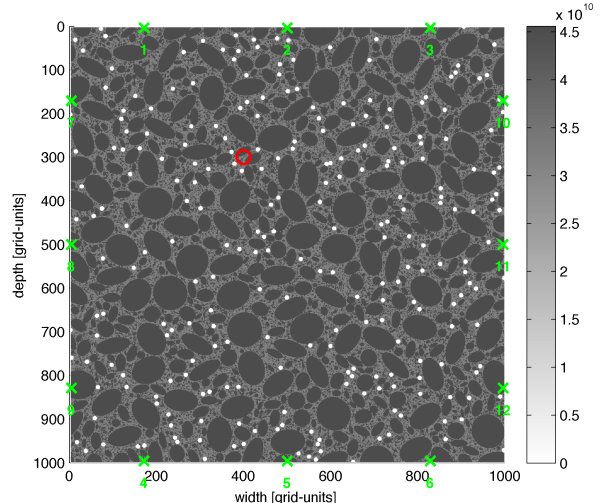


Figure 2. Synthetic model of concrete (similar to X-Ray CT of concrete). Three constituents are used: Cement paste, aggregates and air voids. The grain-size distribution is taken from a real concrete mix and is in agreement with the Fuller curve.

Acoustic emissions (AE) are caused by strain energy release and occur with all building materials. Acoustic emission analysis (AEA) has become a promising method to evaluate

the condition of concrete structures. Qualitative procedures make use of basic parameters of recorded signals and try to identify the load history and the stage of degradation. Quantitative procedures try to identify all characteristics of an AE source and therefore have to consider the wave propagation between source and sensors. Profiting from the methods of geophysics, promising results have been achieved. This includes the determination of arrival times (picking), source localization and moment tensor analysis. Further progress depends on the handling of cracking and cracked concrete as the medium for elastic wave propagation and the elements of structural concrete like reinforcement, post-tensioning tendons and inserts.

Non-Destructive Testing	Exploration Geophysics
X-Ray CT images are possible	Velocity model from active seismic
Wave energy will remain in the system	Wave energy can “escape” at damping boundaries
Transducer can be of same size as wavelength; often only a few are available	Highly sensitive broadband sensors are available
dm-scale	km-scale
Effective elastic properties can be estimated	S-wave velocities are difficult to be determined

Table 1. Differences and similarities for TRM applied in non-destructive-testing and exploration geophysics.

We aim to establish a relation between crack growth and the AE activity that is recorded at the surfaces of a structure by sensors. The

References

- Fink, M., Time-reversed acoustics, *Scientific American*, 67–73, 1999.
 Grosse, C. U., Advances in Construction Materials 2007, Springer, ISBN: 978-3-540-72447-6, Heidelberg, 2007.

proceeding cracking of the concrete serving as a medium for elastic wave propagation shall be observed, described, interpreted and modeled. One aspect is to transfer the time-reverse modelling localization procedure by Steiner et al. 2008 from geophysical exploration to the field of non-destructive testing (Table 1) in order to image crack growth in loaded concrete. With TRM, receivers located like those in the physical model are considered as sources in the numerical simulation. AE are traced back in time, and the location of the generating fracture process becomes visible as a concentration of elastic energy. Advantages of this method are the independency of detection/picking algorithms, the capability to handle low signal to noise ratios, and a possible identification of the moment tensor of the AE. A successful synthetic example is shown in Figure 3.

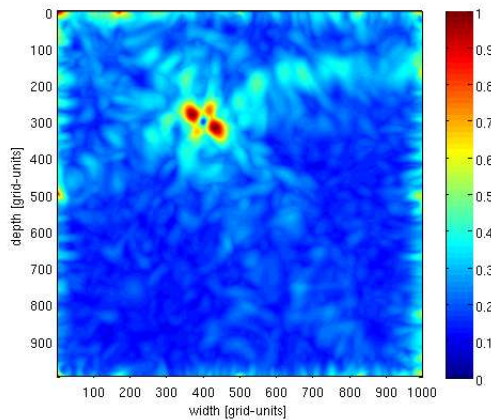


Figure 3. TRM-localization pattern for a double-couple source located at (400,300). The forward simulation used the original concrete model shown in Figure 2 whereas the TRM-simulation used effective elastic properties of concrete. Twelve sensors, three on each side, are implemented.

- Steiner, B., E. H. Saenger, S. M. Schmalholz, Time reverse modeling of low-frequency microtremors: A potential method for hydrocarbon reservoir localization, *Geophysical Research Letters* 35, L03307, 2008.

Phase statistics of seismic coda waves

Ludovic Margerin¹, Domitille Anache-Ménier², Bart Van Tiggelen²

¹ Centre Européen de Recherche et d'Enseignement de Géosciences de l'Environnement, Université Aix Marseille-C.N.R.S., Europôle méditerranéen de l'Arbois, BP 80, 13545 Aix en Provence, France

² Laboratoire de Physique et Modélisation de la Matière Condensée, Université Joseph Fourier-C.N.R.S., Maison des Magistères, 25 Avenue des Martyrs, BP166, 38042 Grenoble, France

Introduction

In the short-period band, ballistic arrivals are often masked by scattered waves due to small-scale heterogeneities in the lithosphere. The scattered waves form the pronounced tail of seismograms known as the seismic coda. Even when scattering is prominent, it is still possible to define the phase of the seismic record by introducing the associated complex analytic signal. In the past, many studies have focused on the modeling of the mean field intensity. The goal of the present paper is to study the statistics of the phase field. In the coda, the measured displacements result from the superposition of many partial waves which have propagated along different paths between the source and the receiver. Each path consists of a sequence of scattering events which affect differently the phase of the corresponding partial wave. For narrow-band signals, the phase field can therefore be written as $\phi(t,r) = \omega t + \delta\phi(t,r)$, where ω is the central frequency, and $\delta\phi$ denotes the random fluctuations. Because the phase is dominated by the uninteresting ωt term, it is necessary to consider the spatial phase shifts between two neighboring points. Such measurements are made possible by the development of dense arrays of seismometers. We note that the phase of coda waves is not affected by anelasticity or earthquake magnitude, and is therefore a good candidate to isolate scattering properties from absorption effects.

Phase Measurements

We study data sets from a temporary experiment deployed at Pinyon Flat Observatory (PFO), California, in 1990 by an

IRIS program. This site presents a high level of regional seismic activity. The array contained 58 3-components L-22 sensors (2Hz) and was configured as a grid and two orthogonal arms with sensor spacings of 7 meters within the grid and 21 meters on the arms. We selected 8 earthquakes of magnitude greater than 2 with good signal to noise ratio in the coda. Typically, epicentral distances are less than 110 km and the coda lasts more than 30 seconds. In what follows the phase measurement is discussed in details. To perform the statistical analysis, we filtered the signal in a narrow frequency band centered around $7\text{Hz} \pm 5\%$ and selected a 15s time window starting around 5s after the direct arrivals. In this time window, the signal is dominated by multiple scattering and is highly coherent along the array. We evaluate the Hilbert transform of the vertical displacement which yields the imaginary part of the complex analytic signal:

$$\psi(t,r) = A(t,r)\text{Exp}[i\phi(t,r)].$$

From the complex field, two definitions of the phase can be given: (1) The wrapped phase ϕ is defined as the argument of the complex field in the range $(-\pi, \pi)$. (2) The unwrapped phase ϕ_u is obtained by correcting for the 2π jumps occurring when ϕ goes through the value π , to obtain a continuous function with values in \mathbb{R} . The ϕ distribution is flat. More information can be extracted by considering higher-order statistics of the phase. For this purpose we consider the spatial derivative of the phase, which can be estimated in two different ways: (1) The first measurement relies on the difference of the wrapped phases $\Delta\phi$ between two seismometers located δ meters apart. Applying the simple finite difference formula $\phi' = \Delta\phi/\delta$, an estimate of

the derivative is obtained. (2) The second method uses the difference of the phase spatially unwrapped ϕ_u at each time step. This yields another estimate of the derivative: $\phi' = \Delta\phi_u/\delta$, which is expected to suppress finite difference artifacts. In practice it is impossible to discriminate a rare but physical large phase fluctuation from a small fluctuation that causes a 2π jump within δ . The only possibility along 1-D arrays is to impose that the largest admissible phase difference between two stations be smaller than pi. In the limit δ tends to 0, the two definitions are equivalent because the probability of phase jumps between the two stations tends to 0. The results of the phase derivative measurement are presented in Figure 1.

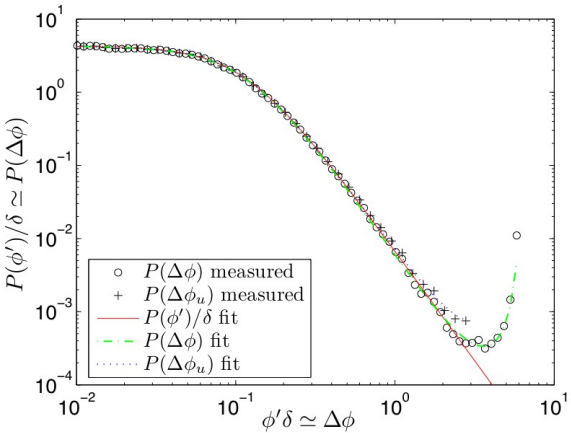


Figure 1: Distribution of the first derivative of the phase normalized by the inter-station distance delta and measured using finite difference formula. \circ : wrapped phase; $+$: unwrapped phase. The color lines represent the fits with Gaussian theory. Green: wrapped phase; blue: unwrapped phase; red: phase derivative.

To interpret our results we assume that the coda waves can be described by circular Gaussian statistics (CGS). The Gaussian hypothesis can be justified by the following simple argument. The coda results from a superposition of many partial waves corresponding to different paths in the medium. Upon scattering, the partial waves are prone to random and independent phase shifts which allows application of the central limit theorem. The comparison between gaussian theory and data is shown in Figure 1, and demonstrates that the phase difference between

two nearby seismometers follows Gaussian circular statistics with excellent accuracy.

Phase Difference correlation

We use the phase difference correlations to put some constraints on the degree of heterogeneity which is responsible for long-range decorrelations along the array. In the Gaussian hypothesis and for surface waves, we calculate the theoretical phase derivative correlation function:

$C(r) \sim k/(\pi r) \exp(-r/l)$, where l is the mean free path of the waves, r is the distance between stations and k is the wavenumber. The formula relies on the form of the field correlation function and is derived from the Gaussian joint probability of 4 fields. The formula has particularly interesting properties. Contrary to the field correlation function, C does not oscillate on the wavelength scale and decreases with the mean free path as the only characteristic length scale.

As above, we estimate the phase derivative correlation function in a finite difference approximation. The unwrapped phase difference correlation is measured along the two orthogonal arms with an aperture of 252m and $\delta=21$ m interstation distance. The results are shown in Figure 2. Although only loose bounds are provided in this study, our work suggests a new method to estimate the degree of heterogeneity of the crust.

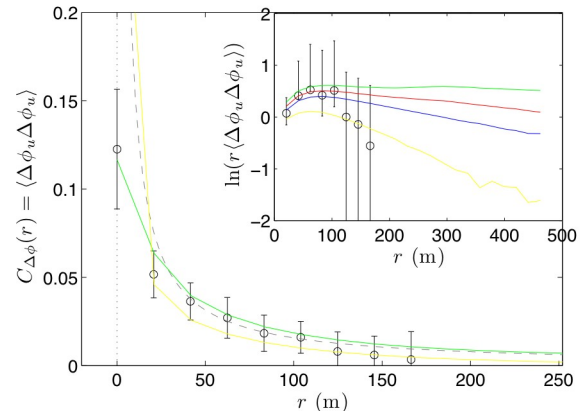


Figure 2: Unwrapped phase difference correlation function. \circ : experimental results. Dashed line: $1/r$ fit. Inset: logarithm of the correlation multiplied by r for data and numerical simulations at fixed k and $l=10$ km (green), $l=1$ km (red), $l=500$ m (blue) and $l=200$ m (yellow).

Lg-blockage in the western Pyrenees explained with locally increased heterogeneity based on radiative transfer theory

Christoph Sens-Schönfelder¹, Ludovic Margerin²

¹ Institut of Geophysics and Geology, University of Leipzig, Leipzig, Germany E-mail: sens-schoenfelder@uni-leipzig.de

² Centre Européen de Recherche et d'Enseignement des Géosciences de l'Environnement (CEREGE), Aix-en-Provence, France, E-mail: margerin@cerege.fr

Introduction

The phenomenon of Lg-blockage refers to an anomalous attenuation of seismic waves in the Earth's crust. It is widely known from thick marine sediment basins that trap the crustal waves in the low velocity region. Some mountain ranges like the European Alpine range and the Pyrenees do also show such a strong attenuation of crustal seismic phases. In these cases the macroscopic velocity structure does not contain sufficient velocity contrast and attempts to model the Lg-blockage by the western Pyrenees on the basis of the large scale velocity structure failed (Chazalon, 1993). So it was speculated that scattering at small scale heterogeneity is an important factor for the attenuation of crustal waves. To test this hypothesis we analyzed new data of Spanish earthquakes that were recorded in France after crossing the Pyrenean mountain range and devised a Monte-Carlo algorithm for the simulation of these seismogram envelopes based on radiative transfer theory.

Observation and Modeling

The new data set supports the observation of Lg-blockage made in previous studies. Depending on the position where the waves crossed the Pyrenees the amplitude ratio between crustal and mantle phases changes dramatically. Whereas the waves that cross the eastern part of the Pyrenees show the typical shape of seismograms at regional distances that are dominated by the Pg and Sg (Lg) waves, these phases are almost absent after propagation through the western Pyrenees.

To model this observation we propose the model depicted in figure 1. It consists of a layer with laterally variable heterogeneity

above a half space with a vertical gradient of the mean velocity.

The algorithm that we implemented to calculate the seismogram envelopes, simulates the elastic transfer of seismic energy in this structural model. The algorithm takes into account the conversion between P- and S-waves at the surface as well as at the interface between mantle and crust. To model the differences between the eastern and the western parts of the Pyrenees the model includes an additional body (red cube in figure 1) in the crust beneath the western part that differs in the scattering and attenuation properties from the surrounding material. Heterogeneity is modeled with fluctuations with an exponential auto-correlation function. With a genetic algorithm we estimated parameters of the random media in the mantle, the crust, and the supplementary body that best explain the observed envelopes for both, the propagation through the eastern and western parts of the mountain range.

Results

Our modeling indicates that the strong attenuation of crustal phases might indeed be caused by increased small scale heterogeneity. Intrinsic attenuation on the contrary does not suffice to explain the observation. The best result is obtained with slightly increased attenuation and significantly increased heterogeneity in the body under the western Pyrenees. Figure 2 shows the observed and modeled seismogram envelopes for the eastern and western Pyrenees. Snapshots of the energy field are shown in figure 3.

References

Chazalon, A., M. Campillo, R. Gibson, E. Carreno, Crustal wave propagation anomaly

across the Pyrenean Range. Comparison between observations and numerical simulations, Geophys. J. Int., v. 115, pp. 829-838, doi:10.1111/j.1365-246X.1993.tb01495.x, 1993

Figure 1. Structural model that is used to explain the Lg-blockage in the western Pyrenees. The red box marks the region with increased scattering and attenuation.

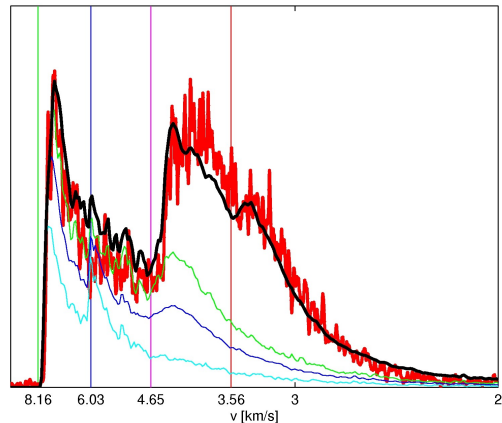
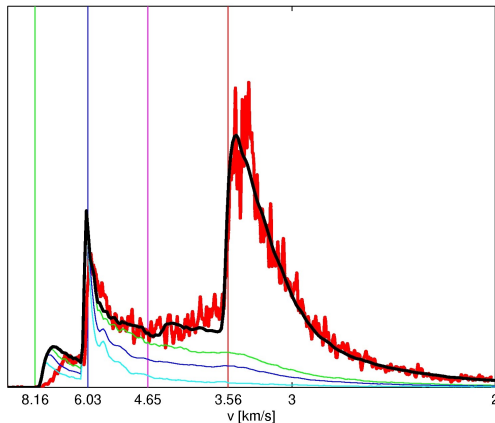
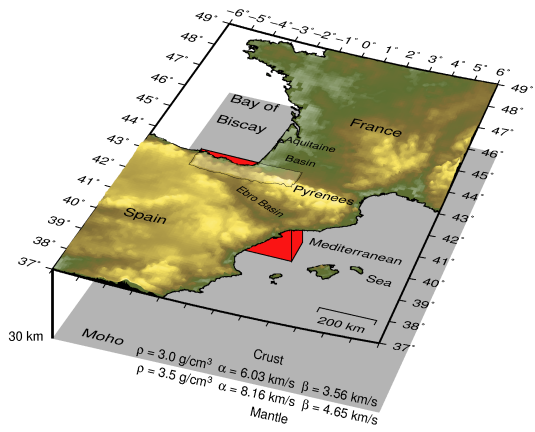


Figure 2. Observed (black curves) and modeled (red curves) envelopes of seismograms for propagation through the undisturbed eastern (left figure) and western (right figure) part of the Pyrenees

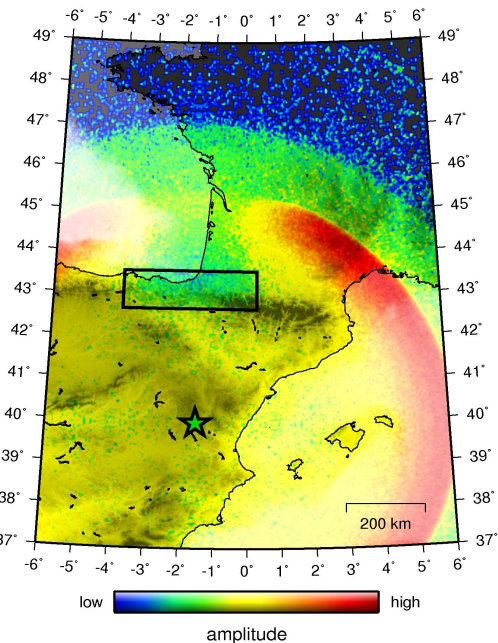
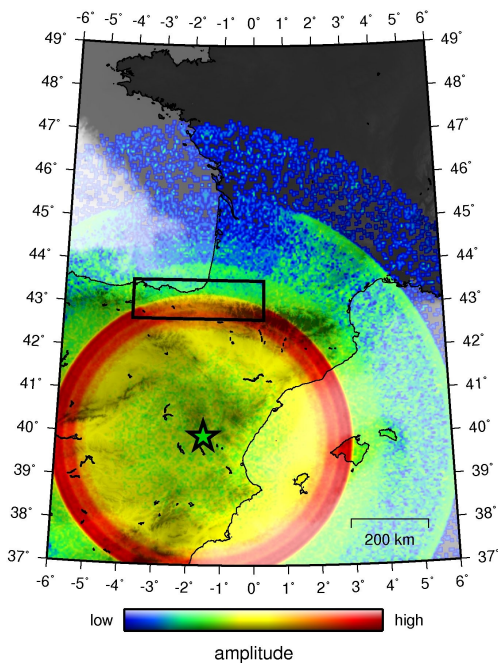


Figure 3. Snapshots of the energy distribution at the surface of the crust 105s (left figure) and 180s (right figure) after an earthquake in Spain. The black box indicates the region of increased heterogeneity. Nicely seen is the gap in the Pg wave (left) and Lg wave (right) whereas the wave fronts of the mantle phases are continuous.

Stability of Monitoring Weak Changes in Multiply Scattering Media with Ambient Noise Correlation: Laboratory Experiments.

Céline Hadzioannou, Eric Larose, Olivier Coutant, Philippe Roux, Michel Campillo

Laboratoire de Géophysique Interne et Tectonophysique, CNRS & Université J. Fourier, BP53, 38041 Grenoble, France. E-mail: hadzio@obs.ujf-grenoble.fr

Small changes in a dynamic, multiply scattering medium can be monitored by observing phase shifts in the coda. Passive monitoring of weak changes through ambient noise correlation has already been applied to seismology, acoustics and engineering. Usually, this is done under the assumption that a properly reconstructed Green function as well as stable background noise sources are necessary, as is the case with passive imaging. In seismology many parameters remain unknown or uncontrolled. In a passive field experiment, scientists face two simultaneous problems. They neither know the source location with sufficient precision, the source mechanism, nor the medium of propagation. It is therefore very complex to characterize the source and the medium at the same time. By reproducing some features of the seismic propagation in the laboratory and employing controlled sources and sensors, we can focus our efforts on the physics of the wave propagation and develop or evaluate new methods more comfortably.

In order to further develop the passive monitoring technique, we perform a laboratory experiment in the 2.5MHz range in a gel with scattering inclusions. We compare an active (pulse-echo) form of monitoring to a passive (correlation) one. The results show that small temperature changes in the medium can be observed even if the Green function of the medium is not reconstructed.

We also establish that relative stability of the background noise structure is a necessary condition in the case where the Green function is not reconstructed.

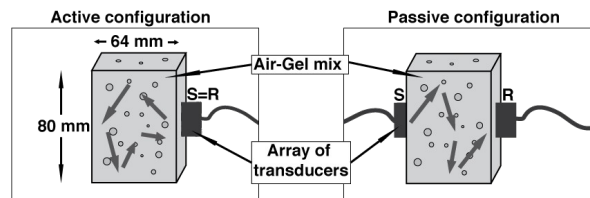


Figure 1. Experimental setup. Left: the active experiment in the pulse-echo configuration. Right: the passive experiment in the transmission configuration before autocorrelation.

References

- C. Hadzioannou, E. Larose , O. Coutant, P. Roux and M. Campillo: Stability of Monitoring Weak Changes in Multiply Scattering Media with Ambient Noise Correlation: Laboratory Experiments., J. Acoust. Soc. Am. 125 in press (2009)

Noise based seismic monitoring of the CO₂-Sequestration site Ketzin, Germany

Robert Mündel¹, Christoph Sens-Schönfelder¹, Michael Korn¹

¹ Institute of Geophysics and Geology, University of Leipzig, Germany, E-mail:

pge06@studserv.uni-leipzig.de, sens-schoenfelder@uni-leipzig.de, mikorn@uni-leipzig.de,

In this work we describe an experiment to test the feasibility to monitor the CO₂-Sequestration in Ketzin by analysing the ambient seismic noise. During injection water in the aquifer is replaced by CO₂. This process decreases the density and the bulk modulus [1] which results in reduced seismic velocities. Passive Image Interferometry is ideally suited to observe this kind of temporal changes, because it is based on seismic noise from distant sources and allows to continuously monitor variations of the seismic velocity with high precision. For this purpose we installed a temporary seismic network of seven seismic stations in the injection area. The station network (fig. 2) has an east-west extent about 2.4 km and a north-south extent about 4 km. Three seismometers are placed on the injection site, one of them 20 m far away from the injection well, and two more about 200 m away. The start of the measurements was May 16 2008 well before the beginning of the injection. To check the quality of the stations we looked for the micro seismic peaks that we can observe with variable strength at all stations. A dominant component in the signals is anthropogenic noise during daytime with sources close to the stations within the array. However, over night from 22 pm to 5 am and during weekends the data are relatively quiet indicating a more favourable source distribution. On the injection site strong technical noise is generated by pumps and other equipment. Due to these particular circumstances, the retrieval of Green's function approximations by cross-correlation requires some care to be taken. Without processing of the raw data the correlations do not show any signatures of seismic phases. However, with frequency-whitening and subsequent

filtering between 0.01 and 20 Hz clear phases can be observed that are related to waves travelling between the stations at a velocity of about 300 m/s. With the rotation of north-south and east-west components into R(Radial)- and T(Transversal)-components relative to the orientation of the station pairs (fig. 1) we facilitate the identification of different wave types. The 300 m/s phase is asymmetrically distributed in the correlations indicating a preferred source direction. To further characterize the dominant phase we measured the dispersion and compare it with predictions from velocity profiles obtained from active seismic studies (fig. 3). Two branches can be observed. Below 2 Hz the slowness is about 0.002 s/m and above 2 Hz the slowness is about 0.0035. The dispersion predicted by the velocity profile for Rayleigh waves is indicated by the gray line in fig. 3. There is a notable discrepancy between the observed and measured dispersion curves. This fact and the velocity of about 300 m/s which is in the range of the sonic velocity, led to the speculation that the phase at 300 m/s is related to a pressure wave in the air that might originate from nearby wind power plants. So we tested the relationship between amplitudes of the cross-correlation and the wind speed. In the frequency range between 1 and 5 Hz a clear correlation with wind speed is found for the amplitude of the phase in the retrieved Green's functions as well as for the raw data. Therefor the comparison with wind speed does not allow conclusions about the origin of this phase. To further characterise the wave field we started to compare Green's functions, from different time periods and different station pairs, to detect possible changes in the travel times of the 300 m/s

phase. The interferometry reveals collective travel time variations for different station pairs (fig. 4). The curve that we infer from the seven month of data shows a travel time minimum in the autumn and would be consistent with an annual cycle. It does no bear a similarity with the almost continuous CO₂-Injektion.

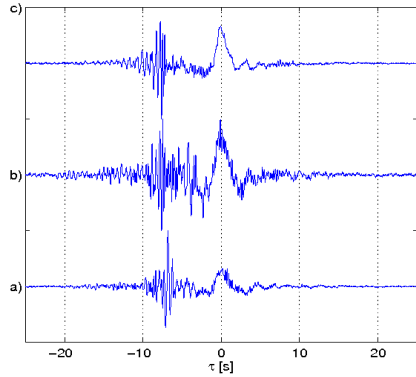


Figure 1: The cross correlations of T- (a), R- (b) and Z-(c) components of KTC KTW. In all three components a peak at -8s is clearly visible. The distance between KTC KTW is about 2200 m corresponding to a velocity of about 300 m/s.

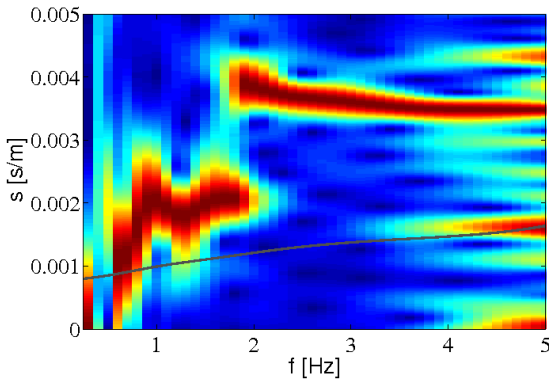


Figure 3: Dispersion characteristic of the KTC KTW path (R-component). The cross correlations were stacked for one month, normalized by their distance, and filtered in small frequency bands. The dark red region from 2 to 5 Hz indicates the 300 m/s phase. The gray line indicates the modelled slownesses of Rayleigh waves for a velocity model obtained with active seismic measurements around the injection site[2].

Acknowledgments

We are greatful for the logistical support of GFZ Potsdam and CO2SINK group.

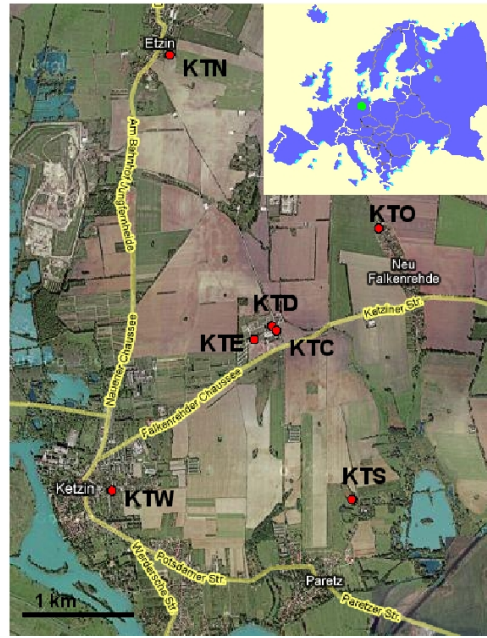


Figure 2: Station network of seven temporally seismic stations near Ketzin close to Potsdam. The injection site is shown on the inset (green dot). The red dots mark the stations. The injection well is 20m away from station KTE.

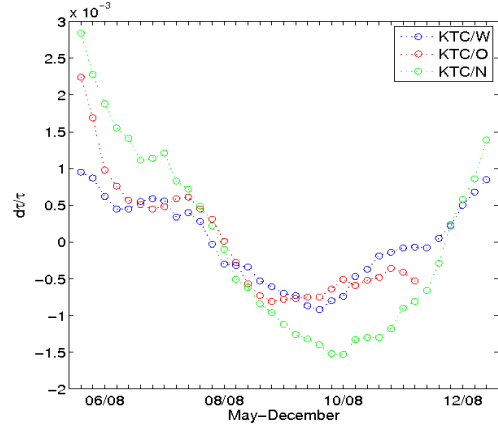


Figure 4: Travel time variations of the 300 m/s phase for different station pairs in the frequency range from 1 to 5 Hz. To calculate travel time varations, cross correlations were computed from ten minutes time windows and stacked for one month. Here we observe an increasing velocity until Sep.08 and a decresing afterwards. For a process connected to the almost continous CO₂-Injection we would expect a monotonic variation.

References

- [1] <http://www.co2sink.de/techinfo/seismic.htm>
- [2] Shallow velocity-depth modell..., S.Yordkayhun et al., journal of Applied Geophysics, 2007, Vol. 63, p.68-79

METSEIS: An Experiment to Quantify Meteorological and Seismological Interactions

Joachim Ritter¹, Johannes Thun¹, Jörn Groos¹, Friedemann Wenzel¹, Christian Hauck²

¹ Geophysikalisches Institut, Universität Karlsruhe (TH), Germany, E-mail: joachim.ritter@gpi.uni-karlsruhe.de, j.thun@mail.de, joern.groos@gpi.uni-karlsruhe.de, friedemann.wenzel@gpi.uni-karlsruhe.de

² Institute for Meteorology and Climate Research, Forschungszentrum Karlsruhe, now at Department of Geosciences, University of Fribourg, Switzerland, E-mail: christian.hauck@unifr.ch

Background

The continuous (back)ground motion of the Earth's surface, often called seismic noise covers all observable frequency bands (Peterson, 1993; Berger et al., 2004). The noise sources involve a wide range of natural and anthropogenic processes which overlap and show distinct time and spatial variations at different scales (e.g. Aster et al., 2008). Very low frequency noise (<0.1 Hz) is excited by barometric pressure variations and there are models which describe this mechanism (Zürn, 2002). At about 0.05-0.3 Hz the ocean-generated microseismicity dominates even far away from coastlines, and variations of these microseisms can be used to describe the wave climate and their propulsive storm systems based on onshore, ocean-bottom and buoy data (Bromirski and Duennebier, 2002). At higher frequencies (0.1 Hz to ~100 Hz) meteorological and man-made processes induce seismic noise which strongly depends on time and location (Wilson et al., 2002).

Over the last 10 years the use of ambient seismic noise as signal increased tremendously (Curtis et al., 2006). Analyses of seismic noise allow the characterisation of near-surface structure for seismic hazard assessment (Bonnefoy-Claudet et al., 2006), lithospheric studies (Shapiro et al., 2005), global applications (Kurrale and Widmer-Schniedrig, 2008) and subtle time-varying phenomena (Sens-Schönfelder and Wegler, 2006).

The wide application of ambient noise data focused on the *utilisation* of noise rather than the *characterisation* of the noise itself and its *sources* (Bonnefoy-Claudet et al., 2006). Our

aim is to contribute to the understanding of noise generation at about 0.01-40 Hz due to meteorological influence with a focus on the higher frequency range. Wind and storms are major noise sources of local and long-range relevance as they generate ocean waves. Also rainfall and temperature influence seismic noise in various direct and indirect ways. The interaction of such meteorological and seismological phenomena is known since about 100 years; however there are still few systematic measurements. Therefore we initiated the METSEIS project to derive data-based, qualitative and quantitative relations between meteorological phenomena and ground motion. In a joint experiment of the Geophysical Institute at the Universität Karlsruhe (TH) (GPI, Uni KA) and the Institute for Meteorology and Climate Research at the Forschungszentrum Karlsruhe (IMK, FZK) we measured basic data to tackle this problem.

Goals and Objectives

The METSEIS project aims at the following research topics:

- Derivation of a quantitative relationship between wind speed and power spectral density (psd) of ground motion in different frequency bands
- Determination of the influence of wind gusts on psd of ground motion in different frequency bands
- Determination of the influence of wind direction at specific sites on psd of ground motion

- Derivation of a quantitative relationship between rain fall and psd of ground motion in different frequency bands
- Estimation of the influence of temperature on ground motion

To determine the characteristics of seismic noise in terms of noise strength we calculate the power spectral density (psd) of our time series. Statistical variations of seismic noise are measured using the method of Groos and Ritter (2008 and this volume). Correlation techniques are applied to psd of seismic noise and meteorological parameters.

The outcome of this study will allow a better understanding of the generation of noise by different weather phenomena. This knowledge can then be applied for a better understanding of seismic noise time series which are used to derive seismic site effect estimates or structural information. Our results can be used also to test whether assumptions on the properties of seismic noise, which are required for some methods, are fulfilled or not in real situations. An application could be the determination of H/V measurements during different wind situations etc. (Nakamura method, see e.g. Parolai and Galiana-Merino, 2006).

Experimental Design

The METSEIS experiment with concerted meteorological and seismological measurements is conducted in Southwest Germany (Fig. 1). Recordings from permanent stations are used as long-term observations (2000–2008). As study area for a temporary, denser observational network we choose the area between Karlsruhe and Stuttgart (Fig. 1), because it covers different climatic regions and ground conditions (Upper Rhine Graben, Black Forest and Filderebene). The meteorological and seismic noise properties in this region are partly known from previous studies and the logistical conditions are relatively easy to handle.

Four permanent seismological stations are located in the city of Stuttgart and in the Black Forest, Taunus and Walferdange observatories (STU, BFO, TNS and WLF in Fig. 1). Close to these sites meteorological measurements are available from the

Deutscher Wetterdienst (DWD, Germany's National Meteorological Service) at stations 4931 (Stuttgart-Echterdingen), 1468 (Freudenstadt), 2601 (Feldberg, Taunus) and 5100 (Trier). For BFO there are also onsite weather data available.

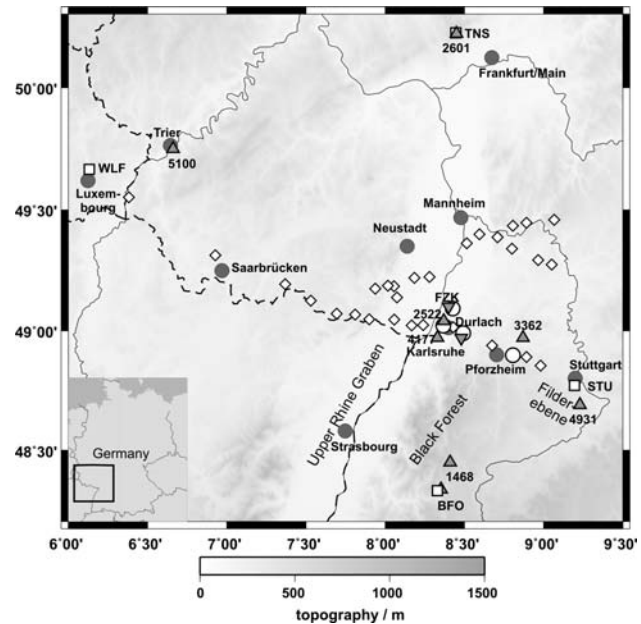


Figure 1. Map displaying the METSEIS experiment with seismological and meteorological observation sites. White circles indicate seismological stations especially deployed for METSEIS, white squares (BFO, STU, TNS, WLF) are permanent seismological observatories. Grey triangles are permanent DWD meteorological observatories (incl. number code) and inverted triangles are meteorological observation sites at FZK and in Durlach (see text). Further seismological data are available from the TIMO experiment (diamond symbols) from Dec. 2004 until May 2006 (Ritter et al., 2008).

Between June 2008 and May 2009 four temporary broadband seismological stations were recording (Fig. 2) close to meteorological observational sites: One seismological observational site (TM47) was on the ground of the FZK where wind measurements are conducted at different heights at a special mast (FZKM). Station TM45 is in the basement of the GPI building in Karlsruhe. TM47 and TM45 are located inside the Upper Rhine Graben. Meteorological data are provided from the DWD at sites 2522 (Karlsruhe) and 4177 (Rheinstetten). Seismological station TM44 is placed on the shoulder of the Upper Rhine Graben at the rim of Durlach and there

meteorological data are provided by a private weather station (DURM; www.wetterstation-karlsruhe.de) through a co-operation. Close to DWD station 3362 (Mühlacker) we placed seismological station TM03 (Öschelbronn) at the northern rim of the Black Forest.

The seismological and meteorological measurements were conducted partly not at an identical position but at some distance. As the excitation of seismic noise occurs across a wide area from which the noise signals interfere at a specific site we expect that this distance does not cause errors during the correlation. This assumption will be an issue of the analysis during METSEIS.

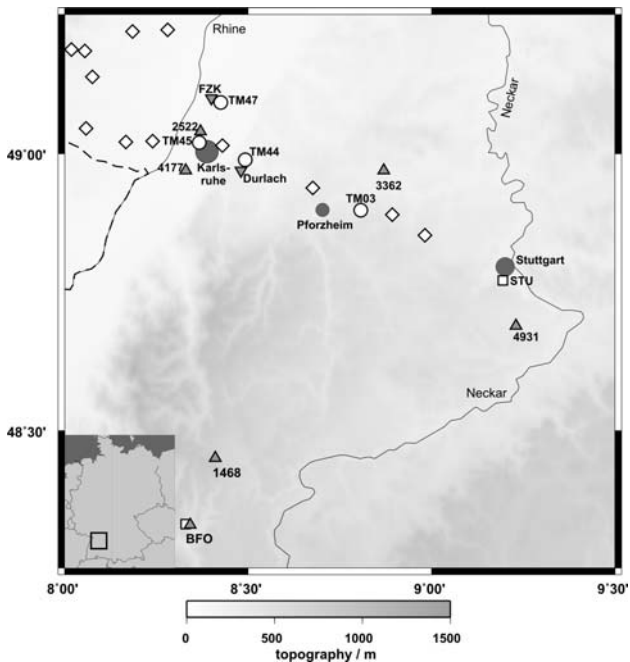


Figure 2. Enlarged view on the METSEIS experiment from Figure 1.

The four temporary seismological stations were equipped with broadband instruments from the KArlsruhe BroadBand Array (KABBA). Recording was done with three channels (vertical, N-S and E-W) at 100 samples per second, and time synchronisation using GPS satellite signals (Global Positioning System). Data loggers were Earthdata PR-6 with 24-bit digitisers. At the beginning of the experiment we added near-real time data routers which transmitted the waveforms via the mobile phone network using GSM-Edge or UMTS technology. The data were received at GPI including a transmission protocol.

Additionally all data were recorded on the hard disks of the data loggers. Tables 1 and 2 summarise some observational parameters.

station code	network	sensor, period in s	sampling rate in Hz
BFO	GRSN	STS-2, 120	20 / 80
STU	GRSN	STS-2, 120	20 / 80
TNS	GRSN	STS-2, 120	20 / 80
WLF	GEOFON	STS-2, 120	20
TM03	KABBA	LE-3D, 5	100
		STS-2, 120	
TM44	KABBA	GÜRALP, 30	100
		STS-2, 120	
TM45	KABBA	STS-2, 120	100
TM47	KABBA	LE-3D, 5	100
		STS-2, 120	

Table 1. Overview on seismological recording stations.

station code	net-work	parameter	sampling rate in Hz
1468	DWD	ws, wd, bp, T, pd	0.00167
2522	DWD	ws, wd, bp, T, pd	0.00167
2601	DWD	ws, wd, bp, T, pd	0.00167
4177	DWD	ws, wd, bp, T, pd	0.00167
3362	DWD	ws, wd, bp, T, pd	0.00167
4931	DWD	ws, wd, bp, T, pd	0.00167
5100	DWD	ws, wd, bp, T, pd	0.00167
FZK	FZKM	ws, wd, bp, T, pd, gs	0.00167
DURM	private	ws, wd, bp, T, pd, gs	0.0167

Table 2. Overview on meteorological recording stations. Parameters: ws: wind speed, wd: wind direction, bp: barometric pressure, T: temperature, pd: precipitation depth, gs: gust speed.

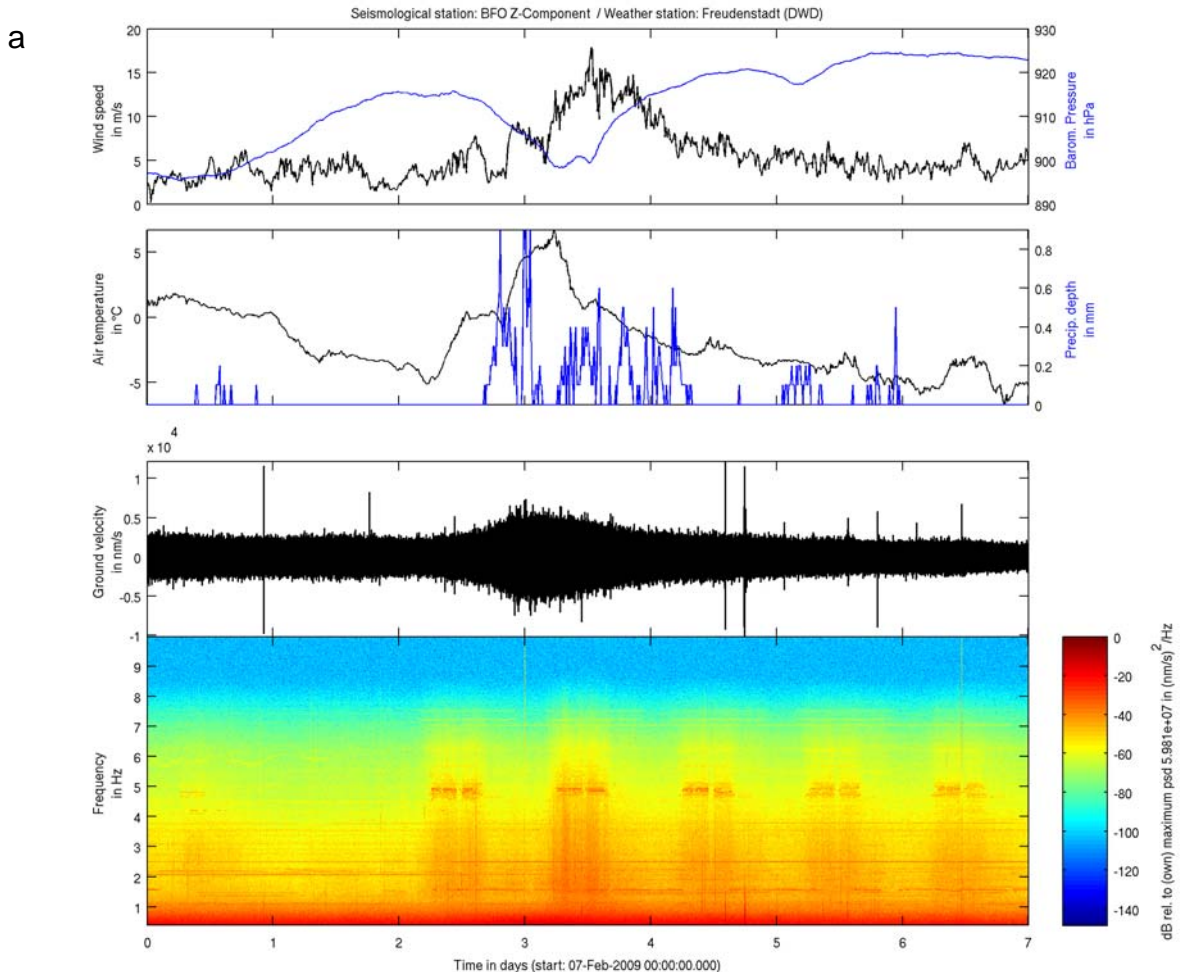
These eight observational sites allow us to discriminate METSEIS interaction at different local ground conditions and monitor time-dependent properties. Additionally we can make use of the seismological broadband recordings of the TIMO project (Tiefenstruktur des Mittleren Oberrheingrabens – Deep Structure of the Central Upper Rhine Graben). During the TIMO experiment 32 KABBA stations recorded continuously the seismic ground motion between December 2004 and May 2006 (Ritter et al., 2008), including

TM03, TM44 and TM45. These recordings will be used to determine spatial correlation lengths of the seismic noise recordings and their relationship to the weather parameters (Ritter and Groos, 2007).

Data Example

In Fig. 3a and 3b we show two examples with seismological and meteorological time series. The time series have a duration of one week (start time: Saturday 7th Feb. 2009) and contain the passage of winter storm Quinten which had its culmination on 10th February. On 12th Feb. a major earthquake (magnitude 7.2) below Kepulauan Talaud, Indonesia occurred and its far-field ground motion appears as relatively transient signal in these diagrams (at about day 4.75). There are also

other impulsive transient signals of mostly yet unknown origin in the time series. The seismological waveforms are high-pass filtered at 0.4 Hz and the spectrograms are composed of Fourier transforms in 120 s long time windows and 30 s step length. The data in Fig. 3 represent two different situations: In Fig. 3a a remote site in the Black Forest is selected (BFO) where the passage of the Quinten is clearly seen in the seismic waveform. On contrary at TM45 in the city of Karlsruhe the ambient noise is too high that Quinten does not leave a clear trace at 1-20 Hz (Fig. 3b). At TM45 the powerful anthropogenic noise is visible due to its clear day and night variation. At lower frequencies (e.g. oceanic microseisms) the result is different but this will be shown separately.



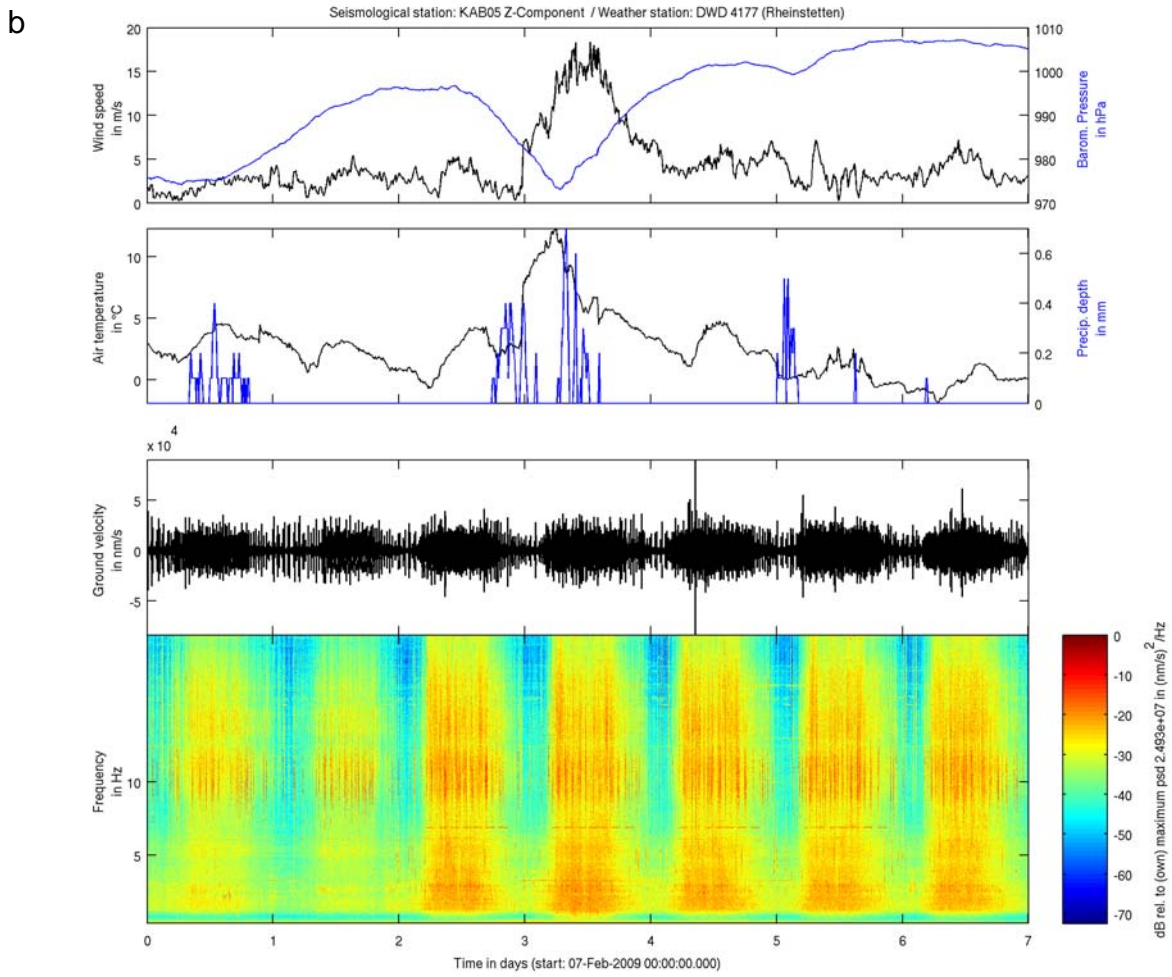


Figure 3. Time series with vertical ground motion and weather data at stations BFO and Freudenstadt in the Black Forest (a) and Karlsruhe (TM45) and Rheinstetten (b). The time is 7th-13th Feb. 2009, during days 2-3 the passage of winter storm Quinten occurred. In the early evening of day 4 a major earthquake below Indonesia occurred.

Acknowledgements

We thank P. Knopf, R. Plokarz, W. Scherer and H. Thomas for assistance with the measurements and/or data handling. METSEIS is financed by a KIT Start-Up-Budget grant (Karlsruhe Institute of Technology) and the Geophysical Institute of the Universität Karlsruhe (TH). Meteorological data were provided by the Deutscher Wetterdienst (DWD: stations 1468, 2522, 2601, 3362, 4177, 4931, 5100), Forschungszentrum Karlsruhe (FZK) and Wetterstation Durlach (Peter Wenner). Seismological data were provided by the German Regional Seismic Network (GRSN: BFO, STU and TNS) and the GEOFON network of the Deutsches GeoForschungsZentrum (GFZ: WLF).

References

- Aster, R.C., D.E. McNamara, and P.D. Bromirski, Multidecadal climate-induced variability in microseisms, *Seism. Res. Lett.*, 79, 194-202, doi:10.1785/gssrl.79.2.194, 2008.
- Berger, J., P. Davis, and G. Ekström, Ambient Earth noise: a survey of the global seismographic network, *J. Geophys. Res.*, 109, B11307, doi:10.1029/2004JB003408, 2004.
- Bonnefoy-Claudet, S., F. Cotton, and P-Y. Bard, The nature of noise wavefield and its application for site effects studies – a literature review, *Earth Sc. Rev.*, 79, 205-227, doi:10.1016/j.earscrev.2006.07.004, 2006.

- Bromirski, P.D., and F.K. Duennebier, The near-coast microseism spectrum: spatial and temporal wave climate relationships, *J. Geophys. Res.*, 107, doi:10.1029/2001JB000265, 2002.
- Curtis, A., P. Gerstoft, H. Sato, R. Snieder, K. Wapenaar, Seismic interferometry – turning noise into signal, *The Leading Edge*, 25, 1082-1092, 2006.
- Groos, J., and Ritter, J., Temporal and spatial changes of statistical properties in the urban seismic noise wavefield, *Geophys. Res. Abs.*, 10, 00313, 2008.
- Kurrale, D., and R. Widmer-Schnidrig, The horizontal hum of the Earth: a global background of spheroidal and toroidal modes, *Geophys. Res. Lett.*, 35, L06304, doi:10.1029/2007GL033125, 2008
- Parolai, S., and J.J. Galiana-Merino, Effect of transient seismic noise on estimates of H/V spectral ratios, *Bull. Seism. Soc. Am.*, 96, 228–236, doi:10.1785/0120050084, 2006.
- Peterson, J., Observations and modeling of seismic background noise, U.S. Geol. Surv. Open File Report, 93-322, 1993.
- Ritter, J.R.R., and J. Groos, J., Kyrills seismischer Fingerabdruck, *Spektrum der Wissenschaft*, März, 19, 2007.
- Ritter, J.R.R., M. Wagner, B. Wawrzinek, and F. Wenzel, Aims and first results of the TIMO project: Tiefenstruktur des mittleren Oberrheingrabens, *Geotect. Res.*, 95/1, 151-154, doi:10.1127/1864-5658/08/9501-0151, 2008.
- Sens-Schönenfelder, C., and U. Wegler, Passive image interferometry and seasonal variations of seismic velocities at Merapi volcano, Indonesia, *Geophys. Res. Lett.*, 33, L21302, doi:10.1029/2006GL027797, 2006.
- Shapiro, N.M, M. Campillo, L. Stehly, and M.H. Ritzwoller, High-resolution surface-wave tomography from ambient seismic noise, *Science*, 307, 1615-1618, doi:10.1126/science.1108339, 2005.
- Wilson, D., J. Leon, R. Aster, J. Ni, J. Schlue, S. Grand, S. Semken, S. Baldridge, and W. Gao, Broadband seismic background noise at temporary seismic stations observed on a regional scale in the Southwestern United States, *Bull. Seism. Soc. Am.*, 92; 3335-3342, doi:10.1785/0120010234, 2002.
- Zürn, W., Simplistic models of vertical seismic noise above 0.1 mHz derived from local barometric pressure, *Bull. Inf. Marées Terrestres*, 137, 10867-10874, 2002.

The Role of Modal Cross-terms in Seismic Interferometry

Wouter Kimman, Jeannot Trampert

Department of Earth sciences, Utrecht University, The Netherlands, E-mail: kimman@geo.uu.nl

The exact interferometric equation (Wapenaar 2004, van Manen 2006) gives the relation between the retrieved Green's function and signals arriving from an enclosed surface integral of sources (monopole and dipole sources).

$$G_{im}(x_B, x_A) - G_{im}^*(x_B, x_A) = \int_S G_{in}(x_B, x) \eta_j c_{ijkl} \partial_k G_{ml}^*(x_A, x) (1) \\ - \eta_j c_{ijkl} \partial_k G_{il}(x_A, x) G_{mn}^*(x_B, x) \} dS(x)$$

This relation is exact for the full wavefield, even for complicated lossless media. If, however, only monopole sources are assumed, as needs to be done for all practical cases, retrieval can be imperfect in heterogeneous media.

For individual Rayleigh wave modes, the interstation Green's function can be written in terms of displacements resulting from a combination of horizontal and vertical monopole sources scaled by the group velocity (Halliday and Curtis 2008)

$$G_{im}(x_B, x_A) - G_{im}^*(x_B, x_A) = \\ -2i\omega U \int_S \rho G_{ip}(x_B, x) G_{mp}^*(x_A, x) dS \quad (2).$$

The most important assumptions made in this derivation are:

- Green's functions are single Rayleigh wave modes.
- Sources extent to infinite depth or at least to the depth where the eigenfunctions become small.
- There is a full azimuthal coverage of sources, meaning that the receivers are illuminated equally from all directions.
- Far field approximation. When sources are close this approximation results in a small frequency dependent amplitude error.
- Sources are not correlated or act consecutively. They are delta sources or have the same source signature.

In figure 1 we compare the match between the direct and the retrieved Green's function by

point forces on a surrounding source surface, subsequently fired in the x, y and z direction. Wheras relative amplitude errors can be expected, the spurious arrival is suprising.

We made an approximation to the exact equation similar to equation (2), but can in such a manner explicitly compute the modal cross-terms, as well as the retrieval of the individual modes. Indeed computed in this way, we can identify the imperfections in retrieval and attribute these to cross terms.

Figure 2 shows the application of the single point force approximation on the full wavefield, as computed by (surface wave) modal summation. We attribute the noisy background to cross-terms, after explicitly computing them (figure 2, green). Even though they are small, one should recognize that all other necessary conditions for retrieval (source distribution etc) are perfect. If for example sources are present at the free surface only, the cross term level increases and overwhelm higher modes.

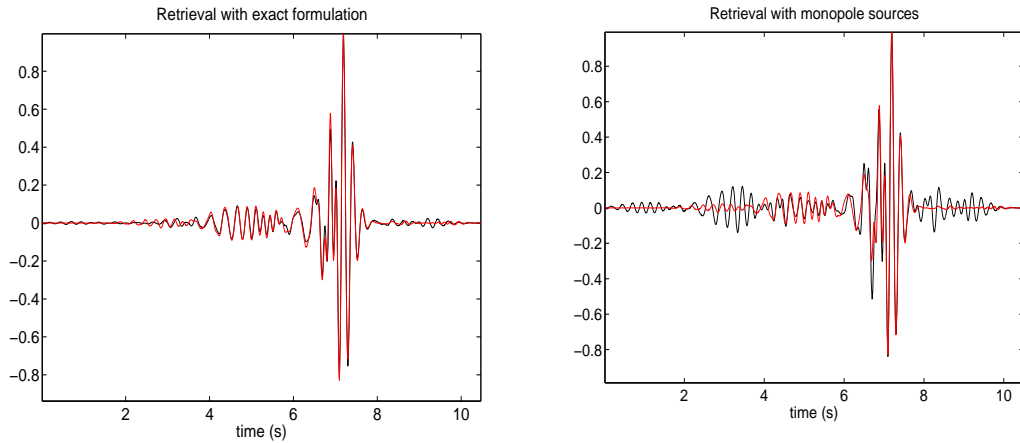


Figure 1. Green's function retrieval for a layered model, using the exact formulation (equation 1) on the left, versus the result using 3 orthogonal point forces only (equation 2) on the right. Sources are placed at a far-field distance in a perfect surrounding surface, except at the free surface (Wapenaar, 2004) with respect to the two receivers.

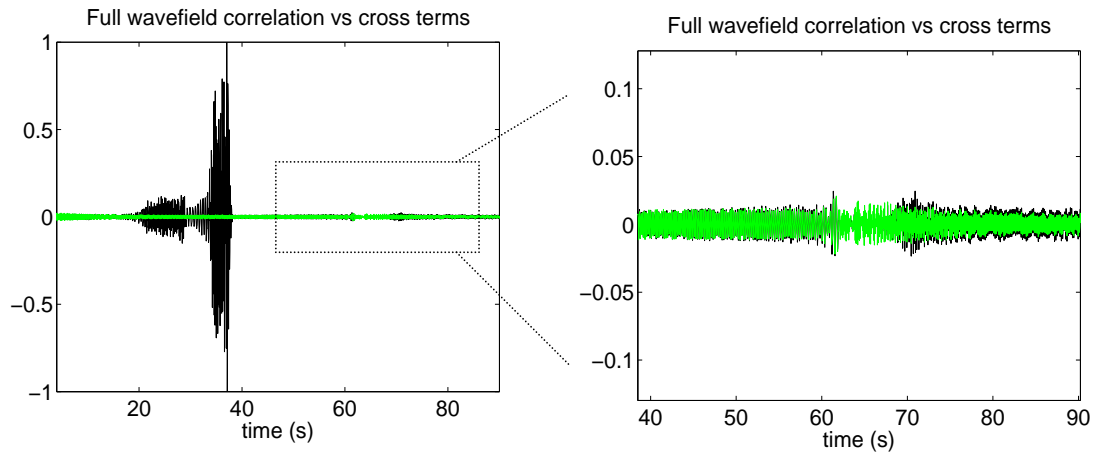


Figure 2. The application of the point force approximation to the full wavefield, this time computed by mode summation. The retrieved Green's function contains a noisy background. In green the computed cross term interactions. (The right figure shows a zoomed version of the box in the figure to the left.)

References

Halliday D. and Curtis A. [2008] Seismic interferometry, surface waves and source distribution. *Geophysical Journal International*, 175, 1067–1087

van Manen, D., Curtis, A., & Robertsson, J.O.A. [2006] Interferometric modelling of wave propagation in inhomogeneous elastic media using time-reversal and reciprocity. *Geophysics*, 71(4), SI47–SI60.

Wapenaar, K., 2004. Retrieving the elastodynamic green's function of an arbitrary inhomogeneous medium by cross correlation, *Phys. Rev. Lett.*, 93, 254301

Seismic Interferometry by cross-correlation and by multi-dimensional deconvolution using ambient seismic noise

Deyan Draganov, Elmer Ruigrok, Jan Thorbecke, Jürg Hunziker, Joost v.d. Neut, Kees Wapenaar

Delft University of Technology, Department of Geotechnology, Stevinweg 1, 2628 CN Delft, The Netherlands. E-mail: d.s.draganov@tudelft.nl

When applying seismic interferometry (SI) by cross-correlation (CC), one assumes a known or regular source distribution. For applications in the field this condition will not be easily fulfilled. For this reason, one can make use of SI by multi-dimensional deconvolution (MDD) (Wapenaar et al., 2008). This method makes use of matrices, where a row of a matrix contains responses for a fixed receiver position and variable source positions. The Green's function is retrieved using a matrix inversion. An advantage of the MDD method is that it can compensate for irregular distribution and strength of the sources. An additional requirement of this method is that the data to be inverted need to be recorded along a wide-aperture well-sampled receiver array. Contrary to this, SI by CC can be performed with recordings even at only two receivers. Wapenaar et al. (2008) show the advantage of SI by MDD over SI by CC using numerical-modelling for acoustic fields when separate recordings are available at the receivers from each of the (passive) seismic sources.

When one wants to apply SI with ambient seismic noise, i.e., when no separate recordings at the receivers are possible from each of the passive seismic sources, then the matrices in the relation of SI by MDD will collapse to column vectors as each row will contain only one recording. We investigate SI by MDD with ambient noise with the help of numerical-modelling examples. We model surface waves propagating in a layered elastic medium. We first compute a dispersion curve for the upper 300 km of the PREM model (Dziewonski and Anderson, 1981) using an approach as described in Wathelet et al. (2004). Next, we forward-model fundamental

Rayleigh waves based on the computed dispersion curve. The configuration that we use is shown in Figure 1. We use 150 simultaneously acting white-noise sources, represented by the blue stars, with an irregular distribution. In particular, we use two clusters of noise sources – the first one is concentrated around $x_2=30$ km and consists of 20 sources, while the second is concentrated around $x_2=-100$ km and consists of 30 sources. We record the emitted noise fields at two mutually perpendicular receiver arrays, which in the figure are represented by the green triangles. Array 1 is parallel to the source-distribution geometry and contains 129 receivers spaced at 2.5 km. Array 2 contains 16 receivers spaced at 20 km. The frequency spectrum of the noise sources peaks at 0.2 Hz, which is the double-frequency microseismic peak. The two arrays record the total noise for nearly 42 hours.

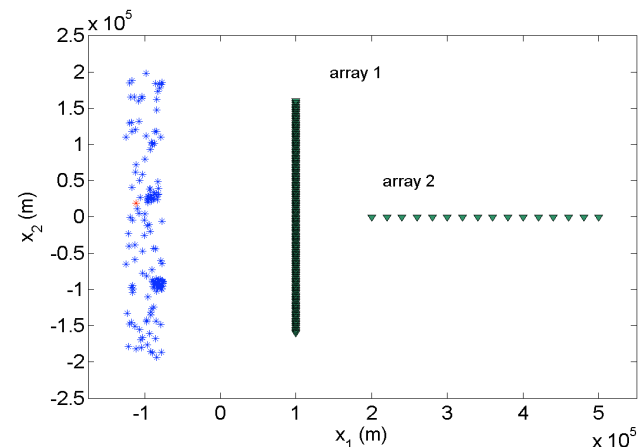


Figure 1. Acquisition configuration used for numerical modelling. There are 150 sources (the blue stars) and 2 mutually perpendicular arrays of receivers (the green triangles).

We choose to retrieve surface wave information as it would be recorded along array 2 in the presence of a virtual source at the position of the receiver with $x_2=0$ km in array 1. We first do this using SI by CC. We extract the noise trace at the chosen virtual-source position from array 1 and correlate it with all the noise traces from array 2. We then use SI by MDD to retrieve the same information. For this, though, we need all noise traces from array 1. MDD is a much slower process than CC. The computational time, though, can be made more acceptable if the noise traces are split into shorter noise windows. These noise windows are then arranged in matrices, which are then used instead of the two noise vectors recorded along the two receiver arrays. The MDD method is applied by least-squares inversion. In Figure 2 we show the amplitude spectrum of the virtual-source gathers along array 2 obtained using CC (top) and MDD (middle). At the bottom of Figure 2 we show for comparison the amplitude spectrum for a reference active-source gather. We see that the SI by CC has done a good job in retrieving the general character of the dispersive surface waves. Nevertheless, we see the amplitude spectrum has a gap at lower frequencies and that the peak is slightly shifted to a higher frequency, namely to 0.3 Hz. These problems are consequences from the irregular source distribution. Comparing the result obtained using SI by MDD with the reference response, we see that the MDD process has corrected for the discrepancies – the spectrum is less distorted and more continuous.

Figure 3 shows the comparison between the virtual-source gather retrieved using SI by CC, shown in red, and the reference active-source gather, shown in black. We can see that the CC retrieves the moveout and dispersion character of the surface wave. On the other hand, we see that the waveform is incorrectly retrieved – there are strong artefacts before the onset. These artefacts result from the cluster in the noise-source distribution that is concentrated around $x_2=30$ km. This cluster is situated in the stationary-

phase region for the virtual source at $x_2=0$ km in array 1 and the receivers in array 2 and causes overillumination of that part of the region.

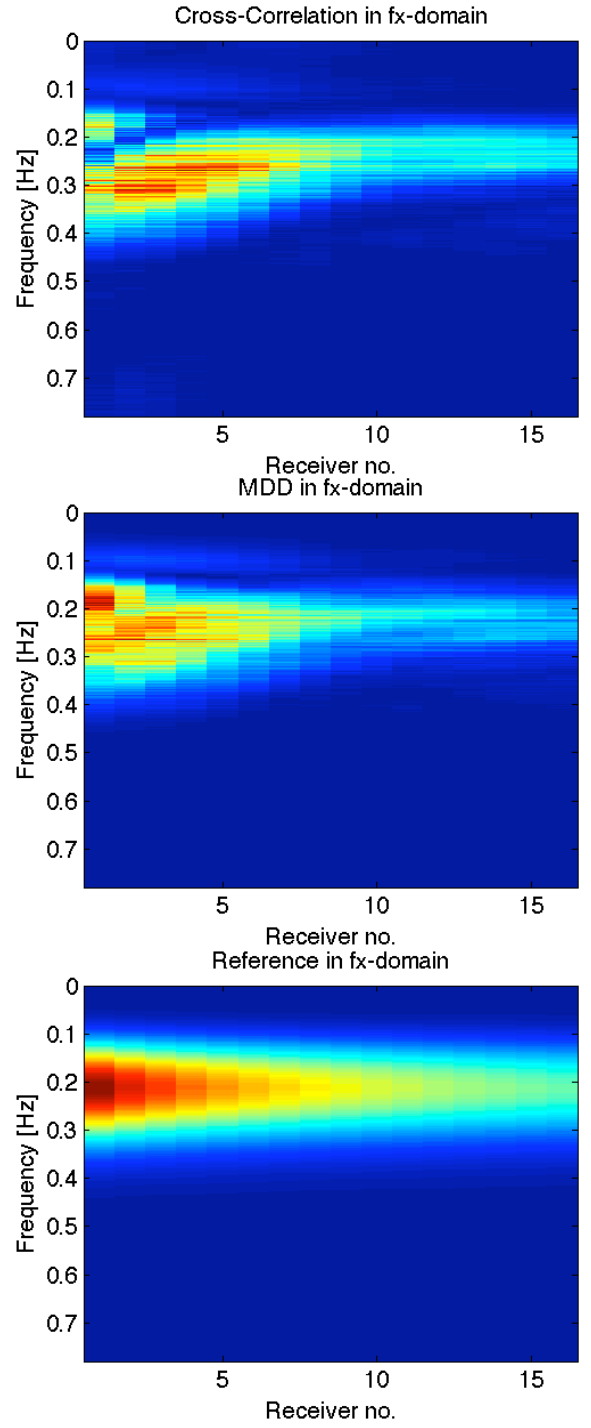


Figure 2. Frequency spectrum of the virtual-source gathers obtained using SI by CC (top) and SI by MDD (middle). A reference active-source gather is shown at the bottom.

In Figure 4 we show the comparison between the virtual-source gather retrieved using SI by MDD, shown in red, and the reference active-source gather, shown in black. We can see

that the MDD process has retrieved not only the kinematics, but also has corrected for the overillumination due to the source cluster around $x_2=30$ km – the artefacts before the onset are largely compensated for and consequently suppressed.

In conclusion, we showed the application of SI by CC and by MDD to ambient seismic noise. Due to irregular distribution of the noise sources, some artefacts might arise in the CC result. SI by MDD could compensate for the irregular source distribution and suppress such artefacts.

References

- Dziewonski, M. and D. L. Anderson, 1981, Preliminary reference earth model: Physics of The Earth and Planetary Interiors, **25**, 297–356.
- Wapenaar, K., J. van der Neut, E. Ruigrok, D. Draganov, E. Slob, and J. Thorbecke, 2008, Seismic interferometry by cross-correlation or deconvolution?: 78th Annual International Meeting, SEG, Expanded abstracts, 2731-2736.
- Waitelet, M., D. Jongmans and M. Ohrnberger, 2004, Surface-wave inversion using a direct search algorithm and its application to ambient vibration measurements: Near Surface Geophysics, **2**, 211-221.

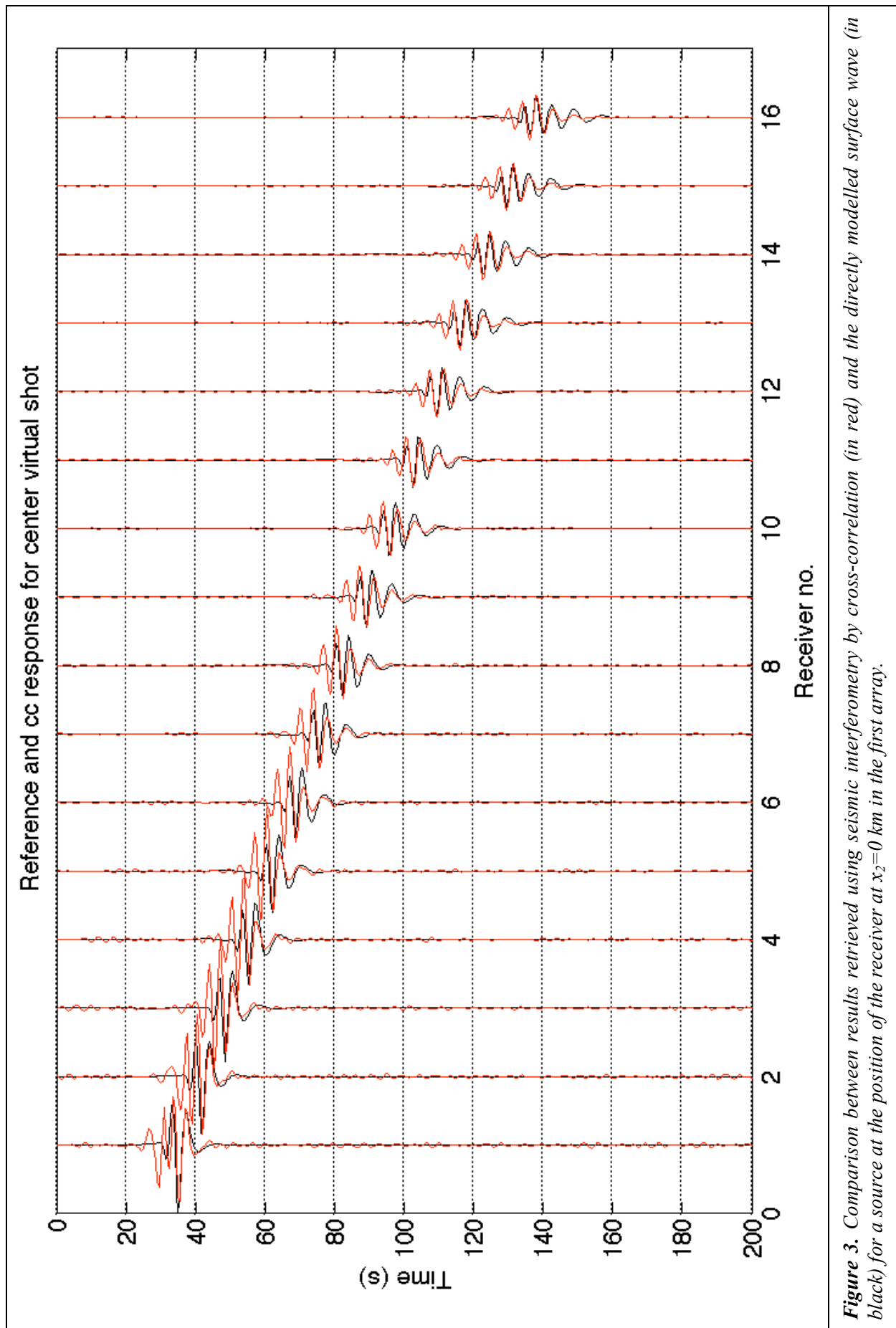


Figure 3. Comparison between results retrieved using seismic interferometry by cross-correlation (in red) and the directly modelled surface wave (in black) for a source at the position of the receiver at $x_2=0$ km in the first array.

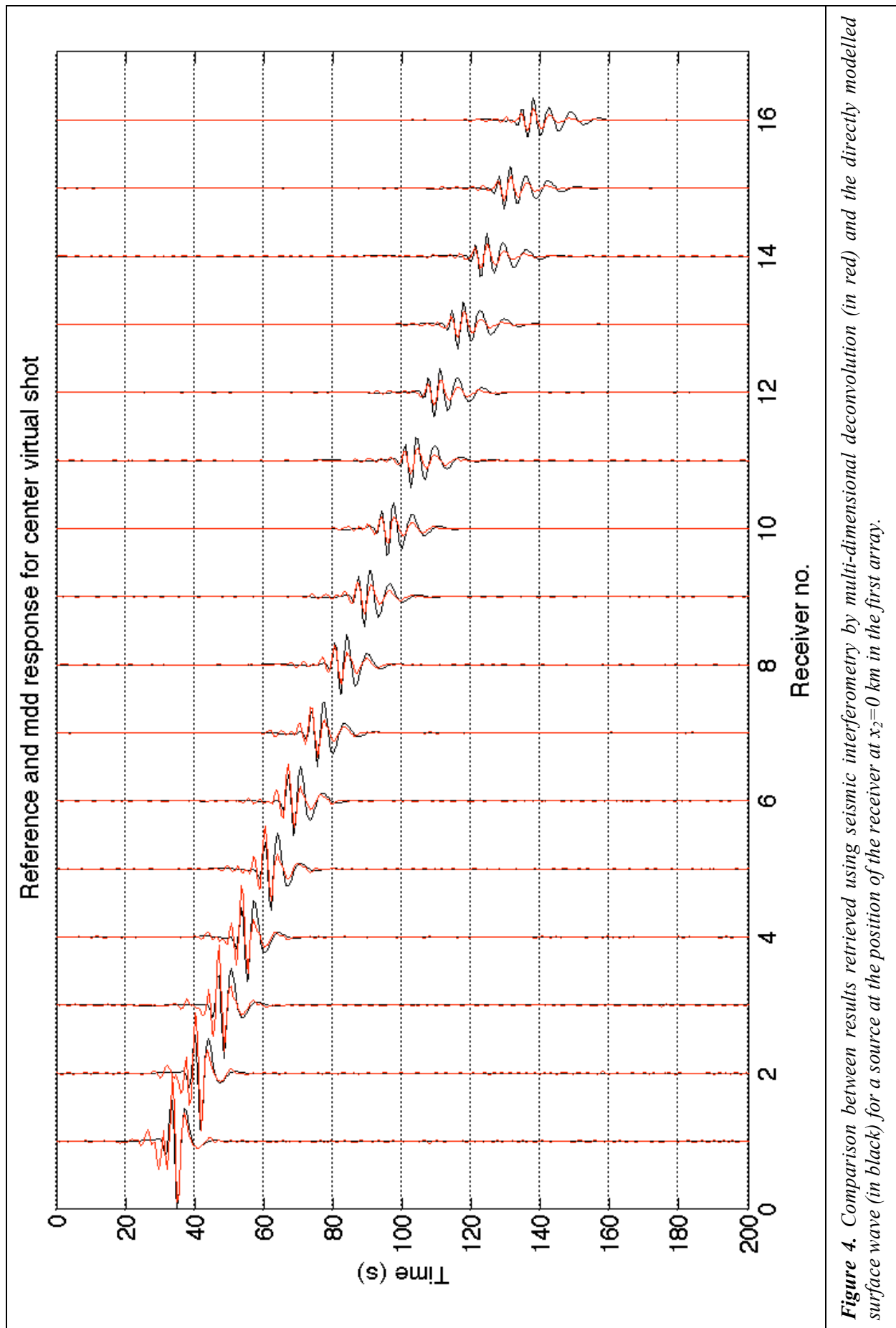


Figure 4. Comparison between results retrieved using seismic interferometry by multi-dimensional deconvolution (in red) and the directly modelled surface wave (in black) for a source at the position of the receiver at $x_2=0$ km in the first array.

What can we learn from Greens function retrieval from ambient noise in the frequency range 1 to 10 Hz?

Michael Korn

Institute of Geophysics and Geology, University of Leipzig, Germany, E-mail: mikorn@uni-leipzig.de

Introduction

It has been well established theoretically that the cross correlation of a diffuse wave field between two seismic stations is equivalent to the Green's function, i.e. to the wave field generated by a point source at one of the receivers and recorded at the second. Ambient seismic noise from distributed sources at the Earth's surface is often assumed to be sufficiently similar to such a diffuse wave field so that the Green's function can be retrieved from continuous recordings of the noise. This has opened a new way for structural imaging without the need of active sources, e. g. for surface wave tomography, and it has a wealth of other possible applications like Passive Image Interferometry to monitor variations of structure or seismic velocities with time. It has been successfully used in detecting velocity changes associated with damage in the fault zone of earthquakes, volcanic eruptions, or structural weakening. The most successful applications so far have been on the continental scale using long-period surface waves, and on small-scale imaging of structural changes with high-frequency waves.

There is a number of issues that need further investigation before it should be used as a routine tool, e.g. to what extent the assumption of ambient noise as a diffuse wave field is valid in different frequency and distance ranges. Another point of interest is what amount of reliable and stable information is contained in the reconstructed Green's functions. Short period waves (1-10 Hz) are of special interest in this context as they are effectively scattered within the crust, and may be used in the context of passive image interferometry e.g. in fault zones.

Data

In this study I used ambient noise data from the short period vertical sensors of the NORSAR array, southern Norway. The array consists of 7 subarrays with 6 receivers within each subarray. They are well suited as a test data set as they have high data quality and long time availability in a region where the crustal structure is fairly well-known, and no time variations are expected. Continuous data sampled at 40 Hz have been used. Normalized cross-correlations (CCF) were computed for 24h traces and stacked for up to 90 days. Inter-receiver distances vary between several km within one subarray, and some tens of km for the whole array.

Results

Stacked traces clearly show the Rg wave (Fig. 1), its velocity being consistent with what is expected from the crustal structure under NORSAR. Their amplitudes at positive and negative times strongly depend on the azimuth of observation (Fig. 2). This amplitude pattern is consistent with a dominant noise source from a certain azimuth plus a significant amount of secondary scattered waves coming in from various directions. This points to the fact that oceanic microseism forms the most significant primary source of ambient noise below 2 Hz, having a strong azimuth and time dependence and clearly deviating from a diffuse wave field. Nevertheless the crustal scattering is strong enough to provide an azimuthal averaging that allows the retrieval of the Rg phase, but not of the amplitude information. Above 2 Hz the Rg arrival breaks down for distances above 10 km, indicating that there are no noise sources at these frequencies that

are strong enough to correlate over more than a few kilometers.

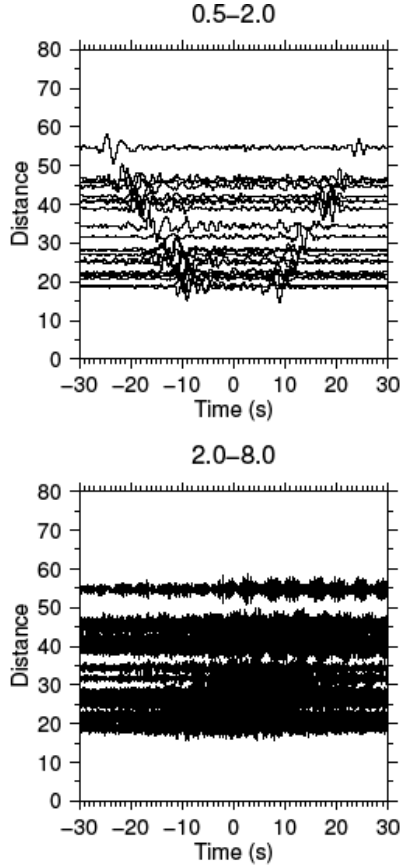


Figure 1: 60 days stacked CCF traces across subarrays.
Top: 0.5 – 2 Hz with clear Rg waves travelling at 2.5 km/s.
Bottom: Above 2 Hz no coherent energy is detected.

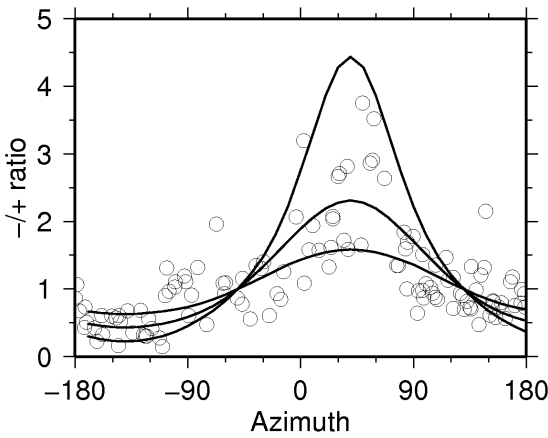


Figure 2: Ratio of Rg wave amplitudes at positive and negative times. The strong azimuthal pattern is explained by the main direction of incoming waves from W to WSW azimuths with a considerable amount of scattered waves from other azimuths. Solid lines are theoretical fits for various azimuthal distributions of ambient noise (after Nakahara, 2006).

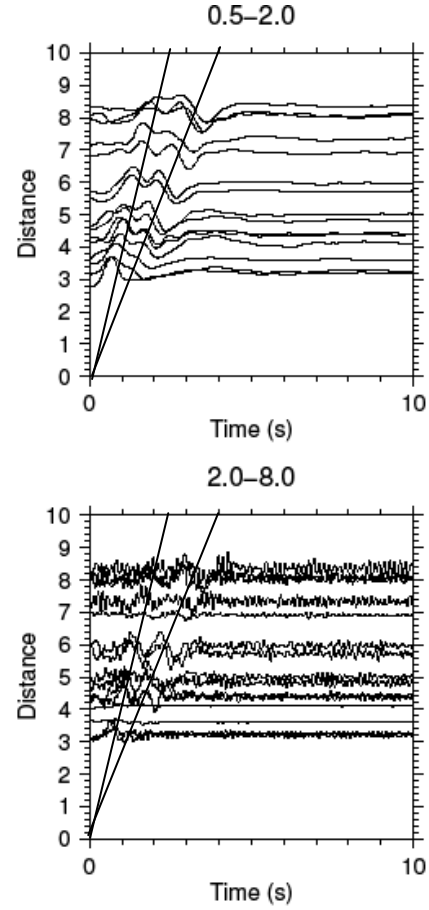


Figure 3: 90 days stacked CCF traces over one subarray. Negative and positive times have been mirrored and stacked.
Top: At 0.5 – 2 Hz Sg body waves and Rg surface waves can be identified.
Bottom: Above 2 Hz signal to noise ratio becomes worse.

CCFs within one subarray show a clear body wave phase (Sg) travelling with about 3.8 km/s (Fig. 3). This phase deteriorates above 2 Hz. Several partly coherent phases can be identified within the coda after Rg. However, they are not stable with time and depend on the noise sources.

Conclusions

Rayleigh waves are easily retrieved from ambient noise in the frequency range up to 2 Hz for distances to 80 km.
Body waves (S waves) can be identified only up to a receiver distance of about 10 km.

No clear coherent coda wave arrivals could be identified.

Below 2 Hz main sources of ambient noise have preferred propagation direction consistent with marine microseisms, but are scattered into a broad range of azimuths. There are significant variations of ambient noise wavefield with time due to variations in meteorological conditions.

Above 2 Hz there is no clear correlatable energy at distances above 10 km, i.e. ambient noise changes its characteristics at about 2 Hz. We speculate that ambient noise above 2 Hz is mainly generated by local sources with low energy that does not propagate for distances more than a few km. This may be a feature of the NORSAR array that has been built in a low noise environment and may be different at sites that are more contaminated by industrial noise.

As a general result from this test we conclude that the success of Green's function retrieval and its applications depends strongly on the properties and time stability of the ambient noise. Strategies for routine checking these properties should be developed.

References:

- NAKAHARA, H., 2006. A systematic study of theoretical relations between spatial correlation and Green's function in one-, two- and three-dimensional random scalar wavefields, *Geophys. J. Int.*, 167, 1097-1105.

A study of ambient seismic noise as the source for body-wave interferometry

Xander Campman¹, Deyan Draganov², Arie Verdel¹ and Kees Wapenaar²

¹ Shell International Exploration and Production B.V., Kessler Park 1, 2288 GS, Rijswijk, The Netherlands E-mail: xander.campman@shell.com

² Department of Geotechnology, Delft University of Technology, Stevinweg 1, 2628 CN, Delft, The Netherlands, E-mail: d.s.draganov@tudelft.nl

One application of seismic interferometry is the extraction of Green's functions from ambient noise. Theory tells us that if uncorrelated noise sources illuminate the recording stations from all directions and if the noise can be characterized as a random process, then the complete Green's function, including the body-wave reflection response and surface waves, is retrieved from a crosscorrelation-and-summation operation (Wapenaar, 2004). Fixing one receiver at a time, correlating the trace from that receiver with every other trace, and summing over the recording time, a virtual source is synthesized at the fixed receiver location and recorded by the other traces. If the noise is generated mainly by sources at or close to the Earth's surface, then only the surface-wave part of the Green's function can be extracted with the crosscorrelation-and-summation operation. The latter is the case, for example, in many global and regional studies of surface-wave tomography with ambient noise when energy in the primary and double-frequency microseism bands, approximately between 0.07 Hz. and 0.5 Hz., is used for correlations. While many papers show successful application of ambient seismic noise-interferometry for surface waves several issues remain with this method. One of the main problems is related to the spatial distribution of the noise sources (Yang and Ritzwoller, 2008) that synthesize the virtual source. It is well known that an uneven illumination causes a directionally biased Green's function (Paul et al., 2005), or even unphysical events.

All energy registered by receivers is potentially input for the crosscorrelation-and-summation process, synthesizing the virtual source. By manipulating this energy (for

example by bandpass filtering or time-windowing), one can manipulate the virtual source. For example, rather than looking at continuous noise records, one could select deterministic events (Yao et al., 2009) or select coda energy (Paul et al., 2005). The advantage of this approach is that the distribution of deterministic events is easier to evaluate. In certain cases, the impact on the crosscorrelation result may even be predicted (Ruigrok et al., 2009). The approach in Ruigrok et al. (2009) bears resemblance to the virtual-source method, as developed in the seismic exploration industry (Bakulin and Calvert, 2006). In the virtual-source method, however, one can optimize the source distribution along the surface to create a desired virtual source. When using continuous noise sources, this is practically unfeasible.

In seismic exploration, one is particularly interested in body-wave reflections, as they provide the highest resolution images of potentially hydrocarbon bearing structures. However, the extraction of body-wave reflections using ambient-noise interferometry has turned out to be much more challenging than the extraction of surface waves from noise. This is in part due to the longer propagation paths between the receivers (and the higher rate of geometric spreading), the more severe restrictions on the distribution of sources for the retrieval of body waves (as pointed out by Wapenaar, 2004, for the retrieval of reflections, sources should be located in the subsurface) and the fact that omnipresent surface-wave noise dominates the generally weaker body-wave noise. In fact, for body waves it is less clear whether any (continuous) noise sources contribute to the synthesis of Green's

functions and if any, what are the source mechanisms and distributions.

Most studies on noise observations agree that the bulk of the noise recorded at the surface of the Earth consists of fundamental- and higher-mode surface (Rayleigh) waves. Nevertheless, comparisons of spectra measured at the surface and in boreholes also permit the alternative explanation of (standing) body waves (Gupta, 1965, Sheriff et al., 1965, Douze, 1967). Only very few studies have observed directly and with confidence the presence of body waves in noise. If any, they appeared to be relatively low-frequency body waves, probably excited by oceanic microseisms (Toksöz and Lacoss, 1968). In the frequency band of interest for seismic exploration (> 1 Hz), these observations are particularly rare.

Nevertheless, at the hand of an example with data recorded in a relatively quiet area, Draganov et al. (2007) showed it was possible to extract body-wave reflections from ambient seismic noise. Because of the specific acquisition geometry used in this experiment, it was only possible to confirm the possible presence of body waves in the raw noise records by examining the polarization of vertically traveling waves (Draganov et al., 2006).

The experiment was repeated on a much larger scale using a 3-D exploration-seismic acquisition spread by Shell in Libya (SEPLG) in 2007. The extent of the entire array on which the noise was simultaneously recorded allows more flexibility in spatial processing. In addition, it allows us to take advantage of the specific geophone-group geometry as it was designed to enhance body waves while suppressing surface waves at specific wavenumbers (as already suggested by Baskir and Weller, 1975). Draganov et al. (2009a,b) applied seismic interferometry and standard seismic processing to these data to extract seismic reflection images from ambient noise.

In this abstract we discuss work in progress on the characterization of roughly 11 hours of ambient seismic noise recorded on approximately 3000 receiver channels during an exploration survey in the Sirte Basin, East of Ajdabeya in Libya. We pay particular

attention to the composition of the noise wavefield and its implications for body-wave interferometry.

Survey geometry and data

In September 2007, Shell recorded approximately 11 hours of ambient seismic noise during an exploration survey in the Eastern part of the Sirte Basin near Ajdabeya in Libya. The recording geometry is shown in Figure 1.

Libya is not generally considered an active seismic area, although several large earthquakes have occurred in the past. The most active part is the Eastern flank of the Hun graben, on the western part of the Sirte Basin. The eastern part of the basin is quieter, with no activity in the basin itself (Suleiman and Doser, 1995). The Cyrenaica platform – to the NE of the survey area -- is also an area of recent seismicity. Not much is known about the specific characteristics of ambient seismic noise in Libya, since only few seismometers have been deployed in the past.

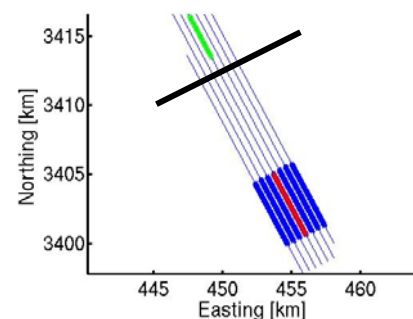


Figure 1. The geometry of the passive survey (thin lines) and approximate location of the road. Parts of the recording spread used for frequency-wavenumber analysis are indicated by the fat blue lines and red and green crosses.

The recording equipment used in this survey, consisted of groups of standard 10 Hz vertical-component geophones and a Sercel 304S recorder. The channels on the line were connected to patterns consisting of 48 geophones. These patterns are designed to suppress the surface wave generated by the vibrator in active seismic surveys, while passing body-wave reflections with much higher apparent velocities.

Unfortunately, the equipment does not allow a full characterization of the ambient noise below a few Hz. Because of this, we have not attempted to quantify the noise in terms of absolute displacements and compare them with the standard noise models. The geophone response of a standard 10 Hz geophone is usually not adequate to record very low-amplitude signals because of 1) its relatively low sensitivity and 2) the 12 dB/Oct decay below 10 Hz.

Nonetheless, we see a strong response down to about 1 Hz. This can partly be attributed to the fact that for each geophone station, the 48 geophones from the pattern are summed together, thereby boosting the signal. Also, the double-frequency microseism starts to ramp up at the low-frequency end.

Noise at short periods is usually attributed to local conditions such as atmospheric conditions and human-generated noise. In our case, a traffic road intersects the survey area, generating strong surface-wave noise. Figure 2 shows the power spectral density (PSD) estimates for all traces along a line in the middle of the survey area. These spectra were calculated using Welch's method. We used approximately 2 hours of noise split up in 47 s windows (the record lengths) with 50 % overlap. Most of the noise is concentrated below approximately 6 Hz. The road can be identified by an increase in amplitude of the noise, which is evident especially at the frequencies up-to about 20 Hz, around 14 km along the line.

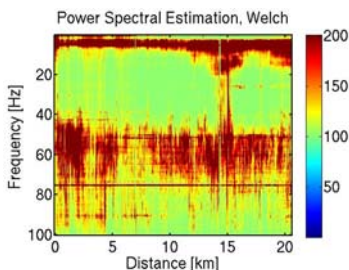


Figure 2. PSD of continuous noise for each receiver station along one line in the survey.

In order to investigate the directionality of the noise, due to the presence of the road, we determine frequency-wavenumber (FK) spectra. Because the crossline sampling of the array is not sufficient to obtain an unbiased two-dimensional FK spectrum for

the expected low surface-wave velocities, we determined the one-dimensional FK spectra on either side of the road (Figure 3). The estimated FK spectrum essentially shows the spatial correlation of the noise. The left panel of Figure 3 is the FK spectrum for the part of the line indicated with the red crosses in Figure 1. Considering the negative wavenumbers, the energy comes from the North. The right panel shows the FK spectrum for the part of the line indicated by the green crosses. The wavenumbers are positive indicating the energy propagates to the North. This confirms that the main source of energy is indeed the road. The spread in apparent velocities in these spectra can have two reasons: 1) frequency-dependent velocities (dispersion) and 2) energy arriving at the receiver line from directions other than along the line connecting the receivers. In the next section, we use this energy as the source for surface-wave interferometry.

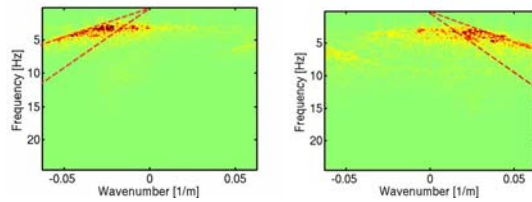


Figure 3. FK spectrum of the noise on the left side of the road and the right side of the road. For reference, the red lines indicate velocities between approximately 500 m/s and 1200 m/s.

Surface waves from noise

Our goal is to apply seismic interferometry to the data, with an emphasis on extracting possible body (P) wave reflections. Wapenaar and Fokkema (2006) derive a representation that expresses the Green function as a sum of correlations of observed traces. As stated in the introduction, we extract a virtual-shot record by fixing one trace and correlating this trace with other traces (along a line, or between lines) and summing the resulting correlograms. We first apply this processing to the data in the frequency band 2 to 25 Hz.

The result is shown in Figure 4. Because of the uni-directionality of the noise (see previous paragraph), we added the anti-causal Green's function to the causal part. It is

clear that a strong surface wave dominates this record. In Figure 4 we also show the dispersion curve extracted from the passive data, combined with the dispersion curve extracted from the active data. The passive part (below 5 Hz) shows good agreement with velocities obtained in the FK spectra in the previous section. The combined curve shows the velocities from the active and passive dispersion curves match well. Note that the active part of the dispersion curve is severely degraded due to the use of the geophone patterns, which are aimed at suppressing surface waves. The (combined) dispersion curve can be inverted to extract depth-dependent velocity profiles or can be used in surface-wave tomography.

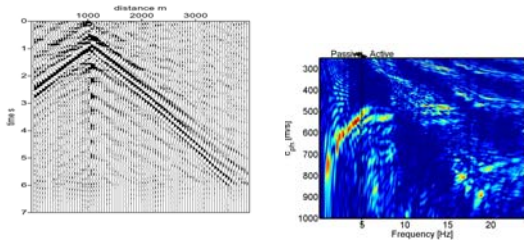


Figure 4. Surface wave extracted from noise (anti-causal and causal part summed) and dispersion curve extracted from the record.

So far, this demonstrates that we can use the surface-wave noise to extract information about the shallow subsurface. In the next section, we examine what energy contributes to the synthesis of the body-wave Green's function and show a virtual source record containing reflections extracted from the noise.

Body wave reflections from ambient noise

The panel on the left-hand side (LHS) of figure 5 shows a representative record of continuous noise after band-pass filtering to suppress the main surface-wave noise. Apart from some remaining surface-wave noise (the inclined events), there does not appear to be any other coherently aligned energy. In order to extract reflections with seismic interferometry, theory tells us we should have noise sources radiation from the deeper subsurface. Hence, we need (nearly) vertically travelling energy. Even if this energy were present in the continuous noise, we would

have to stack over very long recording times to be able to extract such weak coherent energy. Since we only have 11 hours of recordings available, we can also opt for an alternative approach and search the noise-records in more detail for visually discernable ‘events’, travelling nearly vertically. The right-hand side (RHS) panel of Figure 5 shows part of a band-pass filtered record with such an event. Only part of the receiver line indicated by the thicker lines in Figure 1 is shown here. In order to compare the composition of the first panel to the second, we first calculate the power spectrum of the record with ‘event’ and the spectrum of two hours of noise records (which could include events). Figure 6 shows the spectrum of two panels with events and the average spectrum of 2 hours of noise. The frequency bands are not very different, but distribution and amplitude of the energy is significantly different for the events. In order to further characterize these events, we form their FK spectra using beamforming.

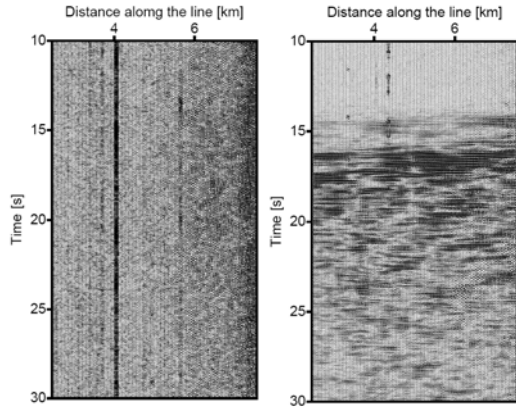


Figure 5. Records along the same part of one receiver line. The left-hand side panel shows part of the continuous noise. The right-hand side panel shows an isolated ‘event’.

At low wavenumbers, the array indicated by the fat blue lines in Figure 1, produces a reliable FK spectrum, as shown for a plane wave with apparent velocity of 8.5 km/s and back-azimuth 30 degrees in the RHS of Figure 6. The FK spectrum is shown in a polar plot with slowness along the radius and back-azimuth along the circumference. Figure 7 shows the FK spectra of two actual events. The slowness range in the plot is $\sim [5e-5 \text{ to } 3.3e-4] \text{ s/m}$. The high apparent velocities

correspond to upcoming body waves. It is as yet unclear what is the origin of these waves, but with the analysis of more events and investigating the directions of approach, we hope to be able to say something about their origin.

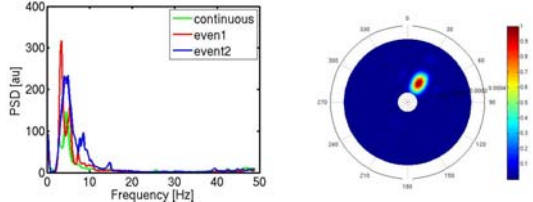


Figure 6. Spectrum of approximately 2 hours of continuous noise (green line), and of 2 isolated events (red and blue lines). All spectra were averaged along the line between receiver station 50 and 150.

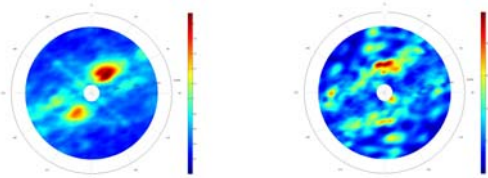


Figure 7. FK- power spectrum for the ‘event’ shown in Figure 6 (bottom), summed over the frequency band [3 10] Hz. The spectrum clearly shows a plane wave with apparent velocity of approximately 8.7 km/s. The right panel shows the FK spectrum of another ‘event’. The apparent velocity of this event is approximately 7.5 km/s.

Correlating and summing all noise records (11 hours), results in the record shown on the LHS of Figure 8, with the virtual source at 1 km. The right panel shows a record from the active survey with the active source at the same location. (Note that some shot processing has been applied to both records to remove remaining surface waves, for example.) Several hyperbolic events coincide, showing we have extracted body wave reflections. Currently, we are extracting all ‘events’ and plan to correlate only the records with such events. We expect that the body wave reflections will be better resolved this way.

Conclusions

We investigated some properties of seismic noise recorded for 11 hours in the eastern part

of the Sirte basin in Libya. The bulk of the energy in the noise is composed of surface waves at frequencies below 5 Hz. Using this part of the noise for interferometry results in the extraction of surface waves with velocities that match well with the velocities extracted from the active dispersion curve.

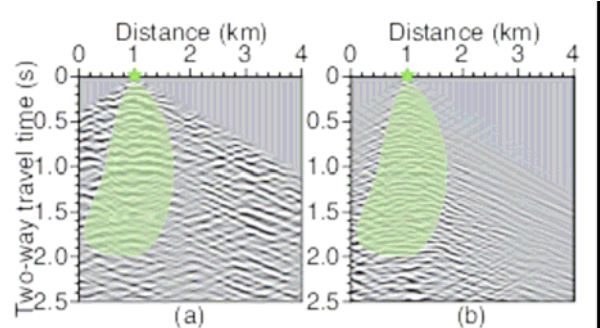


Figure 8. The left panel is a virtual shot record obtained from ambient seismic noise. The right panel shows the shot record from an active source at the same location.

Correlating 11 hours of filtered noise records results in the extraction of shot records containing body-wave reflections that coincide with reflections in an active shot record. From a more detailed analysis of the noise, we identified several records containing coherent energy traveling nearly vertically. FK analysis of these events show that they have very high apparent velocities, corresponding to upcoming body (P-) waves. Current work is focused on further characterizing these events. We will also selectively correlate the noise using only the ‘events’. We expect this will enhance the body-wave reflections in the virtual-shot records. Characterization of the events will allow us to evaluate the effects of their distribution on the resulting virtual-shot records.

Acknowledgements

D.D. is supported by the Technology Foundation STW, applied science division of NWO (project 08115) en Shell Int. E&P B.V. We thank SEPLG (Erik Kleiss, Rian de Jong and Alan Smith) and the Libyan National Oil Corporation for releasing the data and for permission to publish the results.

References

- Bakulin, A. and R. Calvert, 2006, The virtual-source method: theory and case study, *Geophys.*, 71, SI139-SI150.
- Baskir E. and C. Weller, 1975, Sourceless reflection seismic exploration, *Geophys.*, 40, 1, 158-159.
- Douze, E.J., 1967, Short-period seismic noise, *Bull. Seism. Soc. Am.*, 57(1), pp.55-81
- Draganov, D, K. Wapenaar, W. Mulder, J. Singer and A. Verdel, 2006, Seismic interferometry applied to seismic background-noise field data, *Proceedings of the 8th SEGJ International Symposium on Imaging Technology*, dd050924.
- Draganov, D, K. Wapenaar, W. Mulder, J. Singer and A. Verdel, 2007, Retrieval of reflections from seismic background-noise measurements, *Geophys. Res. Lett.*, 34, L04305, doi:10.1029/2006GL028735.
- Draganov, D., X. Campman, J. Thorbecke, A. Verdel and K. Wapenaar, 2009a, Subsurface structure from ambient seismic noise, *Proc. of the 71st EAGE Conf. And Exh.*, Z038.
- Draganov, D., X. Campman, J. Thorbecke, A. Verdel and K. Wapenaar, 2009b, Reflection images from ambient seismic noise, *Geophys.*, in press.
- Gupta, I. N., 1965, Standing-wave phenomena in short-period seismic noise, *Geophys.* 30(6), pp1179--1186.
- Paul, A., M. Campillo, L. Margerin, E. Larose and A. Derode, 2005, Empirical synthesis of time-assymetrical Green functions drom the correlation of coda waves, *J. Geophys. Res.*, 110, B08302, doi: 10.1029/2004JB003521.
- Ruigrok, E., X. Campman and K. Wapenaar, 2009, Lithospheric-scale seismic interferometry: a comparison of approaches to deal with an irregular source distribution and source-side reverberations, *This workshop*.
- Seriff, A.J., C.J. Velzeboer and R. J. Haase, 1965, Possible P-wave observations in short-period seismic noise, *Geophys.* 30(6), pp1187--1190.
- Suleiman, A. S. and D.I. Doser, 1995, The seismicity, seismotectonics and earthquake hazards of Libya, with a detailed analysis of the 1935 April 19, M=7.1 earthquake sequence, *Geophys. J. Int.*, v. 120, pp. 312-332.
- Toksöz, M. N. and R. T. Lacoss, 1968, Microseism: mode-structure and sources, *Science*, 159, pp. 872—873.
- Wapenaar, K., 2004, Retrieving the elastodynamic Green's function of an arbitrary inhomogeneous medium by cross correlation, *PRL*, 93, 254301-1-254301-4.
- Wapenaar, K. and J.T. Fokkema, 2006, Green's function representations for seismic interferometry, *Geophys.*, 71, SI33—SI46.
- Yao, H. J., X. Campman, M. V. De Hoop and R. D. van der Hilst, 2009, Estimation of surface-wave Green's functions from direct waves, coda waves and ambient noise in SE Tibet, *Phys. Earth Planet. Inter.*, under revision.
- Yang, Y. and M.H. Ritzwoller, 2008, Characteristics of ambient seismic noise as a source for surface wave tomography, *Geochem. Geophys. Geosyst.*, 9, doi10.1029/2007GC00181.

Lithospheric-scale seismic interferometry: a comparison of approaches to deal with an irregular source distribution and source-side reverberations

Elmer Ruigrok¹, Xander Campman² and Kees Wapenaar¹

¹ Delft University of Technology, Department of Geotechnology

² Shell International Exploration & Production B.V.

I. INTRODUCTION

A variety of seismic methods has been developed to image the lithosphere using the responses from distant earthquakes. On the one hand, there are the tomographic methods, that use either surface waves or body waves to obtain a low-resolution velocity-variation distributions. On the other hand, there are methods that use body waves to obtain a reflectivity image. In the later class, especially Receiver Function (RF) methods (Wilson & Aster, 2005), which image converted waves, are popular. RF are successful in obtaining an estimate of the large impedance contrasts, though the resolution is limited due to a few practical limitations.

An attractive alternative for RF would be to apply seismic interferometry (SI). Green's function retrieval or SI refers to the principle of generating new seismic responses by crosscorrelating seismic observations at different receiver locations. This technique is frequently used for the retrieval of surface waves between seismic stations since pioneering work by Campillo & Paul (2003), but can in principle be used to retrieve a complete Green's function (Wapenaar, 2004), dependent on the distribution of actual sources. When a collection of reflection responses is obtained using SI, one for a virtual source at each station position, a high-resolution reflectivity image can be obtained by using standard exploration-scale processing (Yilmaz *et al.*, 2000) as is shown by Draganov *et al.* (2009) for an exploration-scale passive dataset. A similar processing sequence could be used for lithospheric imaging. The advantages with respect to RF imaging would be 1) that SI can be applied on the Z-component only (decomposition can be left out), 2) the source-time-function deconvolution may be omitted, 3) free-surface-reflected phases are automatically used, without any model information required and 4) multiple information is suppressed in the stacking process.

It was previously realized by a number of researchers (Abe *et al.*, 2007; Fan *et al.*, 2006; Kumar & Bostock, 2006; Schuster *et al.*, 2004) that SI may well be applied to transmission responses from distant earthquakes, detected by broadband seismic stations. Two relevant issues were previously unaddressed, 1) irregular source distribution and 2) source-side reverberations.

In this study, we test which SI approach can be used best to deal with an irregular illumination and -at the same time- adequately suppresses artifacts caused by source-side reverberations. For these tests we generate

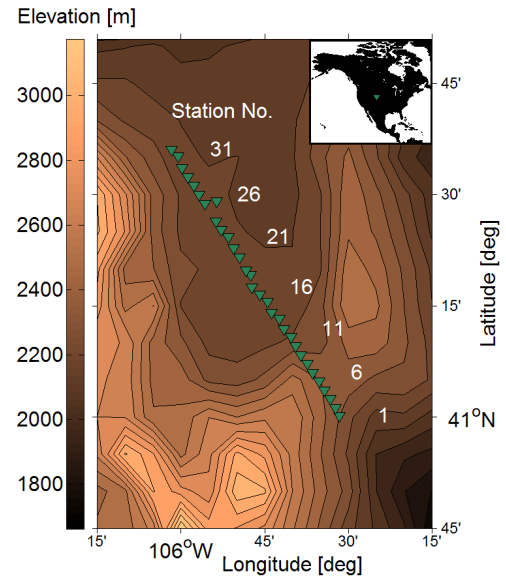


FIG. 1 The Laramie array of broadband stations (green triangles) and the local topology (colormap). The inset in the upper right-hand corner depicts North America and the array location.

synthetic data with similar source-side reverberation, and illumination, characteristics as an actual dataset from the Laramie broadband array (2000-2001).

II. MODELING

Fig. 1 shows the layout of the Laramie array. Only P-wave data is forward modeled. Thus, the assumption is made, that the actual data would be decomposed, or that the Z-component would be a good estimate of the P-wave component. For the modeling, the stations sampling is regularized. On Fig. 2, a simplified crustal model for the subsurface under this array, is depicted. The mean feature is a Moho at 40 km depth. This model is used for forward modeling transmission responses in a frequency band of 0.5-1.5 Hz.

In Wapenaar & Fokkema (2006) a SI relation is derived for a configuration with illumination from below and receivers on a free surface. This SI relation consists of a surface integration of correlations over source positions. For a regional array of receivers, an incoming wave caused by a distant earthquake is by approximation a plane wave.

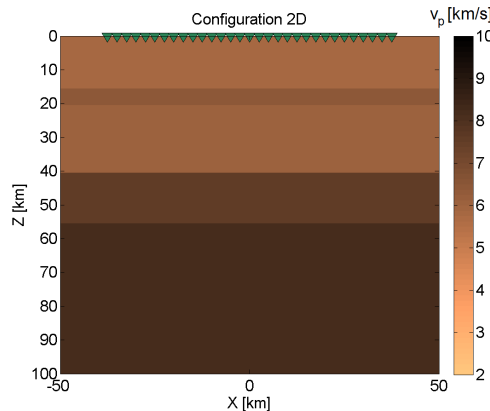


FIG. 2 A simplified horizontally layered velocity model for the crust and upper mantle below the Eastern Rocky Mountains. The model was derived from a refraction survey (Chulick & Mooney, 2002)

Consequently, each global phase, e.g., P, PP, Pcp and PKP, may be treated as a separate effective plane-wave source, characterized by a single rayparameter p . For earthquakes that are more or less inline with a receiver array, different phases may be characterized with a single horizontal rayparameter p . Thus, we rewrite the relation from Wapenaar & Fokkema (2006) to an integration over p :

$$\int_{\partial S_1} G(\mathbf{x}_A, p, -t) * G(\mathbf{x}_B, p, t) dp \approx G(\mathbf{x}_A, \mathbf{x}_B, -t) + G(\mathbf{x}_A, \mathbf{x}_B, t), \quad (1)$$

where $G(\mathbf{x}_A, p, t)$ denotes the Green's function observed at \mathbf{x}_A (one of the stations) due to a plane wave source with rayparameter p . S is a vertical section through the receivers and the medium of interest and ∂S_1 is the lower part of the enclosing line in the lower half space, see Fig. 3(a). The retrieved response $G(\mathbf{x}_A, \mathbf{x}_B, t)$, would be the Green's function between two receiver positions, \mathbf{x}_A and \mathbf{x}_B . To retrieve a response between one station \mathbf{x}_A and all the other stations, equation 1 would need to be repeated for varying \mathbf{x}_B (Fig. 3(b)). Effective sources on ∂S_1 correspond to small rayparameters. These rayparameters contribute to the retrieval of body waves at near and intermediate offsets.

With equation 1 both a causal and an anticausal response is retrieved. This is explained in Fig. 4. A reflection between \mathbf{x}_A and \mathbf{x}_B can be retrieved at positive times by contributions from sources with negative p . The same reflection can be retrieved at negative times by contributions from sources with positive p . The standard procedure would be to add the time-reversed anticausal result of equation 1 to the causal result, to increase the signal-to-noise ratio. Alternatively, the contributions from the positive rayparameters can be time-reversed prior to integration. Hence, only a response is retrieved at positive times, but the sampling of the integral is increased by a factor of 2. Thus, especially when the sampling of

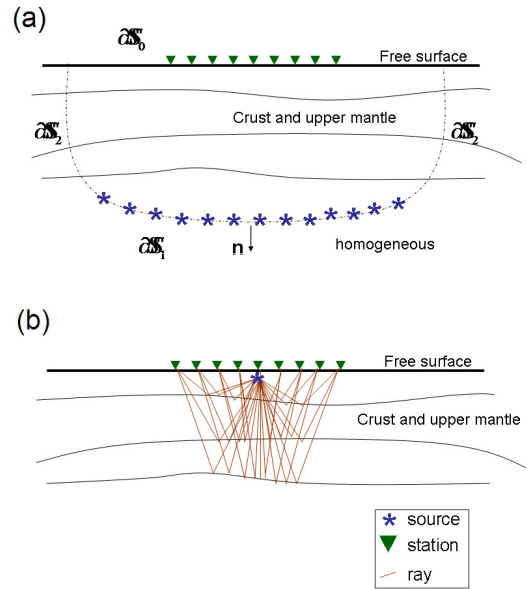


FIG. 3 (a) the configuration for regional-scale seismic interferometry, an approximately layered medium with illumination from below and a recording of responses on the free surface. (b) the retrieved response between the middle station and all the other stations. Note that only the retrieved primaries are depicted with rays, whereas in reality also free-surface and internal multiples would be retrieved.

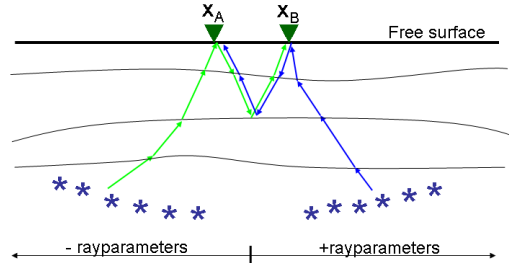


FIG. 4 The two specular rays for retrieving a reflection between a station at \mathbf{x}_A and at \mathbf{x}_B .

equation 1 is just insufficient, it is advantageous to apply time-reversal prior to integration. In the following we will call this the TRBI approach.

The moment tensor of an earthquake is of little relevance for this application of SI, since it may be assumed that the array lays within one focal plane. In this case, the observed response at \mathbf{x}_A may be written as a convolution of a source-time function (STF) with the Green's function $G(\mathbf{x}_A, p, t)$. By assigning a STF to the observed Green's functions in equation 1, the retrieved response will be a convolution of the Green's function between \mathbf{x}_A and \mathbf{x}_B with a stack of autocorrelations of all individual STF's. Through the autocorrelation, the STF's become all zero-phase, which facilitates a successful stacking (integration), even when earthquake responses have very

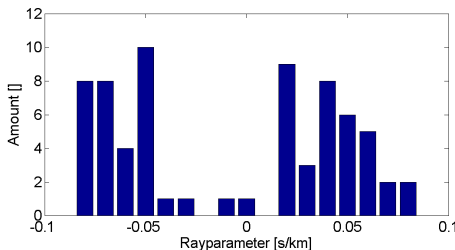


FIG. 5 A histogram distribution of the different phase-responses. Each phase response is represented by one ray-parameter. In total there are 69 phase responses. The binsize is 0.01 s/km.

different -and very complicated- STF's.

A. Irregular source distribution

During the array's deployment, which was about half a year, numerous high-quality earthquake responses were recorded. As a first selection criteria we take responses caused by earthquakes with a magnitude larger than 5. We further restrict the pool by taking only responses caused by earthquakes from within the 1st Fresnel zone for direct waves and with acceptable data quality. We end up with 39 earthquake responses, from which we can extract 69 separate phase responses. The p distribution of these effective sources is depicted in Fig. 5).

In Fig. 6 different approaches are tested to deal with an irregular source sampling. In (a) the reference response is shown. This is a synthesized response for a source at $x=40$ km (stations 16). A primary reflection from all 4 interfaces can be distinguished. In addition, a 1st order multiple from the upper three interfaces can be seen. (c)-(e) are retrieved responses with equation 1 after adding the time-reversed anticausal result to the causal part and muting early times.

Comparing the retrieved responses (b)-(f) with the reference response (a), it can be seen that the first two reflections are not retrieved correctly for any SI approach. Due to the limited illumination, reflections from the shallow interfaces are not retrieved correctly (that is, with a smaller slope than the actual reflections) at large offsets. For this reason, early times at larger offsets are normally muted. In (b), nothing is done to take the source irregularity into account. Large artifacts can be seen, both due to overillumination and underillumination. Overillumination leads here to artifacts at times before an actual reflection and with a slope opposite to the actual reflection. Underillumination leads here to the retrieval of the near-offset with smaller frequencies than the actual ones. If the irregular spacings are approximately known, the rayparameter domain can be divided into bins and the

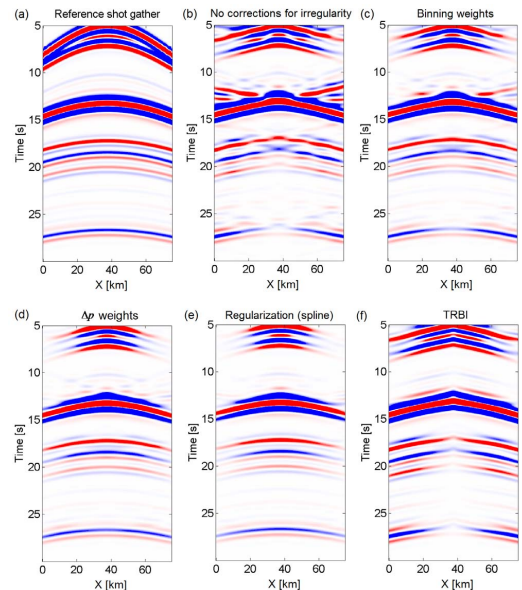


FIG. 6 Responses estimated with SI, with different adjustments for source irregularity, compared with the reference response (a). In (b) no adjustment is applied, in (c) binning weights are applied, in (d) Δp is taken as a weight, in (e) the integrand is regularized using spline interpolation and in (f) the TRBI approach is used.

traces can be weighted according to the amount of traces per bin (c). As a binsize 1 s/km is taken (see Fig. 5). If the source locations are well known, every trace can be weighted by the distance to the neighboring traces (Δp) (d). Alternatively, the integrand may be regularized to a source spacing satisfying the sampling criterion for SI (e). The last 3 approaches (c), (d) and (e), are successful in suppressing overillumination artifacts. The artifacts due to underillumination are limited. For this synthetic data with perfectly coherent events, the integrand regularization (e) gives the best results. When the TRBI approach is used (f) the irregularity artifacts, also the ones due to underillumination, are suppressed. A disadvantage of this approach is that the near offset is not reconstructed well, since the stationary-phase regions (Snieder, 2004) for events in the near offset are only partly sampled.

B. Source-side reverberations

As an input for SI, transmission responses caused by distant earthquakes are used. With SI we aim to use the receiver-side reverberations. Though, the transmission responses also contain source-side reverberations. The different source-side reverberations may be described as separate effective sources. E.g., a direct P-phase is followed for most earthquakes by a pP and sP phase. The time difference between P, pP and sP is often not enough to untangle the receiver-side reverberations of these different phases. Therefore, SI is to be applied on a blend of effective sources. Nevertheless, the application of SI

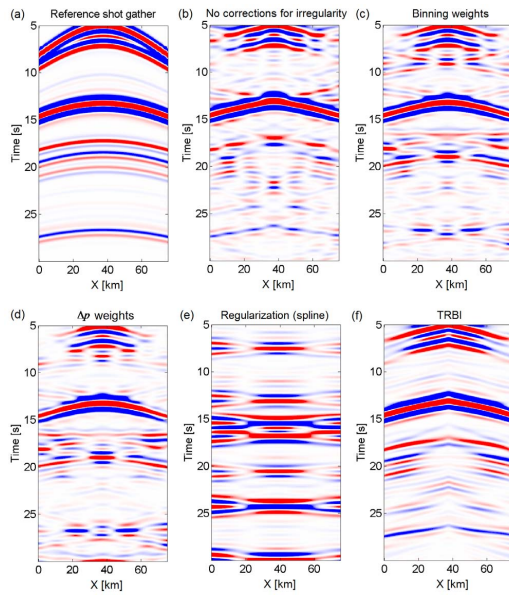


FIG. 7 Responses estimated with SI, with different adjustments for source irregularity, compared with the reference response (a). The used transmission responses contain 2 source-side reverberations. In (b) no adjustment is applied, in (c) binning weights are applied, in (d) Δp is taken as a weight, in (e) the integrand is regularized using spline interpolation and in (f) the TRBI approach is used.

needs to be such, that the spurious contributions caused by source-side reverberations are adequately suppressed.

A new synthetic dataset is created which does not only contain an irregular distribution of effective sources (Fig. 5), but which also contains source-side reverberations. In Fig. 7 again the same approaches are tested as in Fig. 6, but now the 'blended' transmission responses are used. For all approaches, a clear degradation of the quality of the retrieved responses can be noted, due to the additional crossterms. This degradation is worst for the regularization (e). The crossterms are different for each source, thus for each trace in a correlation panel (the integrand of equation 1). A straightforward spline interpolator cannot handle the large variations from trace to trace. This result might be significantly improved by a regularization algorithm with which random variation between traces are suppressed, see, e.g., Zwartjes & Sacchi (2007). The result of binning (c) and Δp (d) are quite bad, since different weights are given to the different cross terms in the correlation panel and therefore these crossterms stack out less successfully than when no weights are applied (b). The leftovers of the cross terms can be noted here as cross-shaped artifacts. The TRBI approach (f) gives the best results. Since no weights are applied, the cross terms stack out similarly as for (b), but additionally the source-sampling-irregularity artifacts are suppressed. Again the near offset is retrieved less successfully here, because of an amplitude reduction inherent to this SI strategy.

The blended transmission responses are used to re-

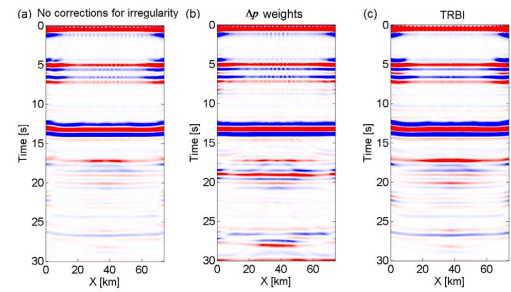


FIG. 8 Zero-offset stacks obtained from data retrieved with SI, using different adjustments for source irregularity. In (a) no adjustment is applied, in (b) Δp is taken as a weight, and for (c) contributions from sources with positive p are time-reversed prior to integration.

trieve 31 shotgathers, for a virtual source at each station position. Subsequently, the retrieved shot gathers are resorted to CMP (Common-Mid-Point) gathers. All CMP gathers are NMO (Normal Move-Out) corrected with the actual velocity model (Fig. 2 and stacked to obtain one zero-offset stack. This is the response as if there was a plane wave source at the free surface. The zero-offset stacks for the different methods are shown in Fig. 8. The resulting stacks for binning and regularization are left out.

Fig. 8(a) is a good estimate of the reflectivity of the subsurface. Only near zero time a spurious event can be seen, which is caused by using only a limited illumination range. The same spurious event can be noted in (b) and (c). The irregularity and source-blending artifacts, which were obvious on individual shotgathers (e.g., on Fig. 7(b)) have been suppressed. Contributions from multiples were partly suppressed in the stacking process. Fig. 8(b) shows the stack made with body-wave responses that were obtained with a Δp weighing SI approach. In this stack, artifacts caused by source-blending, remain. The stack that is made with body-wave responses from the TRBI approach (c) is similar to (a), though with a closer look it can be seen that the interfaces in (c) are more smooth than in (a).

Subsequently, the zero-offset stacks are migrated and converted from time do depth. The resulting images are depicted in Fig. 9. Since plane reflectors were imaged, the migration outcomes are similar to the zero-offset stacks.

III. CONCLUSIONS

We studied retrieving body-wave responses between a regional array of broadband stations using SI. SI consists of a surface integration of correlations over source positions. It is important to obtain enough effective sources from actual earthquakes to adequately sample this integral. We showed, with numerical data, that a few months of data suffices to select a good distribution of

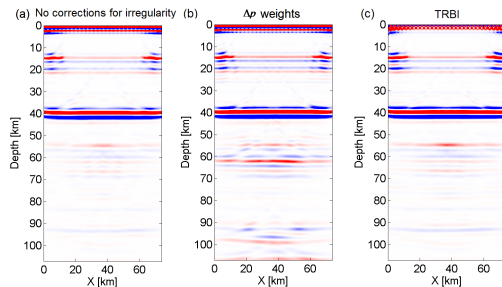


FIG. 9 Post-stack migrated and time-to-depth converted images, obtained from data retrieved with SI, using different adjustments for source irregularity. In (a) no adjustment is applied, in (b) Δp is taken as a weight, and for (c) contributions from sources with positive p are time-reversed prior to integration.

sources, at least, when the array is more or less inline with an earthquake belt. The irregularity of this distribution introduces over- and underillumination artifacts to the retrieved responses. These artifacts can be suppressed by weighing the contributions to the integrand with the distances between the effective sources, or by regularizing the integral. When, in addition, the influence of source-side reverberations is taken into account, a weighing strategy degrades the result. In this case, the best reflection response can be obtained when contributions from effective sources with positive rayparameters are time-reversed prior to integration (TRBI approach). We further processed the retrieved body-wave responses to reflectivity images. It turns out that, in this process, irregularity and source-blending artifacts are sufficiently suppressed. Only when a weighing strategy was used to obtain the body-wave reflections, source-blending artifacts remain. In conclusion, we can state that a straightforward implementation of SI suffices if the eventual goal is to obtain a reflectivity image. If also the retrieved body-wave responses are studied, it is better to use the TRBI approach.

Acknowledgments

This work is supported by The Netherlands Organization for Scientific Research (NWO).

References

- Abe, S., Kurashimo, E., Sato, H., Hirata, N., Iwasaki, T., & Kawanaka, T., 2007. Interferometric seismic imaging of crustal structure using scattered teleseismic waves, *Geophysical Research Letters*, **34**, L19305.
- Campillo, M. & Paul, A., 2003. Long-range correlations in the diffuse seismic coda, *Science*, **299**, 547–549.
- Chulick, G.S. & Mooney, W.D., 2002. Seismic structure of the crust and uppermost mantle of North America and adjacent oceanic basins: a synthesis, *Bulletin of the Seismological Society of America*, **92**, 2478–2492.
- Draganov, D., Campman, X., Thorbecke, J., Verdel, A., & Wapenaar, K., 2009. Reflection images from seismic noise, p. in press.
- Fan, C., Pavlis, G.L., Weglein, A.B., & Nita, B.G., 2006. Removing free-surface multiples from teleseismic transmission and constructed reflection responses using reciprocity and the inverse scattering series, *Geophysics*, **71**, SI71–SI78.
- Kumar, M.R. & Bostock, M.G., 2006. Transmission to reflection transformation of teleseismic wavefields, *Journal of Geophysical Research*, **111**, B08306.
- Schuster, G.T., Yu, J., Sheng, J., & Rickett, J., 2004. Interferometric/daylight seismic imaging, *Geophysical Journal International*, **157**, 838–852.
- Snieder, R., 2004. Extracting the Green's function from the correlation of coda waves: a derivation based on stationary phase, *Physical Review E*, **69**, 046610–1–046610–8.
- Wapenaar, K., 2004. Retrieving the electrodynamic green's function of an arbitrary inhomogeneous medium by cross-correlation, *Physical Review Letters*, **93**, 254301–1–254301–4.
- Wapenaar, K. & Fokkema, J.T., 2006. Green's functions representations for seismic interferometry, *Geophysics*, **71**, SI33–SI46.
- Wilson, D. & Aster, R., 2005. Seismic imaging of the crust and upper mantle using regularized joint receiver functions, frequency-wave number filtering, and multimode kirchhoff migration, *Journal of Geophysical Research*, **110**, B05305.
- Yilmaz, O., Doherty, S.M., & Yilmaz, O., 2000. *Seismic Data Analysis: Processing, Inversion and Interpretation of Seismic Data*, SEG.
- Zwartjes, P.M. & Sacchi, M.D., 2007. Fourier reconstruction of nonuniformly sampled, aliased seismic data, *Geophysics*, **72**, V21–V32.

Electromagnetic Interferometry by multi-dimensional deconvolution applied to diffusive controlled-source exploration

Jürg Hunziker¹, Evert Slob¹, Kees Wapenaar¹

¹Delft University of Technology, Delft, The Netherlands, E-Mail: j.w.hunziker@tudelft.nl

Introduction

Controlled Source Electromagnetics (CSEM) can be used to identify potential oil or gas reservoirs previously mapped with seismics. In the marine application of CSEM, a boat tows a source in the ocean over an array of receivers situated at the ocean bottom. The source emits an electromagnetic field in the low frequency range. In our synthetic example the frequency is 0.5 Hz. The receivers record horizontal components of the resulting diffusive electromagnetic (EM) field as a function of offset from the source position. A reservoir forms a high resistivity zone which leaves an imprint on the recorded response. Besides the measurements above an expected reservoir, a reference measurement is taken in a region where no reservoir is expected. A difference between the two measurements at intermediate offsets indicates the presence of a reservoir. Figure 1 shows synthetically modeled data of a typical CSEM measurement above a layered earth structure. This technique is often also referred to as Sea Bed Logging (SBL).

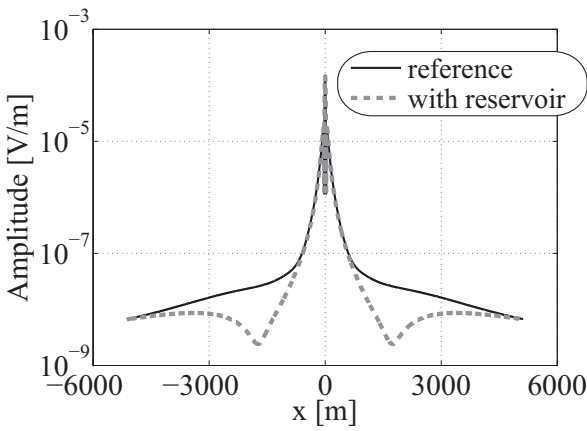


Figure 1: Synthetically modeled 2D electric field with a reservoir present in the subsurface (dashed grey line) and the reference response without a reservoir (solid black line).

The recorded EM fields are strongly affected by the water layer thickness and the position of the

source in the water as can be seen in Figure 2, where the EM fields are shown for a water layer thickness of 200 m (shallow sea) and 1000 m (deep sea). The source is in both cases 175 m below the water surface. This dependence of the water layer thickness makes a quantitative interpretation of the data with respect to subsurface structures difficult.

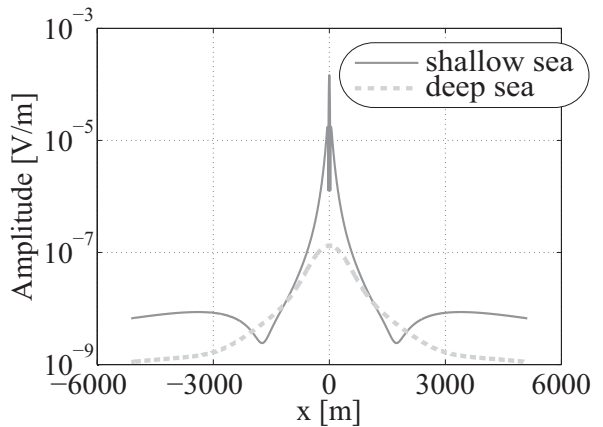


Figure 2: Synthetically modeled 2D electric field for a shallow sea situation (dark grey line) and a deep sea situation (dashed light grey line).

Interferometry by multidimensional deconvolution (MDD) can overcome this issue, because it allows to retrieve a reflection response which contains only information from the subsurface. By applying interferometry by MDD the structure above the receivers is replaced with a homogeneous halfspace consisting of the same material parameters as the first layer below the receivers. In other words, all reflections from above the receivers are eliminated. Furthermore the direct field is erased too and the sources are redatumed to the receiver positions.

Theory of Interferometry by MDD

Interferometry by MDD consists of two steps. First the recorded fields need to be decomposed in upwards and downwards decaying fields. This was first done by Amundsen *et al.* (2006)

in CSEM. Here an algorithm provided by Slob (2009) is used. This decomposition requires in 3D recordings of all four horizontal EM field components. The decomposed fields can be related to each other through a reflection response $\hat{\mathbf{R}}_0^+$:

$$\hat{\mathbf{P}}^- = \hat{\mathbf{R}}_0^+ \hat{\mathbf{P}}^+. \quad (1)$$

Equation 1 uses matrix notation introduced by Berkhouit (1982). Each column of the matrices $\hat{\mathbf{P}}^-$ and $\hat{\mathbf{P}}^+$, containing the upwards and downwards decaying fields, consists of various receiver positions but a fixed source position and vice versa for the rows. The circumflex denotes space-frequency domain and the superscripts $-$ and $+$ indicate upwards and downwards direction respectively. The subscript $_0$ stands for the absence of any reflections from above the receiver level in the reflection response.

In the second step, the reflection response $\hat{\mathbf{R}}_0^+$ is retrieved with a least-squares inversion of equation 1:

$$\hat{\mathbf{R}}_0^+ = \hat{\mathbf{P}}^- (\hat{\mathbf{P}}^+)^{\dagger} \left[\hat{\mathbf{P}}^+ (\hat{\mathbf{P}}^+)^{\dagger} + \varepsilon^2 \mathbf{I} \right]^{-1}. \quad (2)$$

The superscript \dagger denotes complex-conjugation and transposition and \mathbf{I} is the identity matrix. The stabilization parameter ε prevents the inversion from getting unstable. Compared to classical interferometry carried out by Cross-Correlation (CC), interferometry by MDD is not a trace to trace process, but requires an array of receivers. The advantages of MDD include elimination of the source signature, improved radiation characteristics of the retrieved source and relaxation of the assumption of a lossless medium. On the other hand, MDD is more expensive and the matrix inversion involved may be unstable. A general overview of interferometry by MDD can be found in Wapenaar *et al.* (2008).

Results and Conclusion

The retrieved reflection response for the shallow sea and the deep sea situation are plotted in Figure 3. Since the only difference between the two models is the thickness of the water layer, the two retrieved reflection responses have an identical shape. Consequently it can be said, that

interferometry by MDD successfully removed the effects of the water layer.

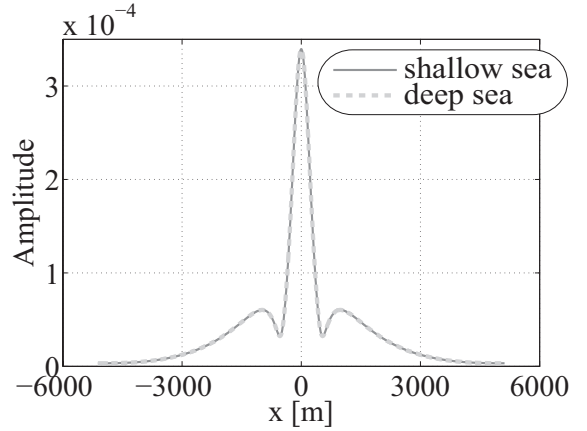


Figure 3: Retrieved reflection response for a shallow sea situation (dark grey line) and a deep sea situation (dashed light grey line).

Acknowledgments

This research is supported by the Dutch Technology Foundation STW, applied science division of NWO and the Technology Program of the Ministry of Economic Affairs (grant DCB.7913).

References

- Amundsen, L., Løseth, L., Mittet, R., Ellingsrud, S., & Ursin, B. 2006. Decomposition of electromagnetic fields into upgoing and downgoing components. *Geophysics*, **71**, G211–G223.
- Berkhouit, A. J. 1982. *Seismic Migration. Imaging of Acoustic Energy by Wave Field Extrapolation*. Elsevier.
- Slob, E. 2009. Interferometry by Deconvolution of Multicomponent Multioffset GPR Data. *IEEE Transactions on Geoscience and Remote Sensing*, **47**, 828–838.
- Wapenaar, K., Slob, E., & Snieder, R. 2008. Seismic and electromagnetic controlled-source interferometry in dissipative media. *Geophysical Prospecting*, **56**, 419–434.

We are hands-on with tomorrow's energy challenges

40 years of pioneering operations on the Norwegian continental shelf have made us world leaders in the field of maritime oil and gas activities. We apply our skills and experiences from these demanding conditions to the rest of the world. We consistently work to find sustainable solutions for the energy requirements of the future. Our pioneering projects for carbon capture and storage are vital in order to reduce the climate impact.

www.statoilhydro.com

StatoilHydro

